SILVER NANOCLUSTER SINGLE MOLECULE OPTOELECTRONICS AND ITS APPLICATIONS

A Thesis
Presented to
The Academic Faculty

by

Tae-Hee Lee

In Partial Fulfillment
of the Requirements for the Degree
Doctor of Philosophy in Chemistry

Georgia Institute of Technology
Jan 2004

SILVER NANOCLUSTER SINGLE MOLECULE OPTOELECTRONICS AND ITS APPLICATIONS

Approved:

Professor Robert M. Dickson, Chairman

Professor Mostafa A. El-Sayed

Professor Thomas Orlando

Professor C. David Sherrill

Professor Mohan Srinivasarao

Date Approved JAN 23 2004

ACKNOWLEDGMENTS

I would like to thank my advisor Dr. Robert Dickson for his support and enthusiasm about my research. I thank our group members, Yasuko Antoku, Jose Gonzalez, Lynn Peyser, Jie Zheng, and Chad Hladik for their help and friendship. I also thank my Committee and Dr. Mike Barnes for their support and help. Lastly, but most importantly, I would like to thank my family – my mother, my father, my sister, my brother, my brother-in-law and my fiancé Sunhee – for their endless support and love.

TABLE OF CONTENTS

LIST OF TABLES

LIST OF ILLUSTRATIONS

SUMMARY

Charge transport dynamics through single silver nanoclusters were investigated. Silver nanoclusters were *in-situ* formed within electromigration induced nanogap junctions efficiently forming semiconducting electrodes for molecular electronic devices. Formed silver nanoclusters within the junction show strong multicolored single molecule electroluminescence (EL) at room temperature under DC, AC, and customized pulse train excitation. EL mechanism of silver nanoclusters is field induced ionization of silver nanoclusters followed by field emitted electron reinjection into the excited states of silver nanoclusters. Complicated on-off behavior of the EL according to the applied electron reinjection energy yields electrically excited single molecule absorption spectra, and Ag_3, Ag_5, and Ag_6 were identified in the nanogap junctions. The reproducible complicated on-off behavior of these nanoclusters can be useful as extremely efficient computing elements. Two nanoclusters yielded a full adder, which would otherwise consume at least 25 conventional FETs. Another interesting aspect of the system was found in its electrical properties and heterojunction nature such as diode behavior and asymmetric photoconductivity. Prototype FETs based on this heterojunction nature of electromigration induced nanogap junctions were also tested. Optical illumination on the junction area is

found to change its electrical properties, which can be a useful property to visualize optical writing of electric circuits.

This scientifically and technologically rich system (electromigration induced silver oxide nanogap junctions filled with in-situ formed silver nanoclusters) has many interesting properties as investigated in this thesis research. Most importantly, this system yielded a non-controversial method of studying charge transport dynamics through single molecules in a molecular electronic device structure. Revealed through this research, tunneling current of field emitted electrons through molecular states may explain many negative differential resistance (NDR) phenomena in molecular electronic devices. From the perspective of engineering, many nanoscale photonics and optoelectronics applications based on this system are also viable.

CHAPTER I

INTRODUCTION

Long range charge transport based on electronic band theory has most often been employed to model charge transport dynamics through bulk solid state materials.[1] Although unable to accommodate the particle-like behavior of charges, this band theory based charge transport dynamics have successfully explained many physical phenomena within crystalline metals, semiconductors, and crystals even with defects where the charge transport takes place mainly through the collective motion of charges or wave-like propagation. While incapable of providing a precise picture of charge transport dynamics in nanoscale materials, the long range transport theory based research and outcomes thereof remain the basis of flexible electronics such as computers, which utilize electrostatic charge and electrochemical potential for processing information.[2]

As the size of functional elements in computers continues to shrink, the charge transport dynamics within nanoscale semiconducting elements no longer follow the band theory based charge conduction. This anomaly from the perspective of classical wave-like charge transport originates from the lack of translational symmetry and quantum confined transport media which are

sometimes even smaller than the wavelength of charges of reasonable energy and concentration, i.e., several nanometers. To avoid such obvious contradictions in explaining nanoscale charge transport, researchers started treating nanoscale materials as separate individual entities responsible for charge transport[3-10], such as a single molecule interacting with electromagnetic wave. Utilizing such constructs, researchers are trying to understand the anomalous charge transport dynamics through nanoscale materials (different than ohmic or exponential charge transport with respect to the applied field strength). Such unique transport leads to several interesting phenomena: Coulomb blockade effects for additional charges yielding regularly spaced conductance peaks[10-13], inelastic scattering and tunneling through the vibrational or electronic states of nanoscale materials, which, in many cases, yields conductivity peaks[14-16] or negative differential resistance (NDR)[17-20]. In many cases, these conductivity peaks or NDR reflect the coupled states of the nanoscale materials with charges.[17-20] Several theoretical and experimental results have been reported about this anomalous charge transport through nanoscale materials.[11-26] Despite the numerous discrepancies among them, all indicate that charge transport through nanoscale materials is distinctively different from that through bulk materials. Still an open problem,[27] understanding and controlling charge transport dynamics through nanoscale materials is a very critical problem both in fundamental science and in application engineering. Scientifically, as energy is transported through materials at fundamentally small scales, the charge transport within nanoscale materials will provide deeper

insight into how molecules respond and interact with their environment, thereby providing better understandings of nature. From the engineering perspective, charge transport within nanoscale materials will provide the basis of the ultimate small size functional elements useful for many applications such as thumbnail sized computers or encyclopedia.

This thesis is devoted to the measuring and understanding the charge transport dynamics through nanoscale junctions with single molecules. The electric current through a molecule within a broken junction was found to be a consequence of the same process as the tunneling of field emitted electrons through the molecule's electronic states. It will also contain some application ideas and implementations of the scientific studies.

1.1 Motivation of molecular electronics

Current computing technology is based on the binary logic operations performed by transistors as electronic switches. Transistors were first developed by combining two diode junctions to create bipolar transistors.[28-30] Diode junctions allow one direction of current flow and the current flow is an exponential function of the applied electric field across the junction. Diodes are normally composed of two different semiconductors doped with different materials to cause different electrochemical potentials of the charge carriers on each side of the junctions. The electrochemical potential difference of the charge carriers within each side of the junction causes the preferential charge flow direction. When the two differently doped semiconductors are put together, some charges

around the junction naturally flow across the junction to cancel the abrupt junction potential difference resulting from the different material work functions. This initial charge flow will stop after a charge depletion layer is formed at the junction setting up a potential energy barrier at the junction. Therefore, to enable charge flow, energy must be provided to the charge carriers so that they can overcome the junction potential barrier. According to the Maxwell approximation of the Fermi distribution (Maxwell-Boltzmann and Fermi-Dirac statistics agree with each other within 5% when the energy of the charge carrier is at least 3kT higher than that of the Fermi level[3]), the concentration of charge carriers with high enough energy to overcome the junction potential barrier is an exponential function of their energy. Thus, by combining two differently doped semiconductors, the current flow is restricted to one direction showing exponential increase with the charge carrier energy increase by applying an external electric field. This exponential current flow is the basis of charge switching within an electronic circuit. In a bipolar transistor, the electrochemical potential of charges in the base region is controlled so that the electric current between emitter and collector can be turned on. After several years of bipolar transistor development, field effect transistors were also introduced. A field effect transistor (FET) has a similar structure to the bipolar transistor(figure 1-1-1) . Instead of controlling the electrochemical potential of the charges in mid section of the two junctions by applying current, FETs control the electrochemical potential of the charges in the mid section by applying an electric field to the gate electrode that does not cause direct charge flow.

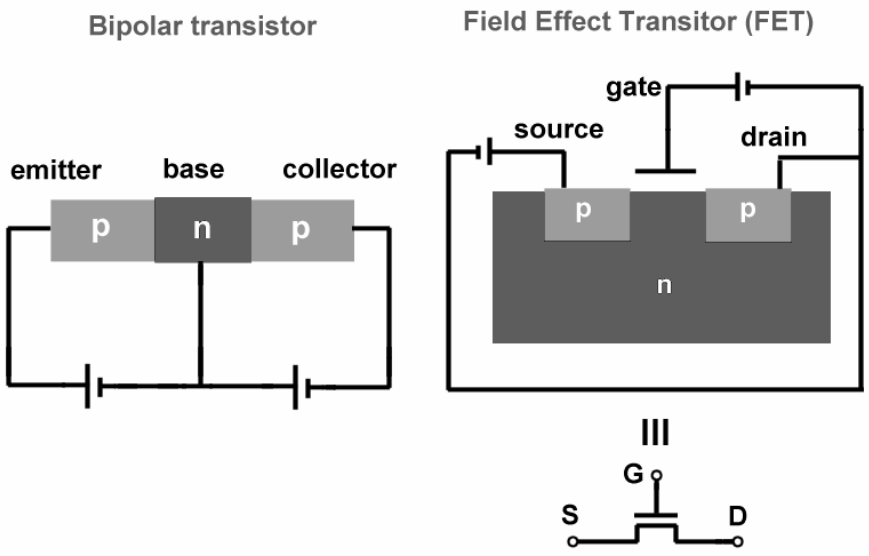

Figure 1-1-1. Typical transistors structure (left - bipolar transistor, right – field effect transistor). “n” and “p” mean semiconducting materials doped with n type and p type dopants, respectively. For example, Si doped with boron can be used as “p” type semiconductors. Si doped with nitrogen or phosphorus can be used as “n” type semiconductors. By controlling the electrochemical potential of charges in the bipolar transistors base region, one can control the passage of current between emitter and collector. In the case of field effect transistors, electric field is applied to the insulated gate electrode to control the electrochemical potential of the charges between source and drain, thereby, controlling the current between source and drain. This three electrode based charge switching is the basis of current computing technology.

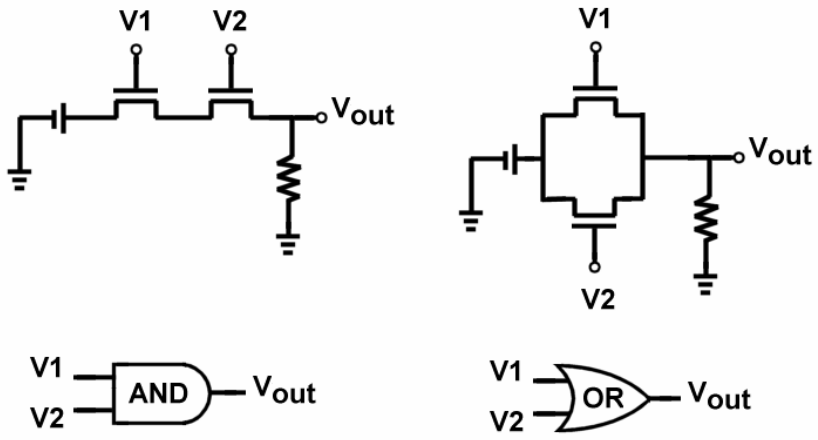

Figure 1-1-2. Examples of logic gates implemented with FETs. For the “AND” gate, only when both FETs are “on”, does a significant amount of current flow through the circuit. Then, the output voltage registers a potential difference according to the ohm’s law, V=IR. In the case of an “OR” gate, when either one of the two FETs is “on”, significant current will flow through the circuit. As a result, one observe a potential difference V across an output load given by V=IR. To turn on the FETs, two inputs to the gate electrodes of the FETs are used. The output load shown in the logic gates can be any given set of logic gates, thus, highly complicated logic operations can also be accomplished. For example, the output load can be another FET’s gate input to deliver the logic operation output to the next gates as their inputs. This consecutive connection of the logic circuits enables highly complicated operations with sometimes tens of gates connected to give one output.

Gate electrode is normally insulated from the circuit usually with a thin layer of oxide. By applying an electric field to the gate electrode, one can concentrate the charge carriers around the two junctions and can turn on the current flow between the source and drain electrodes. (figure 1-1-1) This gated current enabled contemporary computing technology electrically performing the binary logic operations. For example, by using two FETs, one can build an AND or OR logic gate as illustrated in figure 1-1-2.

Faced with one major challenge – the size of FET and therefore the rate of information flow, current computing technology actively seeks a way of downsizing the computing elements.[31] Individual molecules offer chemically tunable materials of ultimate small size that can be designed to carry specific function and stability under ambient conditions. Using single molecules as the switches for electrostatic charges may provide the answer for this challenge. Since charge transport through single molecules is governed by quantum mechanics, there are several major differences associated with charge transport through single molecules compared to that through bulk semiconducting materials.

1.2 Charge transport through single molecules/nanoscale materials

Charge transport through crystalline bulk semiconducting solid materials has been studied mainly with electronic band structure theory.[1,30] Electronic band structure theory treats charge transport as directed collective motion of charges over long distances which far exceed that of wavelength of charges. This

treatment ignores local variations within materials and in many cases it is not even necessary to consider such variations due to the dominating long range transport in the overall charge transport process. By combining the band structure with molecular orbital theory, some local defects and variations in bulk materials can be accounted for in the charge transport to certain degree.[1,32] For example, localized defect states in doped semiconductors and localized polaronic and solitonic states within bulk conductive polymeric materials can be taken into account in an approximate manner to better describe charge transport within those materials.[33-36] Despite these complicated modifications, the charge transport or electrical conduction through these bulk materials gives only simple on/off behavior according to the field strength with very few exceptions.[37] In effect, this simple on/off behavior of charge transport is the basis of modern computing technology which utilizes the amount of electrostatic charge as information.

When charge transport is restricted to nanoscale materials with sizes smaller than even that of the quantum wavelength of the lowest electronic states, charge transport dynamics get so complicated that theoretical considerations even for specific systems can be very challenging.[1,7,9,10] General theoretical methods and understandings remain particularly elusive. In contrast to the ohmic or exponential charge transport in bulk materials, the most dominating charge transport mechanisms through nanoscale materials are quantized charging and discrete energy level tunneling(figure 1-2-1).[5,10-26] Quantized charging can be well explained by the Coulomb blockade effect - an intermediate case of nanoscale electronics. The discrete stepwise current increase with CdSe

nanocrystals within nanoscale break junctions induced by an electromigration process is a typical example.[22,24] One has to pay extra energy to charge something with an additional charge especially when the charged particle is of significantly smaller scale than the charge wavelength. The integer multiples of the extra energy (=e^2/C from eV=eQ/C where Q=single electron charge in this case) should be paid whenever the upper level of quantized charged state is reached. Thus, stepwise increase in the current should be seen as the nanoscale transport media is charged with additional charges by applying higher voltages to induce higher current. This coulomb blockade effect with several nanometer size silver and gold particles has also been demonstrated.[12,13] The stepwise increase in the current in the report with the equal spacing of 27mV match well with the calculated value of e/C, 28mV. Unless extremely small particles are used, the coulombic charging energy is normally far below room temperature thermal energy, thereby requiring cryogenic temperature experiments to demonstrate such effect. Although researchers could see the coulomb blockade effect from several nanometer CdSe particles between gold electrodes[24], they could not explain why other complicated peaks appear in the dI/dV vs V characteristics that likely arises from other inelastic interactions between charges and the particle.

An application of such systems with designed organometallic molecules was demonstrated to show that an additional electrode insulated by a thin layer of oxide can alter the electrochemical potential of the molecular conduction bridge.[23,38-40] The resulting gated current through the molecule by applying different field strengths to the third electrode resembles the conventional field

effect transistors (FET). But one important problem with this application demonstration is that the researchers ignored the contribution to the current by field emitted electrons[41]. With two metallic electrodes separated by several nanometers, the most dominating current would be from field emitted charges. The field of 10^9V/m (or 1V/1nm) is more than sufficient to induce field emission out of any given metallic surface.[42] Therefore, the field emission through 50nm wide electrodes separated by only a few nanometers could well be dominating the total current especially compared to the current through <1nm wide region where the single molecule is located. The molecule, of course, can modify the electrochemical potential profile of the charges across the junction. However, having only one molecule within 50nm wide metallic break junction should not be sufficient to give the characteristic charge transport through the molecule as the total response of the system. The microampere level of reported current is also too high to safely flow through a molecule (in most cases of STM measurement, tunneling current through molecules does not exceed at most several nanoamperes[43,44]). Therefore, although the attempt to measure the electric current through single molecules was novel and inspired many research groups to study the science of charge transport through single molecules, the interpretation left much to further study by not considering the above facts – too high current and the dominating electric current due to the field emission. One other example to show such inspiring results is an organic molecule based molecular junction within mechanically broken nanoscale gap made of gold.[18,19,45,46] Researchers showed NDR type charge conduction through the

molecule demonstrating the possibility that the nitride group reduction/oxidation causes the sudden conductivity change of the molecule.[19] By the same reason described above, however, – not considering field emission and too high current level through a single molecule, and additionally, inelastic interactions of charges with the molecule, their interpretation left much to further develop and polish.

In many experimental reports, the charge transport thorough nanoscale materials also shows particular preferences toward certain field strengths suggesting discrete charge transport channels in the potential energy landscape.[4,5,9,20,47] As early as the 1960's, researchers attributed some of these discrete energy level charge transport to the inelastic interaction of charges with molecular vibrational modes(figure 1-2-1).[14,15,48,49] When charges inelastically interact with molecular vibrational modes, some portion of charge energy is consumed to excite the molecular states, thereby, adding additional conduction channels. In some cases, the energy loss due to the inelastic scattering process yields photons.[14,49,50] As a result of this inelastic scattering process between charges and molecular states, the charge conduction along the charge energy shows peaks sometimes with photons by enabling strong coupling between the charges and the molecular states at specific voltages. As explained in figure 1-2-1(C), a sandwiched Al_2O_3 layer (between aluminum and lead plates) doped with acetic acid or propionic acid yields vibrational spectra of these molecules in its d^2I/dV^2 vs. V characteristics. Electroluminescence has already been predicted based on this type of interaction between charges and molecular states in 1968.[49]

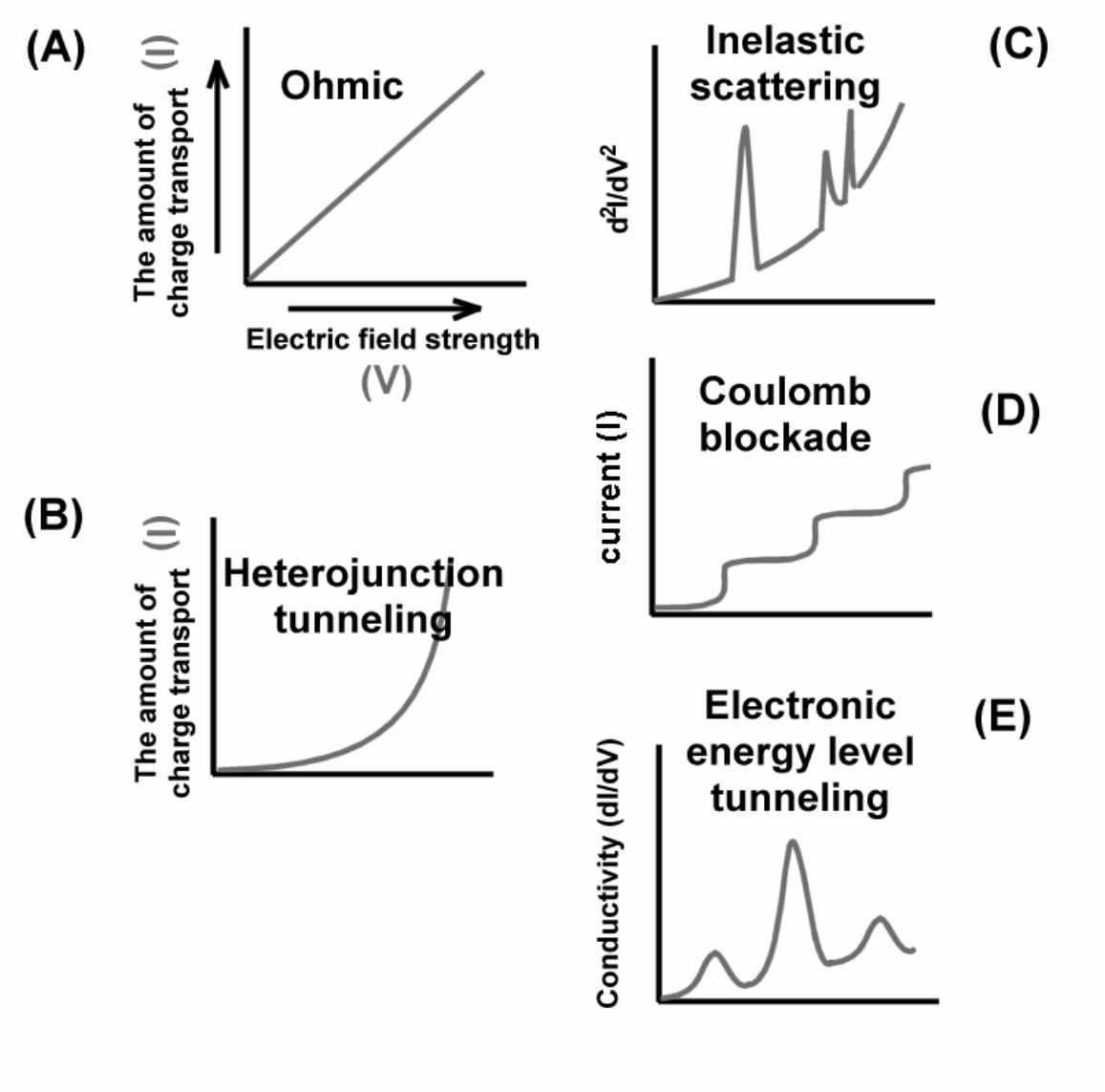

Figure 1-2-1. Examples of charge transport dynamics through solid state materials in bulk and on the nanoscale. (A) and (B) I-V characteristics of typical metals and heterojunctions. (A) Metallic conduction normally does not need higher energy than thermal energy to excite the charge carriers to enable current flow. As a result, a linear increase in the current is seen as field strength is increased. (B) Heterojunctions are usually made of two different semiconductors with different band energies and band gaps. With high enough forward bias,

charge carriers overcome the energy barrier to yield significant current. Below the threshold voltage of the exponential I-V curve, no significant conduction takes place. When high enough energy is provided to the carriers, charge flow through the semiconductor conduction bands takes place to yield an exponential increase in the current. Therefore, charges can be switched in a simple on/off manner in bulk semiconductor junctions. (C), (D), and (E) Schematics of several non-trivial charge conduction examples showing complicated charge switching. (C) Aluminum oxide is sandwiched between aluminum and lead. The oxide layer is exposed to a carboxylic acid (e.g. acetic acid or propionic acid).[49] Due to inelastic scattering of the electrons off of molecular vibrational modes, sudden charge consumption takes place at particular electron energies matching the vibrational energies of the molecules. The peaks all match those in the vibrational spectra of corresponding molecules. (D) A metallic or semiconductor nanoparticle is placed within a nanoscale break junction induced by an electromigration process.[24] At 4.4K, the junction shows discrete, approximately equally spaced charging energies characteristic of coulomb blockade behavior. (E) A mechanically broken nanogap junction holding a dithiol molecule. Even at room temperature, reproducible tunneling behavior can be observed. This particular system triggered much interest in the field of molecular electronics.[45]

Many of interesting charge conduction through molecular electronic devices is largely the scaling down of inelastic scattering process from 2-D monolayers to 0-D conduction channels. The fundamental processes remain the same, however. Unfortunately, the exact nature of the molecule-electrode junction becomes very complicated and difficult to understand as the interactions of electrons within structure of true nanoscale. One early example of these 0-D NDR structures was shown with C_{60} within a gold junction.[16] Although researchers did not describe the inelastic interaction between charges and the molecule, the coupling between the vibrational states of C_{60} and the charges flowing through the junction was clearly shown in the report.

Lately, discrete electronic energy level tunneling (figure 1-2-1) based negative differential resistance (NDR) was also reported from several experimental systems.[17-20] Those experimental systems have metallic electrodes surrounding nanometer scale materials or single molecules. Acting as charge tunneling bridges, those materials yield NDR behavior of charge conduction through the junctions. This type of NDR was first reported with benzene dithiol within mechanically broken junction made of metallic gold.[18,19] By coupling the transporting electrons with the molecular electronic states, the reported system demonstrated NDR type charge conduction due to specific preference of the electron energies enabling coherent electron tunneling through the molecules. Another report from the same research group reported the molecular states between neutral and anionic forms according to the electrochemical potential provided by the two electrodes surrounding the molecule. Although the

explanation given in the report is not very clear to accommodate any general NDR behavior of such junctions, the coupling between electrons and molecular electronic states have been evidenced by other experimental systems and theoretical considerations of such systems.[6,7,20,21] several other interesting reports utilized well defined chains of metal atoms such as gold and silver.[51,52] In these reports, a better controlled system was used to study the charge transport dynamics through such nanoscale materials systems. By utilizing a properly matched Ni-Al lattice, the authors positioned metal atoms one by one to form a chain of metal atoms on the surface and used an STM tip on the top of the chain to probe the charge tunneling properties of the chains. The current or conductivity of the chains according to the applied voltage could probe the electronic states of the chains when the charges are coupled to the electronic states of the chains. The charge coupling with the upper electronic states of the metal chain yields peaks in the dI/dV vs V characteristics when the coupling gets strong at certain charge energies. As in a 1-D particle-in-a-box model, the energy of the LUMO equivalent of such chains of metal atoms should decrease as the box size increases. Therefore, the energy of charge, or the voltage required to induce such coupling should decrease as the chain size decreases. Accordingly, the conductivity peak position in dI/dV vs V characteristics moves toward lower voltage as the chain length increases.

Since these experiments necessarily involve very low level of charge detection and sometimes single electron detection, it is very complicated to setup such experimental systems to study the charge transport dynamics through

molecular dimensions. Also, such systems generally involve state-of-the-art construction which makes the charge transport dynamics studies even more difficult. These junctions, however, can be of practical significance due to their fundamentally small size. NDR type junctions are especially of significant interest for a new efficient computing scheme since the complicated on/off of charge transport according to the field strength can significantly enhance the efficiency of switching or information processing.[26,31,53] Therefore, from the perspective of both scientific and engineering interests, easier experimental systems are very important problem to solve. In this thesis, simple fabrication methods of such nanoscale charge transport junctions, as well as easier control and easier feedback detection scheme will be addressed. Such challenges were accomplished through the electromigration process and tailored electric excitation as well as the molecule-specific light emission as the feedback from the junction molecules.

1.3 Theoretical consideration of electron tunneling through single molecules/nanoscale materials surrounded by metallic electrodes

Among numerous charge transport phenomena such as tunneling, inelastic scattering, and coulomb blockade charging through single molecules and other nanoscale materials, theoretical aspects of tunneling through electronic energy levels have been extensively studied due to the rich experimental reports based on the phenomena. Many of the theories treat the tunneling as an electronic transition between electrodes and the bridging molecule. The tunneling

channels, or the energy levels for electronic transitions are treated as conduction channels in Landauer formalism (equation 1-3-1).[54,55]

$$I(V) = \frac{2e^2}{h} \cdot \int \frac{df(E)}{dE} T(E) \cdot dE \cdot V \qquad (1\text{-}3\text{-}1)$$

I(V) in the equation is current as a function of voltage V applied to the system. df(E)/dE is the density of the states available in the bridge, or the junction with electron transmission probability T(E) at an energy level E. Equation 1-3-1 indicates that the total current with an applied voltage V is given by the summation of the current through all the available conduction channels over the entire available energy range. At certain energy level E, the conduction probability is given by the transmission probability T(E). The transmission probability can be calculated by many different approaches.[5,56-62] In many cases, the conduction probability at energy E (=$\frac{df(E)}{dE} \cdot T(E)$) is the electronic transition between the electrode and the transport media. When $\frac{df(E)}{dE} \cdot T(E)$ in the equation 1-3-1 is integrated, it becomes the total transmission current between the electrodes and the junction molecules connecting them. The transmission probability through the junction molecule must be calculated at each energy level E. The integration range can be restricted to consider the density of states

available in the metal electrodes. It can be approximated to be E_f-eV/2~E_f+eV/2 with applied voltage V by assuming a parallel metal plate capacitor model and thereby yielding the quasi Fermi level difference of the two electrodes caused by the applied voltage. If one plate is charged in a pair of parallel plates, the opposite plate also gets charged with the opposite charges to cancel the electric field setup by the charging. As a result, the two plate will have the same amount of the opposite charges to each other in equilibrium. Thus, by applying voltage V, the energy of charges at one plate would be half of the energy (=eV/2) applied and the other plate also get half (=-eV/2). While likely a poor model, in the simplest picture of the electrodes pair separated by a molecule, the $\frac{df(E)}{dE} \cdot T(E)$ in equation1-3-1, thus, is the density of states available in the molecule if the electron transition probability between the metal electrodes and molecule is assumed to be constant. Therefore, one may think of the discrete electronic states of the bridging molecule as the conductance channels in the Landauer formalism (equation 1-3-1). The transmission probabilities through each channel of the conduction at energy E can be thought to be the combination of the density of states of the tunneling molecule at energy E and the perturbation connecting the states in metal and the molecules. Therefore, the tunneling current at one applied electric field strength can be calculated as the transition between the electronic states of the electrodes and the bridging elements both of which are modified by the external field. However, in real experimental systems, the simple picture provided above is not so accurate due to the dynamic nature of the conduction process. As charges pass through the molecule, everything in the

transport path experiences the time dependent modification of the electrochemical potential. To accommodate such considerations, researchers started using Green's function formalisms to estimate the behaviors of these devices.[57,63] Currently, such calculations are available only in the DFT level although it is considered to be good enough for the Green's function approach. Such efforts could explain several experimental systems fairly accurately.[57,64] Additionally, with the complication of electrode structure attached to the bridging element, researchers have shown that it is almost impossible to predict the general results of such experimental systems.[7] Lately, if the bridging elements are directly attached to the metallic electrodes, it was suggested that the discrete energy level tunneling through bridging elements may not be as obvious as expected due to the energy level broadening by mixing the electronic states in the bridging elements and in the metal surface.[6,7] Thus, to get the pronounced tunneling current through discrete electronic energy levels of the bridging elements, the elements and electrodes should be separated by a tunneling barrier such as a semiconductor, an insulator, or at the very least a several carbon long aliphatic chains.

1.4 Field emission as a mechansim of charge transport through molecular devices and the energy distribution of field emitted electrons

When strong enough electric field is applied to the surface of materials, some electrons can escape the surface and be transmitted toward the collector, which holds a higher potential than does the surface. This field induced electron

emission is called field emission. Generally, metal surfaces require 10^8 V/m to show significant field emission current.[41,65,66] Field emission sources are currently utilized as illumination sources of the microscopy technique called field emission microscopy and as display beam sources.[42,65,67] There have been reported a few materials demonstrating very low field emission threshold voltages - a very important property for such applications.[68-70] For example, diamond with various structures such as thin films and nanodots can emit large numbers of electrons with very low voltages such as three orders of magnitude lower than that for normal metal films. The amount of the field emitted electrons follows the Fowler-Nordheim equation when these electrons can be assumed to pass through a material across which their potential varies only slowly and electrons can move freely(equation 1-4-1).[41,42,65,66] As indicated in the equation, the tunneling current density shows threshold behavior. After the threshold, the tunneling current density dramatically increases as applied electric field increases.

$$j \approx a \frac{E}{\phi^{3/2}} \exp(-b \frac{\phi^{3/2}}{E}) \qquad (1\text{-}4\text{-}1)$$

In this equation, j is current density of the field emission, φ is the work function of the surface, E is the applied electric field across the surface and vacuum or semiconductor, and a, b are the constants independent of field, work

function, and to each other. The field emitted electrons have a peak in their energy distribution. Within certain range of relatively low electric field strengths (~10^9V/m, or 1V/1nm), the total energy of field emitted electrons peaks around the Fermi energy of the surface – in many cases with FWHM <0.2eV.[42,65,66] These electrons within kT below the Fermi energy level is also considered to be the most mobile electrons because of their thermal energy. Even in the high current density cases with metals of high Fermi energies (4.5eV), the FWHM of the electron energy distribution does not exceed 1eV even at room temperature.[42] Still yielding a peak in the energy distribution of field emitted electrons, high electric field generally shows broadened and shifted peaks toward higher energies than in the lower field case.[42,66,71] This energy distribution peak originates from the evanescent nature of the electronic wave function along the distance from the metal surface. As a result, electron density at a given distance from the surface exponentially increases as the energy of the electrons increases.(equation 1-4-2)[42]

$$J(E) = aV \exp(\frac{-b}{V}) f(E) \exp(\frac{cE}{eV \cdot \sqrt{\phi}}) \qquad (1\text{-}4\text{-}2)$$

In this equation, f(E) is Fermi distribution of the metal surface, E is the energy of the field emitted electrons, V is the applied electric field, φ is the work function of the surface, and a,b, and c are constant independent of field strength

or energy. Since the energy of field emitted electron peaks around the quasi Fermi energy of the surface, an electric field of proper strength would show tunneling probability peaks at the discrete states or bands through a tunneling bridge close to the metal surface (closer than several nanometers). Tunneling bridges such as surface adsorbates or semiconducting layer on top of the metal surface experimentally proved this effect.[41,72-80] From these studies, it has been shown that one can probe the excited states of the surface adsorbates or conduction band of the semiconducting overlayers by measuring the energy distribution of the field emitted electrons out of a metal surface all through these overcoating materials. In some cases such as CO adsorbed Mo surface, inelastic interaction between field emitted electrons and adsorbates were also reported.[41,80]

Having fundamentally very similar process of charge transport to that in 2-D inelastic scattering structures and 0-D molecular/nanostructure bridges, these field emitted electron energy distribution affected by overlayer/adsorbate can provide an accurate insight into the charge transport process within such structures. The 2-D thin layers or 0-D bridges through which charges transport can be regarded as overcoating layer or surface adsorbates in surface modified field emission process.[41,72-80] In most cases of charge transport study through such devices, nanometer separated two metal electrodes are attached to these structures. Since these structures are made of significantly different materials from the electrodes, it would be hard to imagine there can be any coherent charge propagation channels across the two electrodes in such devices. From

the perspective of classical wave-like charge transport, thus, it is fairly reasonable to assume that the two electrodes in such devices are almost insulated from each other. By applying voltages to such structures, the field strength across them (1V/1nm=10^9V/m) would be high enough to induce field emission. Therefore, this field emission-like charge transport would be more dominating process than any other long range charge propagation such as coherent conduction through electronic states. Therefore, by applying voltages to such nano-devices, field emission out of the electrode would dominate the total current. Consequently, the inelastic scattering and tunneling process of those field emitted electrons through the nanostructure bridges will yield the unique charge transport behavior attributed to the bridge materials. The resulting charge transport behavior is fundamentally same as that of long-known field emission processes through overlayers or adsorbates. By combining the field emission with inelastic scattering/tunneling process[41,74,77,78,80], both of which are well known since early 1970's, one can provide more precise picture of charge transport through many molecular/nano devices. To summarize the significance of modified field emission processes to the molecular electronic devices, charge transport through nano structures is not a different problem from the field emitted electron energy distribution modification due to surface adsorbates or overcoating layers.

One difficulty with the field emission model to predict the charge transport through nanoscale devices is in the local variation of surface properties of the electrodes. Since the nanoscale devices have very complicated electrode

surface structure, which is far from being flat and clean, it is hard to quantify the energy levels (such as local work functions) associated with the electrodes around the nanostructures through which the charges pass through. Even from a different approach to quantify charge transport through molecular devices[6,7], it is well known that the interaction between the electrodes and molecules play a very important role. This complicated unpredictable interaction between the electrodes and molecules is mainly due to the complicated device atomic geometry around the molecule.

1.5 Electroluminescence mechanism in solid state devices

Electroluminescence from solid state materials (inorganic and organic) have long been known since the early 1900's.[81-83] Dominating mechanisms for these electrically induced emissions are band gap emission and exciton decay emission. Solid state semiconducting materials form valence and conduction bands separated by band gaps within which no electron can be excited. Sometimes, the bottom of upper energy state band (conduction band) and the top of lower energy state band (valence band) have very well matched symmetries enabling direct excitation and decay pathways between the two states. The electroluminescence based on band gap emission is common in many electrically driven semiconductor operations.[28-30] If charge carriers are injected into the upper and lower bands (electrons to the upper band and holes to the lower band) such as in the normal semiconductor operation, the charges can recombine anywhere in the materials with proper states to yield electrically driven

band-gap emission.[28,30] This kind of band gap emission is easily observed at normal heterojunctions where electrons and holes recombine and carry electricity. Since the states in bulk crystalline semiconductors are not localized in most cases, band gap emission is normally not localized, unless specifically engineered to occur in a narrow recombination zone.

The defects incorporated within semiconductors in many cases can yield discrete energy states within the band gap of the semiconductors. Sometimes, the additional states due to the defects are paired so that electronic transition between those states can take place. Since these states are introduced by incorporating defects, they form localized states in many cases. But the holes and electrons formed at such local sites can separately move around the materials although they are somewhat paired and often at least weakly bound to each other. This kind of paired electron and hole is called an exciton.[1,32] Depending on the materials in which the excitons are formed, excitons can be fairly mobile or immobile yielding free and bound exciton respectively. Excitons can decay through electron and hole pair recombination to yield either heat or photons. In case of electrical excitation, the exciton formation can be achieved either through the combination of two separate charges at one excitonic site as explained, or through the ion or charge bombardment on the excitonic site causing the charge separation or the excited state. After the excitons are formed at emissive sites, they can radiatively decay emitting electroluminescence. In chemistry friendly terms, charge injection means either positively or negatively ionizing the molecules, followed by charge compensation to result in

electronically excited states. This occurs only if the opposite charges with appropriate energy can be injected to the charged sites. These sites can be viewed as holding a pair of separate charges, and they eventually decay either radiatively or non-radiatively. This separate charge injection strategy generally yields higher efficiency of electroluminescence than does high energy charge collision induced excited state formation.[84-88] To further improve the efficiency of this type of electroluminescence, different strategies have been used to control the energy of injected holes and electrons as well as those of the transport media of these charges to facilitate exciton formation only at emissive sites.[89-91] For example, if the cathode Fermi level is too low compared to the LUMO or conduction band of the electron carrying layer, a semiconducting layer with intermediate energy level can be used so that only moderate energy is necessary to inject electrons into the electron carrying layer. The hole injection energy can also be adjusted with multiple layers with favorably matched energy levels. Another important factor for the efficiency of the LED junction is hole and electron mobility through the multiple layers of devices. To improve charge carrier mobility, many materials have been tested to identify good electron and hole transporting materials.[92-96]

To achieve a faster switching speed and elongate the device lifetime, many LEDs work under very fast AC or very short pulsed excitation. Therefore, the time response of an LED is an important property in terms of application. Researchers have used AC field and pulses to study the time response of the multilayered LED structure. Some interesting aspect of the LED structures

especially made of organic materials has been revealed. One of the most important aspects of the time response of these organic LEDs is that the light emission is lagged and the frequency of AC or the width of pulses is severely restricted due to the low dielectric constant of the most of the organic compounds.[97,98] To improve time response and efficiency of the organic LEDs, it is important to have materials with higher dielectric constant, or better charge transport property.

One particularly relevant light emission mechanism was reported as early as 1976[14,51] and predicted several years earlier.[48] In this report, inelastic electron tunneling to excite optically coupled surface plasmon modes yields electrically driven photons with broad range of energy covering the whole visible spectrum. Similar photon-yielding inelastic tunneling processes with electronic states of gold or silver have also been reported.[50] In addition to the exciton emission, band-gap emission and electron bombardment caused cathodoluminescence, the inelastic tunneling-induced light emission is another way to generate photons based on a solid state conductor-insulator-conductor structure. The inelastic tunneling-induced light emission is directly relevant to many of the studies of nanoscale charge transport and electroluminescence. Although distinctively different from the tunneling based electroluminescence, electric current induced – or hot electron induced - luminescence out of metal island films has also been reported.[99-102]

1.6 Electromigration process as a molecular junction formation method

under strong currents within thin metallic or well conducting films, atoms within the film become mobile as momentum from the electron “wind” is transferred to the heavier atoms.[103-107] As a result, voids form during the electron flow, eventually yielding a linear mechanical break that cease electron flow. This self-controlling mechanism to stop the movement of atoms is termed “electromigration” and is one main cause of electronic device failure through destruction of metallic electrodes.

Assuming voids formed in a polycrystalline thin film does not have electrostatic charge, the flux of voids is mainly determined by its concentration gradient and momentum transferred from the electron “wind”. The dependence of void flux both on its concentration gradient and electron flow is expected to be linear so that void flux divergence is zero, or no void build up is expected at the steady state.[103,105] However, the defects within the grains cause the local electron flow fluctuation yielding local heat fluctuation to force the void concentration gradient fluctuation out of equilibrium. Once triggered, the non-steady-state void concentration fluctuation causes and accelerates the void build-up at certain local points yielding macro scale voids. By the same self-accelerating fashion, the void grows until the cause of the instability, or electron wind, is ceased, which means that a gap in the materials along the electron path is formed to open the circuit. The size of these gaps ranges from several nanometers to several tens of nanometers.[22,103,108]

Resulting from momentum transfer, atoms also move toward the direction of electron wind. The two major components of the driving force of this

movement are electrochemical potential gradient and momentum transferred by the electron wind. To consider the movement of atoms, it is not necessary to consider the electrochemical potential gradient caused by the electric field since atoms can be fairly well assumed to be neutral. Thus, the consequence of the atomic movement would be the net movement of atoms and other electrically neutral materials toward the direction of electron wind flow.[103-106] During the linear failure formation caused by void migration, the electric field strength around the failure can be very high by dropping the most of the circuit potential difference right at the failure. Therefore, the electron momentum can very strongly blow off the materials around the failure to the direction of electron wind. As a result, the mobile atoms and neutral species will likely build up to the anode side of the gap. The anode is defined to be the electrode holding higher (more positive) potential during the electromigration process.

1.7 Electromigration-induced break junctions in molecular electronics

Recently, the electromigration process started being used to form electrodes separately by nanoscale gaps to study the charge transport dynamics through nanoscale materials.[16,22,24,108] Some methods provide a very narrow gap that is comparable to the dimensions of single molecules. This has triggered interest in the utilization of the electromigration induced nanoscale gap as the electrodes for single molecular junctions. This simple method can facilitate the charge transport study through single molecules and molecular electronics applications as well. Two examples are CdSe coulomb blockade junctions[23,24]

and organometallic molecule based FETs.[24,38] As mentioned earlier, the results out of these system were not clearly explained since they didn't incorporate field emission and inelastic scattering/tunneling which are probably dominating the charge transport process through the nanoscale break metallic junctions. Additionally, as FETs rely on spatial separation of gate and source-drain field, the direct scaling down of conventional FET does not apply to the molecular scale FETs. Despite these effects, the researchers showed that the nanocrystals and molecules can certainly modify the charge transport characteristics through these kinds of junctions.

1.8 Fluorescence of silver nanocluster and its applications to the molecular charge transport dynamics study

Molecular silver nanoclusters (Ag_2 to Ag_8) and their charged counterparts have been reported to strongly fluoresce in the visible spectrum within rare gas matrices, on silver oxide surface, as well as in aqueous solutions.[109-116] Their emission is much more stable and stronger compared to the fluorescent organic molecules due to the chemically inert properties of the metallic nanoclusters. Photoactivation of such small silver nanoclusters on silver oxide thin films opened a new interest to utilize those nanoclusters as an optical information storage media.[109] These small silver nanoclusters show molecule like behavior with well defined electronic structure identified by both experiments and calculations.[110,111,113-115,117-121] Lately, dendrimer encapsulated such molecular silver nanoclusters were synthesized in solution.[116] In the report, Ag_1~Ag_4 silver

nanoclusters show strong and stable fluorescence spanning whole visible spectral range. Lifetimes of these dendrimer encapsulated silver nanoclusters are also measured to show the similarity between electroluminescent species and the fluorescent ones, of which mass can be precisely determined.

The robust small silver nanoclusters can have several benefits over the organic molecules in molecular electronics. First of all, the chemically inert nanoclusters enable more reproducible and stable charge transport. Secondly, it is easier to fabricate molecular electronics device based on the metallic nanoclusters due to their robustness. Lastly, the strong emission out of the silver nanoclusters opens a great opportunity of electrically driven molecular light emitting devices.

Recently, STM-induced light emission from several silver atom chains of different lengths (Ag_2~Ag_5) were reported.[51] The emission resulted from charge recombination after charge tunneling through the excited states of these silver chains. The conductivity and emission intensity peaks are well aligned to overlap each other. The conductivity and emission intensity peak positions indicates that the excited state energies of the silver chains of different lengths scales as those in 1D particle in a box model. As mentioned above, the reproducible molecular scale junction current and emission is promising with these robust metallic nanoclusters as also shown with gold chains.[122]

1.9 Antibunching of photon streams out of single quantum sources and single photon sources

While still in the very beginning stage of development, there are other interesting computing scheme using different forms of information such as electron spins, photons and the polarization states of photons.[31] When a new computing scheme includes photons as its information or information media, several benefits could be realized. By using photons instead of electrons, communication and computational speeds can reach the vacuum speed of light without capacitance problems that plague high speed electronics. Additionally, controlled photon polarization states provide the highest communication security by quantum mechanically precluding undetected eavesdropping.[123,124] To realize these benefits of photons, convenient single photon sources, that ideally can also perform computational tasks, are needed.

While highly attenuated classical light sources may offer useful approximations of a single-photon source, only a single quantum system (atom, molecule, quantum dot, etc.) can provide a true nonclassical single-photon output.[124] First observed in dilute atomic beams, and later for single molecules in cryogenic molecular crystals, nonclassical (single-photon) emission is manifested experimentally in the measurement of the 2^{nd}-order fluorescence correlation function as *photon antibunching*.[125] The correlation function is measured by dividing the luminescence into two parts seen equally by photon-counting detectors D_1 and D_2 and measuring the distribution of time intervals, t, between detection events at D_1 and D_2. For a single-photon source, fluorescence antibunching is manifested a characteristic minimum for t near zero.(figure 1-9-1)

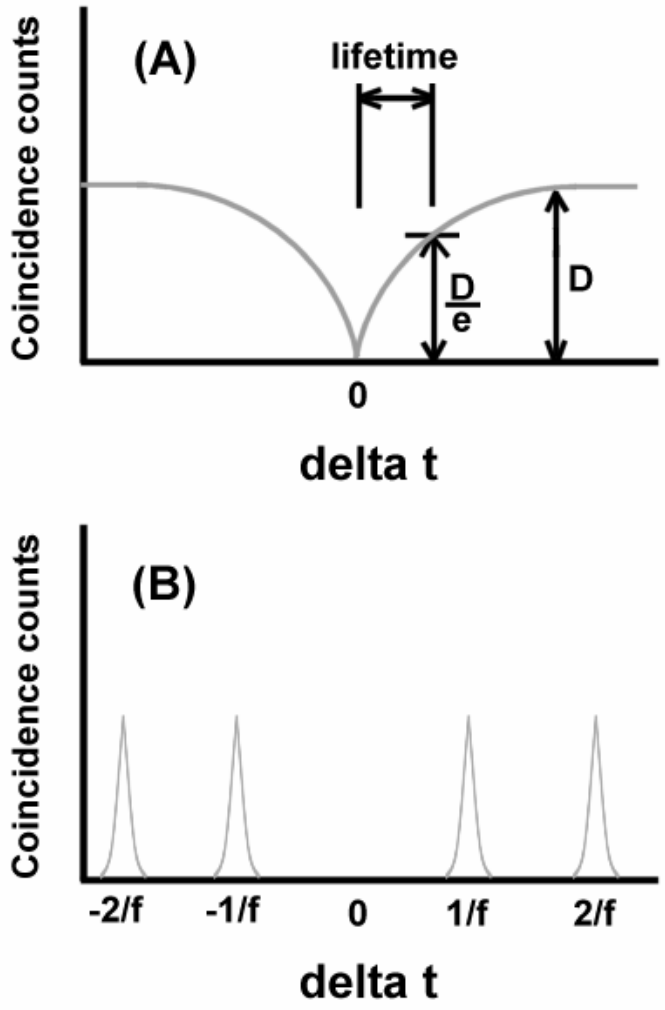

Figure 1-9-1. Ideal antibunching signatures of quantum emitters in a Hanbury Brown-Twiss configuration. The emission is divided into two (50/50), each of which is detected by a single photon detector. All starts/stop pairs of photon arrival times registered by the two detectors is measured and displayed as a histogram along the time difference of the two photon detection events. The probability of detecting two photons at time delay zero should approach zero as schematicized in the figure (A) under CW excitation and (B) under pulsed

excitation (see equation 1-9-1 and equation 1-9-2, respectively for CW and pulsed excitation). In case of CW excitation, the dip shape follows the inverse of exponential decay, and can thereby be utilized to deduce the excited state lifetime of the quantum emitters as indicated. In the case of pulsed excitation, a single quantum system can only emit a single photon at a time, therby preventing observation of a peak at zero delay if a sufficiently short pulse is used. The other peaks should be spaced as 1/f, or the inverse of excitation pulse repetition rate.

This feature has a simple physical interpretation: For a single-quantum system, the probability of two photons being emitted simultaneously is zero. By measuring the second-order fluorescence correlation function, $g^2(\tau) = <I(t)I(t+\tau)>/<I(t)>^2$ from individual quantum emitters using a Hanbury Brown-Twiss configuration, antibunching can be manifested by $g^2(\tau) \approx 0$. This experiment measures the distribution of arrival time differences, τ, between photon detection events at two separate detectors viewing the emission from a single source through a beamsplitter. For a single-quantum emitter, this distribution shows characteristic photon antibunching manifested as zero joint probability of detecting two photons simultaneously. As shown in figure 1-9-1, in case of CW excitation, $g^2(\tau)$ can be approximated as below equation provided that electronic polarization phase coherence is damped on a time-scale significantly faster than the fluorescence lifetime.

$$g^2(\tau) = 1 - \frac{1}{N}\exp(-\left|W_p + \Gamma\right|\tau) \qquad (1\text{-}9\text{-}1)$$

In the eqation, N is the number of emissive sites or chromophores, W_p is the pumping rate and τ is the radiative decay rate. In the case of pulsed excitation as shown in figure 1-9-1, when the pulse duration is significantly shorter than the fluorescence lifetime, $g^2(\tau)$ can be expressed as in equation 1-9-

2. In the equation, N is the number of emissive sites or chromophores, ω_{ml} is the pulse frequency, and Γ_f is the fluorescence decay rate.

$$g^2(\tau) = \sum_{i=1}^{N} \exp(-\left|\tau \pm \frac{i}{\omega_{ml}}\right|\Gamma_f) \qquad (1\text{-}9\text{-}2)$$

Despite the extensive literature on single-molecule/quantum dot luminescence in condensed phase, there have been very few reports of quantum optical measurements on these systems.[126-130] For most organic systems, the relatively poor photostability significantly limits the number of fluorescence photons that can be detected from a single molecule. Because the measurement of interest depends on coincidences between detected pairs of photons, the limited photochemical lifetime (usually on the order of several seconds at saturation intensities) practically precludes observation of antibunching from a *single* source molecule. Experiments by Ambrose, et al. and recently by Huser and co-workers on conjugated polymers in thin-films, circumvent this problem by generating a composite histogram of coincidences from hundreds or thousands of separate single-molecule measurements. In the case of conjugated polymers, this observation is particularly interesting since the optical output depends sensitively on the configuration of the polymer chain in the film. However fluorescence instabilities (such as blinking) and generation of highly reactive (dark) polaronic pairs at even modest excitation intensities has significantly limited applications of these materials in a photonics context.

Inorganic materials such as quantum dots or nitrogen vacancy (N-V) color center defects in diamond have attracted a great deal of interest in the context of quantum information processing primarily because of the high photostability associated with these species.[123,130] However, synthesizing such systems is especially challenging which severely limit the accessibility. Fluorescent organic materials, on the other hand, offer a convenience in processing and accessibility, however the relatively poor photostability (typically yielding around 10^4 detected photons) is a serious limitation in practicability. Several proof-of-principle experiments using photonic qubits have been achieved at distances up to tens of kilometers, although weak classical light pulses were used instead of true single-photon states. The important difference is that ultrasecure communication can only be guaranteed for *single-photon basis states* as a result of the 'no-cloning' theorem in quantum mechanics. In this thesis, I will describe antibunching of photon stream out of silver nanoclusters that can be used as robust single-photon resources in quantum information processing applications. These species are very stable and strong emitters showing photochemical stability several orders of magnitude higher than any other organic or inorganic species under ambient room temperature conditions.

Recently, an electrically driven single photon source was demonstrated based on cryogenic InAs semiconductor quantum dots.[126] By using electrical pulses to form excitons within the nanodot at cryogenic temperature, researchers proved that the radiative exciton decay within the quantum dot yields non-classical photon statistics – antibunching. Despite the significance of practical

application of such electrically driven single photon sources, no systems has been reported to promise the room temperature electrically driven single photon sources yet. Another novelty of single molecular electroluminescence can, thus, be found in the context of such applications - room temperature electrically driven single photon sources.

CHAPTER II

EXPERIMENTAL

2.1 Overall experimental scheme (figure 2-1-1)

Nanometer scale junctions were fabricated through a simple, one-step electromigration process. Junctions are formed on silver or silver oxide thin films by applying DC current. While the silver oxide nanoscale break junctions are formed by one-step electromigration process, silver nanoclusters are also *in-situ* formed within the junctions. All experiments focus on the charge transport behavior of the junction mediated by the silver nanoclusters within the junction. DC, AC and customized pulse trains were used to excite the junction nanoclusters and the optical response of the nanoclusters to such stimuli was investigated to study the charge transport dynamics through the single molecular nanoclusters. Some application ideas were experimentally tested utilizing the charge transport dynamics through the single molecular junction. On the other hand, the optical and electrical properties of silver oxide thin films and their nanoscale break junctions were also characterized from a materials point of view. Some application ideas of the break junctions as electronic components were also tested.

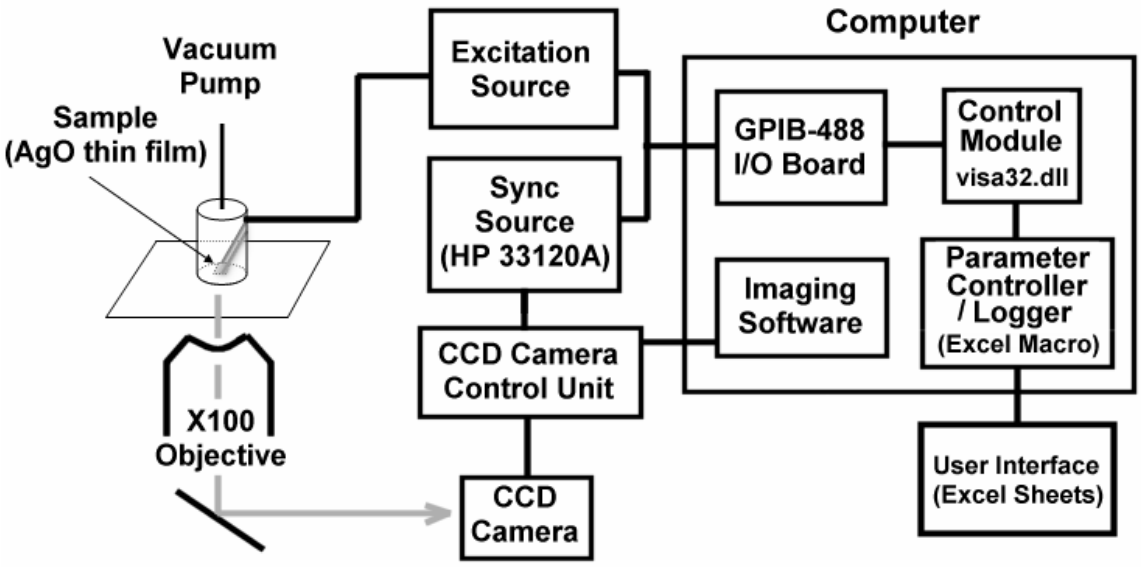

Figure 2-1-1. General experimental schematics. The excitation source is directly controlled by the control software while the imaging device is indirectly controlled by controlling the sync source to trigger the image collection. The sample is under moderate vacuum (10^{-5}torr). The electrical connection to the sample was achieved by placing spring loaded gold plated electrodes on the top of the sample to be forced into the contact by the vacuum.

2.2 Silver oxide film preparation

The silver oxide thin film substrates in which junctions are fabricated can be prepared through 3 different methods. 1) thermal evaporation, 2) RF-sputtering, and 3) chemical bath deposition. The glass cover slips were cleaned by dipping in Norchromix H_2SO_4 solution for one hour followed by rinsing with deionized water. The coverslips were then left in deionized water in a clean beaker which was cleaned in the same manner. The coverslips were then dried in hot oven at 120°C for an hour. The coverslips were then left in an ozonator for two hours. Thermal deposition is carried out on clean glass coverslips in moderate vacuum (< 2 X 10^{-6} torr). Films are formed by heating pure silver metallic wire to get a deposition rate of 0.1 nm/sec using DV-502A thermal evaporator from Denton Vacuum. The shutter protecting the substrate from metal vapor should be opened only after cooling down the metal wire after completely heating the metal wire to get rid of any surface oxide formed on the wire. Then, the desired voltage to get desired deposition rate should be set as fast as possible. This requires several trial and error before getting used to the deposition system. The deposition rate is measured with quartz crystal micro balance. The final thickness was controlled to be in the range of 12~20nm. These thin pure silver films will be rapidly oxidized and yield silver oxide surface.

The second method of silver oxide film deposition is RF-sputtering. In a combined oxygen and argon environment, sputtered atoms from the pure metallic silver target react with oxygen in the plasma to deposit silver oxide

deposition.[131,132] The benefit of silver oxide deposition through RF-sputtering is high control of the final film composition and resistivity according to the RF-power and plasma gas mixture ratio (O_2:Ar). For example, O_2/Ar = 2.0~3.0 at 150~250W RF power can be used to deposit a film of several kΩ to several MΩ final film resistance. At 3.0 O_2/Ar ratio with 250W RF power, the deposition rate is typically about 0.07nm. Typically films of 20nm thickness are deposited on thin glass coverslips for the junction fabrication and subsequent characterization experiments.

The last method of film deposition is chemical bath deposition. The synthesis procedure is well described in the literature[133] which was exactly followed to yield reasonably similar optical and electrical properties of formed silver oxide deposition layer on a thin glass coverslips. The final film thickness is typically in the range of 80~120nm with 10Ω~10kΩ resistance according to the pH of the final bath for film deposition (higher pH yields better conducting and thicker films).

Generally, chemically deposited films are the most heterogeneous, yielding many electroluminescent spots. Thin metallic silver film deposited by thermal evaporation is less efficient in forming electroluminescent nanoclusters. However, thermal evaporation provides very easy method of thickness control. RF sputtering is far less efficient in forming electroluminescent spots compared to other methods. But, it provides very efficient and accurate method of forming silver oxide thin films with different oxygen. RF sputtering also provides the most physically robust films.

2.3 Junction formation

Each silver oxide thin film on glass is made into a ~100μm X 3mm thin strip. A layer of silver epoxy or paint of 1mmX1mm dimension is painted on both ends of the strip to form contact points for gold plated copper electrodes directly attached to power supplier through SMA coaxial cables. Then, the sample is placed under vacuum while the gold plated electrodes are mechanically pushing the silver epoxy electrode layer by the aid of vacuum pressure which is typically 10^{-5} torr. After the vacuum is stabilized, DC voltage is applied to the sample to cause DC current. Starting from 0.00V, the DC voltage is increased at a rate of 0.05~0.1V/sec until the junction is formed, which is indicated by a sudden current drop of typically more than 2 orders of magnitude change to yield tens of kΩ to tens of MΩ final resistance. Figure 2-3-1 shows the typical setup for the electromigration and figure 2-3-2 shows the typical I-V characteristics of electromigration process within the silver oxide thin films. The absolute values of current and voltage strongly depend on initial film resistance and thickness. Typically thick films with high resistance give high electromigration voltages. The initial current is mainly dependent on the initial film resistance.

2.4 Electroluminescence characterization

A variety of excitation methods are used to generate electroluminescence (EL) - DC (Agilent E3646A), AC (minicircuits ZOS-150, ZOS-300 with amplifier

ZHL2010) and two combined pulses of which pulse widths, amplitudes and interpulse delay are independently controlled (Datron 2000). Intensity of electroluminescence (I_{EL}) is measured using CCD camera (Micromax, Roper Scientific) attached to Olympus IX-70 microscope normally with a 100X oil immersion 1.4 N.A. plan-apochromat objective.

The excitation source, the imaging CCD camera and the information logging device are all software synchronized with one master visual basic program (see appendix) controlling the excitation source, sync pulse generator for the camera as well as logging the individual experimental parameters associated with the individual CCD images in a batch of images for each experiment.(figure 2-1-1, figure 2-4-1~2-4-3)

Electroluminescence intensities were measured under different DC voltages, different AC amplitudes/frequencies, and different widths/amplitudes/polarities/interpulse delay of two consecutive pulses simulating one cycle of AC excitation. In the case of two-pulse excitation, the pulse train repetition rate is optimized for the maximum EL intensity. The two-pulse excitation was made by combining two separate pulses from separate channels of one pulse generator. The shape of each two-pulse train was verified with a digital oscilloscope. EL spectra were taken with Acton Research SpectraPro 300i monochromator and Roper Scientific Spectroscopy grade CCD camera. With the interchangeable mirror and gratings in the monochromator, EL images and spectra were taken together for comparison.

2.5 Electrical response measurement

To characterize the junction electrical response, a picoammeter (Kiethley 6485) was used in conjunction with the same setup as in figure 2-1-1. The detailed connection scheme is shown in figure 2-4-1. The picoammeter was placed in between excitation source (agilent E3646A) and sample. The current measurements were recorded with a computer through a GPIB interface. The EL response was also recorded in some cases to compare the electrical and optical response of the junctions under same electrical excitations.

In case of AC and pulsed excitation, a fast current transformer was used as shown in figure 2-4-2 and figure 2-4-3. The induced voltage out of the transformer is the second derivative of the voltage and the first derivative of the current through the circuit.(Appendix) Numerical integration was done with the numerical values out of digital oscilloscope to measure the voltage and current with AC and pulsed excitation.

2.6 Optical characterization of the junction

Mercury arc lamp excitation with band pass filters (UV 360~380nm, blue 460~490, green 510~530nm) was used to study the fluorescence behavior of the junctions. Fluorescence images were taken with various CCD cameras (Roper scientific Micromax and Hamamatsu Orca 3chip color CCD). Lifetime information of nanocluster excited states were obtained using a frequency doubled Ti:Sapphire laser (400nm, <1ps pulse width) at 84.1MHz repetition rate. The time

dependent emission was collected with a micro channel plate photomultiplier tube (MCP-PMT, Hamamatsu R3809) and PC based integrated discriminator/time-to-digital converter/multichannel analyzer (Becker-Hickl TCSPC-630). The setup is shown in figure 2-6-1. One important variable to get proper lifetime information is the electrical signal arrival time to sync and CFD channels in the TCSPC-630. By using control sample (R6G or fluorescent bead) and delay module (Ortec 425A), proper delay of sync signal can be achieved. It should be done in trial and error manner to see the proper fluorescence decay curve out of control samples. With the same delay applied to the sync signal, sample fluorescence decay was measured.

One alternative way to estimate “zero” delay time between sync pulse and signal pulse in the TCSPC board is to use a pulse generator. One 2ns positive pulse of 4V amplitude from Datron200 is split into two ~2V pulses. The two splitted pulses were then attenuated and inverted to -0.3V by using pulse inverters. One of the pulses is then connected to the end of the cable which is connected to the photodiode output when actual experiment is performed. The other pulse is connected to the end of the cable which is connected to the output of the MCP-PMT when the actual experiment is performed. This setup should give a delta function in the photon counts vs time chart. By adjusting the delay, approximate delta function location on the time axis can be achieved. While not accounting for the pulse delay out of the photodiode and distance difference between the photodiode and the sample from the laser source, this position of

the delta function is the time matching “zero” delay between sync and CFD inputs of the TCSPC-630 board.

2.7 Scanning Electron Microscopy (SEM) and Energy Dispersive Spectroscopy (EDS) characterization of the junction

The structure of electroluminescent junctions was characterized with SEM (Hitachi 3500H). The elemental composition around the junctions was determined by EDS. For silver, oxygen, and silicon, the 2.98keV, 0.53keV, and 1.74keV peaks, respectively, were used. The ratio between oxygen and silicon from the glass coverslip substrate was obtained by measuring the amount of oxygen and silicon from fresh pure metallic silver thin films of the same thickness and on the same substrate as those of the junction silver oxide film. The amount of silicon obtained from the junction area was multiplied by the measured oxygen/silicon ratio to get the amount of oxygen from the junction substrate. The mount of oxygen from the substrate was subtracted from the total amount of oxygen from the junction to obtain the amount of oxygen in the silver oxide. The amount of silver was directly integrated from the silver peaks at 1.74keV.

2.8 Photoconductivity measurements

The junction was applied with 5~40V DC voltage and the current was measured while the junctions were under controlled excitation (light source chopped at controlled frequencies) with band-pass filtered mercury arc lamp or

514nm continuous wave laser with a beam chopper or a shutter. The experimental setup is shown in figure 2-8-1.

2.9 Silver nanoclusters conductive path writing

A silver oxide thin film was illuminated with blue band pass filtered mercury arc lamp to photoactivate the surface and form silver nanoclusters. During the photoactivation, the current through the junction was measured under 4~20V DC voltage applied across the film. The fluorescence from the illuminated area of the film was also measured for comparison to the electric current. The experimental setup is shown in figure 2-9-1.

2.10 Two terminal optoelectronic logic gates implementation

Two-pulse train excitation was used to test the optoelectronic logic gates implementation. The first pulse was from one channel of the pulse generator (Datron 2000). One pulse from the other channel of the pulse generator was divided into two smaller pulses which were also divided into two yielding total 4 small pulses. The widths and amplitudes of the 4 divided pulses were controlled by controlling their mother pulse and characterized with oscilloscope. One, two or three of the 4 divided pulses were recombined to give one second pulse to be fed into the sample. The delay between the first pulse and the final second pulse was optimized to give maximum EL output. All electrical wave forms were characterized on a fast digital oscilloscope.

2.11 Photolithographic patterning of electrodes

To work toward true single nanocluster junctions and obtain better controlled shape of the silver oxide film for the electromigration junction formation, photolithographic pattering was used. The mask for the photolithography is shown in figure 2-11-1. The pattern looks like a bow tie and the size of the neck of bow tie is 1micron. Silver metal films prepared on clean glass coverslips (cleaned as described in section 2.2) first cleaned with pure nitrogen gas. Each film is placed on a vacuum chuck of a spin coater. Hexamethyldisalizane (HMDS primer) is then coated for 30seconds at 3500rpm. A drop of positive photoresist (Shipley 1813) is applied to cover 2/3 of the film surface. The sample is then spun for 30seconds at 3500rpm, followed by 10 minutes of soft baking at 90°C. The sample is exposed under the mask for <20seconds to the 220nm UV source with 2~3mW power in the mask aligner. The sample is hard baked for 20 minutes at 120°C. The sample is developed in tetramethyl ammonium hydroxide solution (Microposit MF319). After drying the sample with pure nitrogen gas, the sample is dipped into 1:1 concentrated ammonia and 30% hydrogen peroxide mixture for less than a second. The sample, then, was rinsed with deionized water to check the width of silver metal ribbon neck under an optical microscope. The etching and rinsing steps were repeated until desired ribbon neck width was achieved. Then, the remaining photoresist is cleaned with acetone.

2.12 Experiment for the antibunching of photon stream

For the antibunching experiments, a scanning confocal microscopy setup with a tightly focused laser beam (where the tight beam focus also generates a non-zero z-component at the sample), and two single photon counting avalanche photodiodes viewing the luminescence in a Hanbury Brown-Twiss configuration were used(figure 2-12-1).[126,127] The histogram of detector coincidences separated by time difference t using a PC-based time-to-amplitude converter (TAC) and pulse-height analysis system (TimeHarp 100, PicoQuant). Prior to building the histogram, one has to make sure that the zero delay between the two detection events from the two APDs should be within the window of observation. This zero delay adjustment should be done by delaying the sync signal from one APD to the TAC system. An efficient way to adjust the zero delay for the sync signal is described in section 2.6. The proper delay to the sync signal of Timeharp-100 should be longer than 74ns. For unstable molecules, it is necessary to generate antibunching signals from hundreds of molecules by scanning the stage with very well controlled concentration of the molecules. If the two APDs look at exactly same spot on the sample plane, the sample scanning will still yield an antibunching signature integrated from several hundreds of molecules. CN-PPV (cyanonitrile substituted poly-paraphenylenevinylene) and CdSe quantum rod were used for control experiment. Since the lifetimes of silver nanoclusters are not yet readily accessible with commercially available electrical pulse generators, only short pulsed laser excitation was used to prove the antibunching of photon stream out of silver nanoclusters. The excitation scheme is similar to that described in section 2.6.

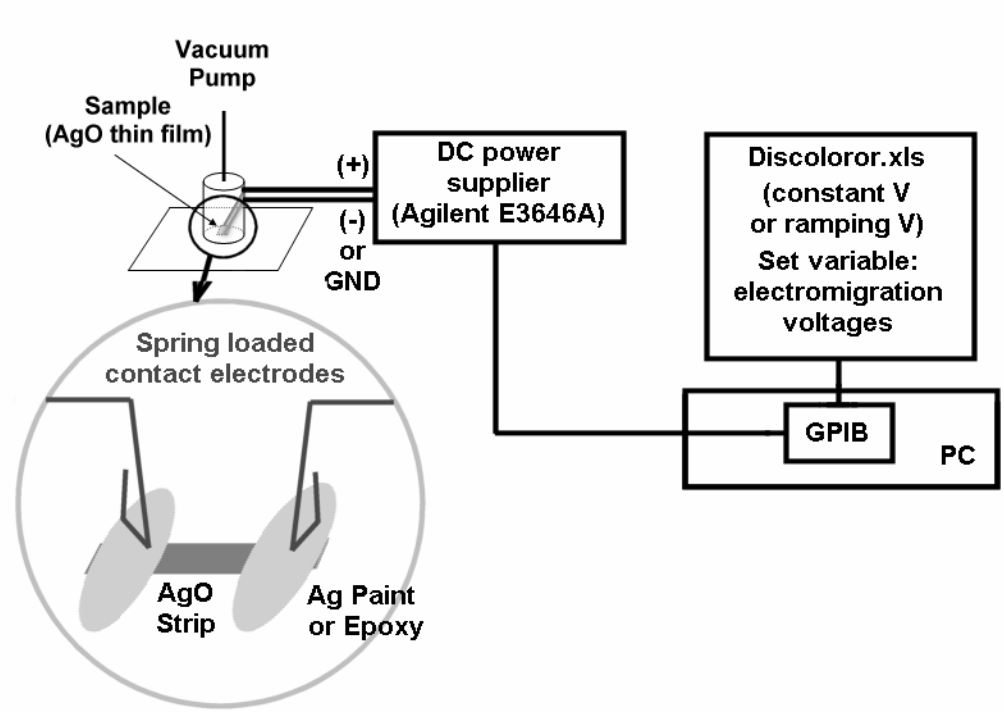

Figure 2-3-1. Schematics of the electromigration process to create the nanoscale break junctions. The whole process is software controlled (discolor.xls). One must suddenly open the circuit following the sudden current drop so that no further junction broadening can take place.

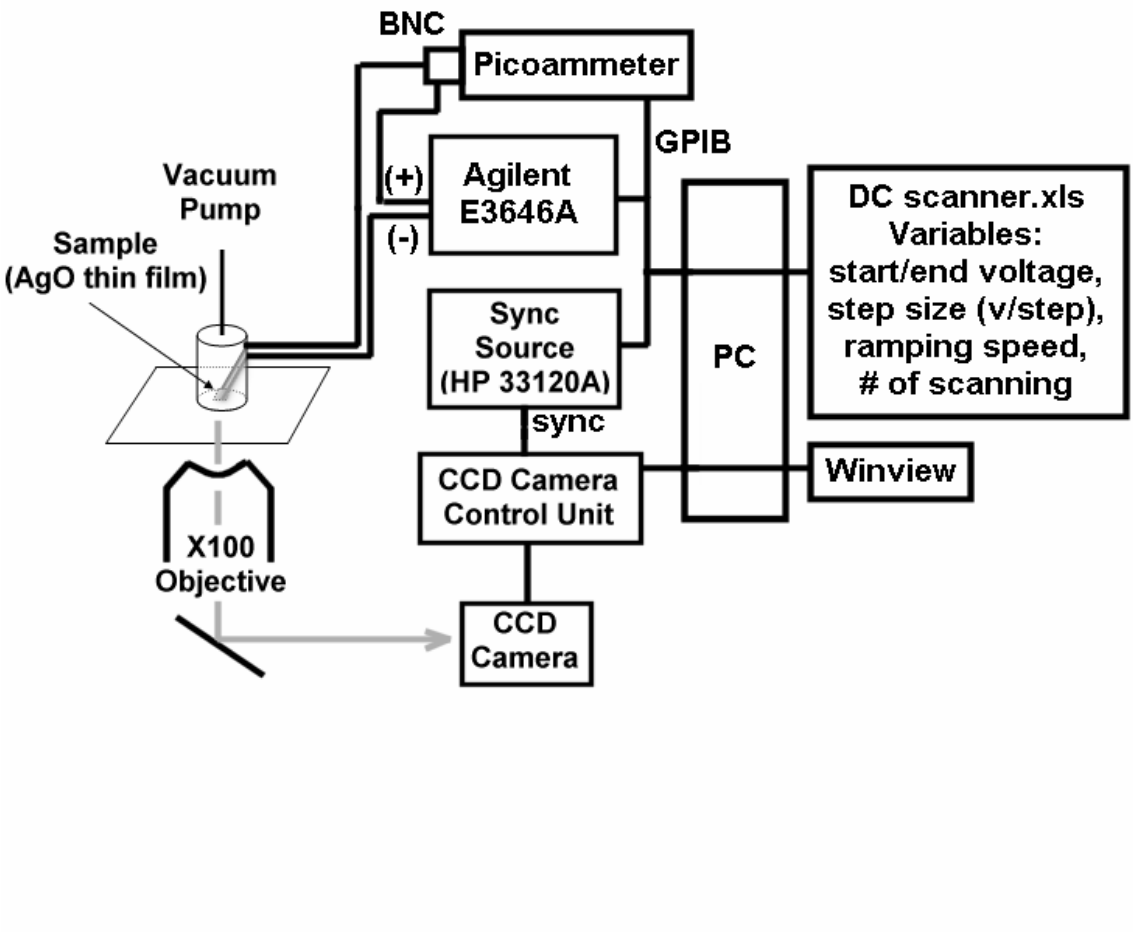

Figure 2-4-1. Schematic of the DC voltage scanning experiment. Voltage to the sample is software controlled (DC scanner.xls). The range of scanning and the number of scans can be set in the software. The electroluminescence image was simultaneously recorded as the voltage is applied to the sample and current is measured.

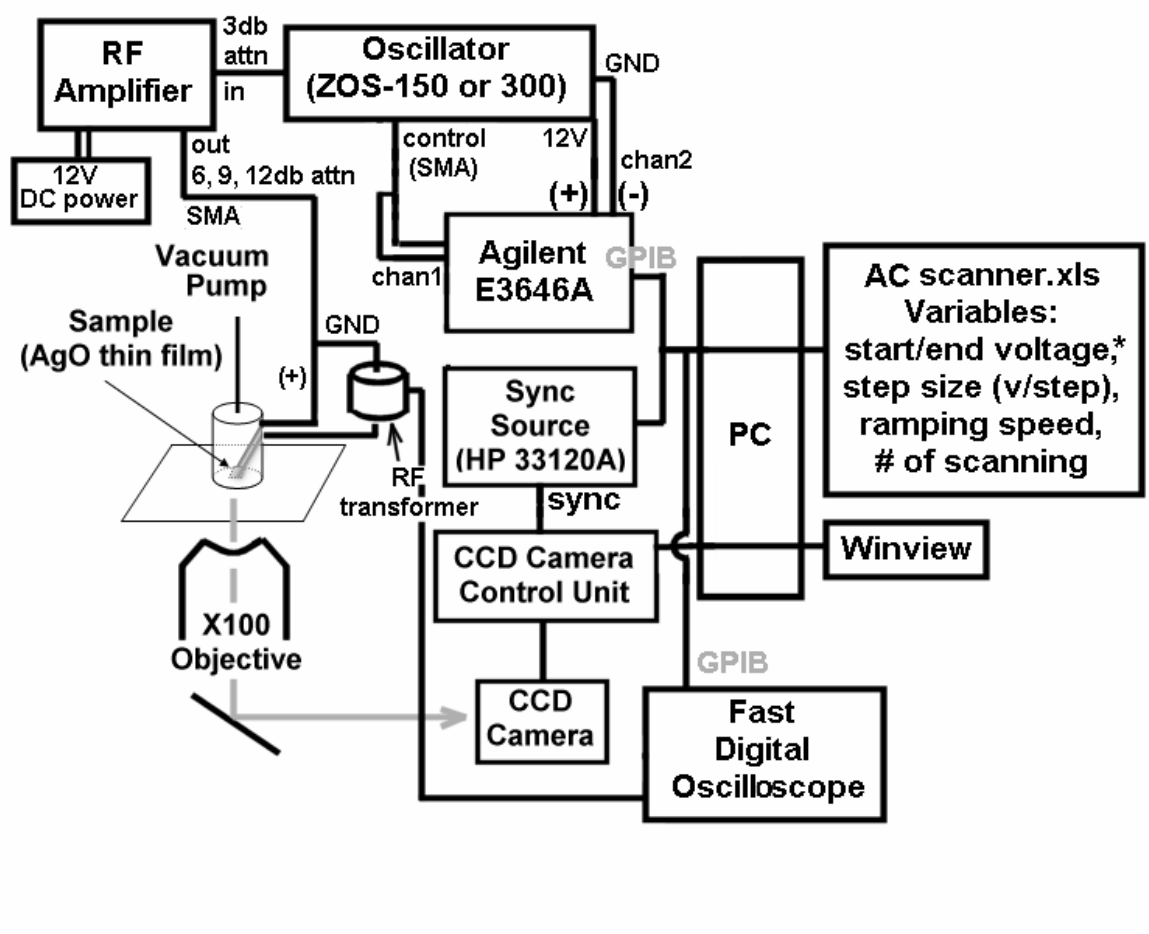

Figure 2-4-2. Schematics of the AC frequency scanning experiment. The AC excitation frequency is controlled by controlling the DC voltage (1~16V) connected to the “control” of the sine wave oscillator (Minicircuits, ZOS-150 or ZOS-300). The frequency calibration curve is shown in the appendix. The output of the oscillator is amplified after 3db attenuator which is necessary to protect the amplifier. The amplifier output is normally attenuated by 6, 9 or 12db to give ±2.5, ±2.0, or ±1.7V final excitation to the sample. Electroluminescence images were simultaneously taken while the frequency was scanned.

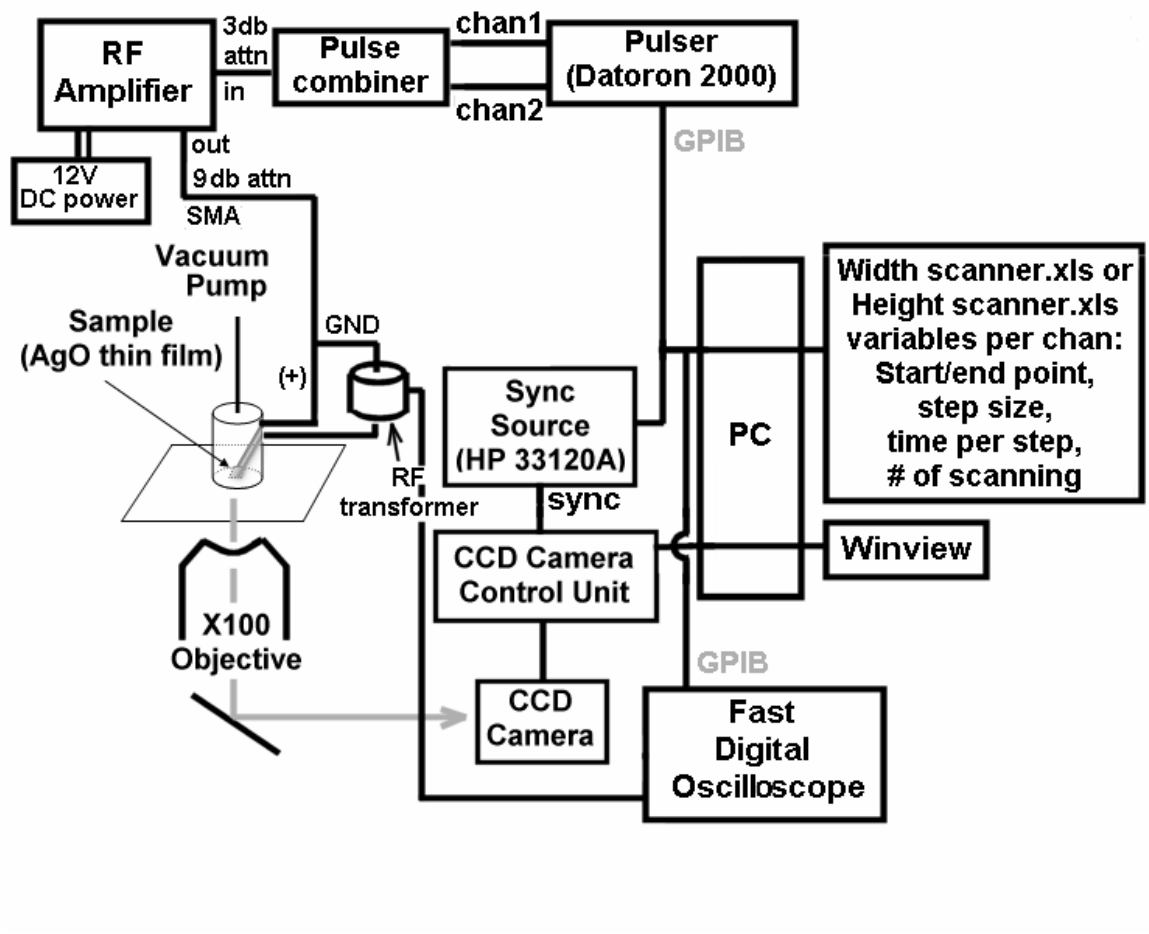

Figure 2-4-3. Schematics of two pulse excitation experiment. Two pulses were generated from the two separate channels of a pulse generator (Datoron2000). Two pulses were then combined together to give one pulse train. Pulse widths, amplitudes, polarities and interpulse delay were all controlled. The electroluminescence images were simultaneously taken while those parameters were changed.

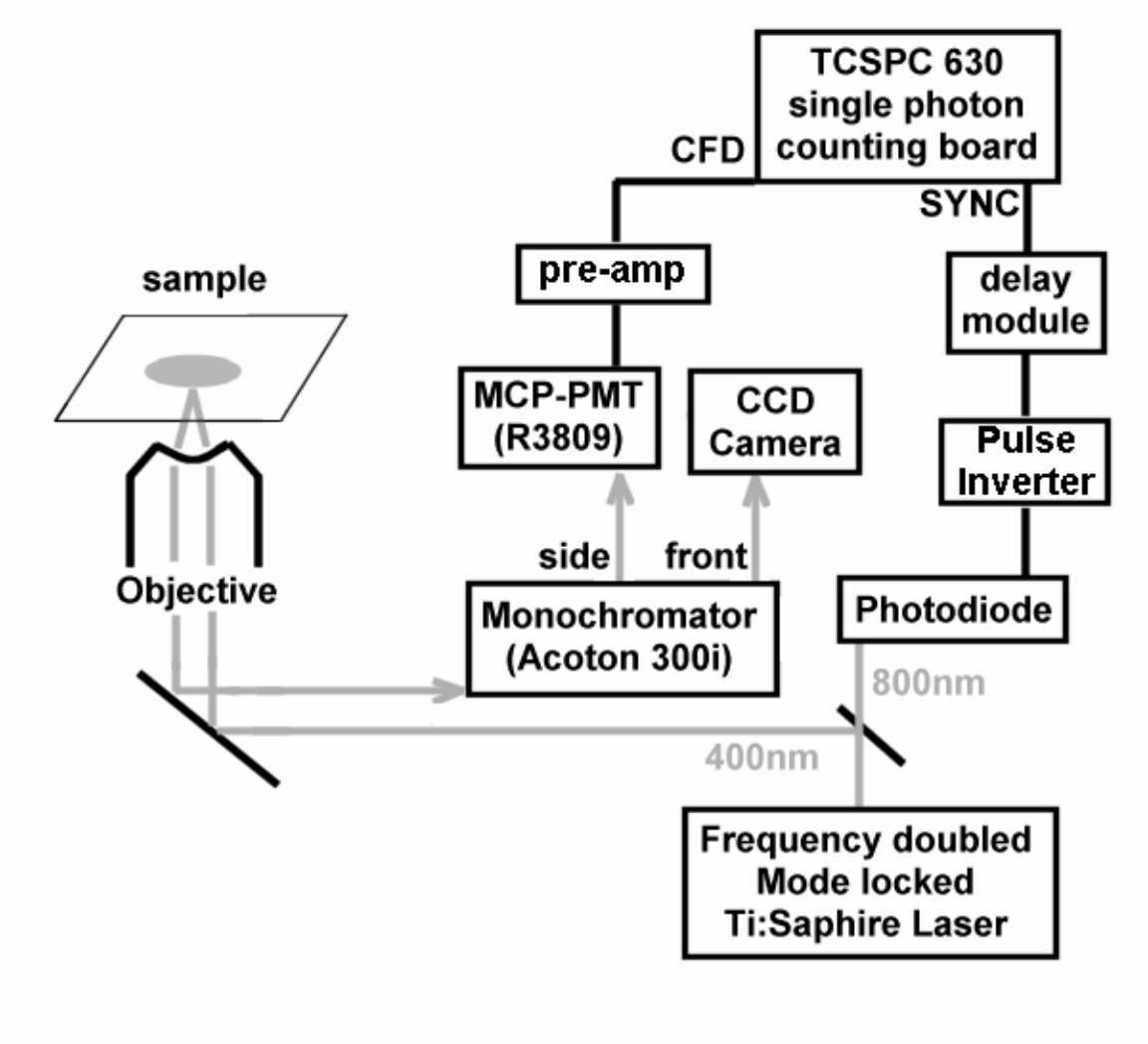

Figure 2-6-1. Schematics of the lifetime measurement setup. This typical lifetime measurement setup was combined with fluorescence wavelength selection through the monochrometer. The fluorescence is directed to the monochrometer through a slit. The fluorescence is dispersed by a grating in the monochrometer. The side port of the monochrometer with a slit, then, can select the specific wavelength range of the fluorescence by using different gratings and changing the center wavelength of the gratings. To calibrate the bandwidth of the selected fluorescence through the side slit of the monochrometer (front slit opens to the

CCD camera), a tightly focused laser spot was used. By adjusting the center wavelength of gratings, one can detect the start and end center wavelengths of the gratings letting the laser spot get through the side slit. The difference between the two wavelengths is taken as the bandwidth of the fluorescence selected by the monochrometer.

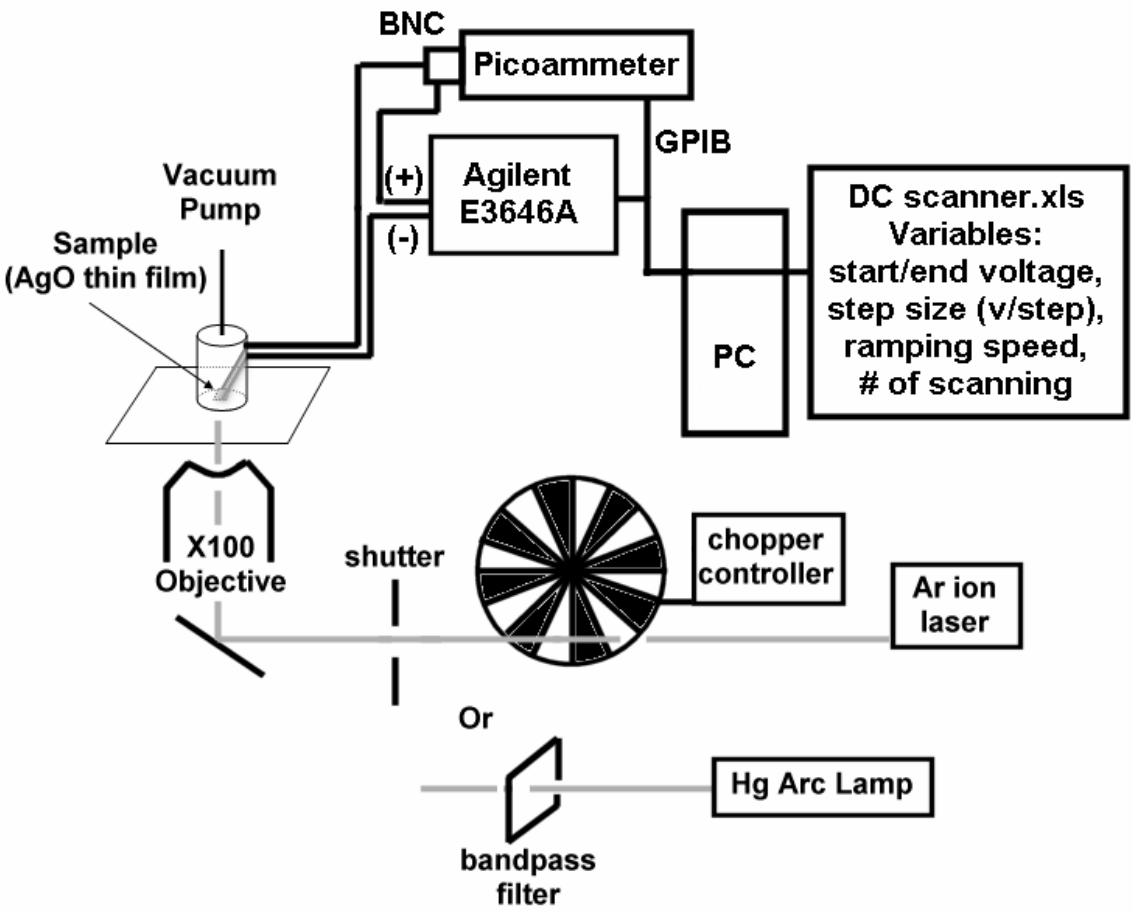

Figure 2-8-1. Schematics of the photoconductivity experiment. An optical chopper (Stanford research systems SR540) or shutter was used to control the illumination. The electric current under constant potential difference was measure and recorded with software while the illumination is controlled.

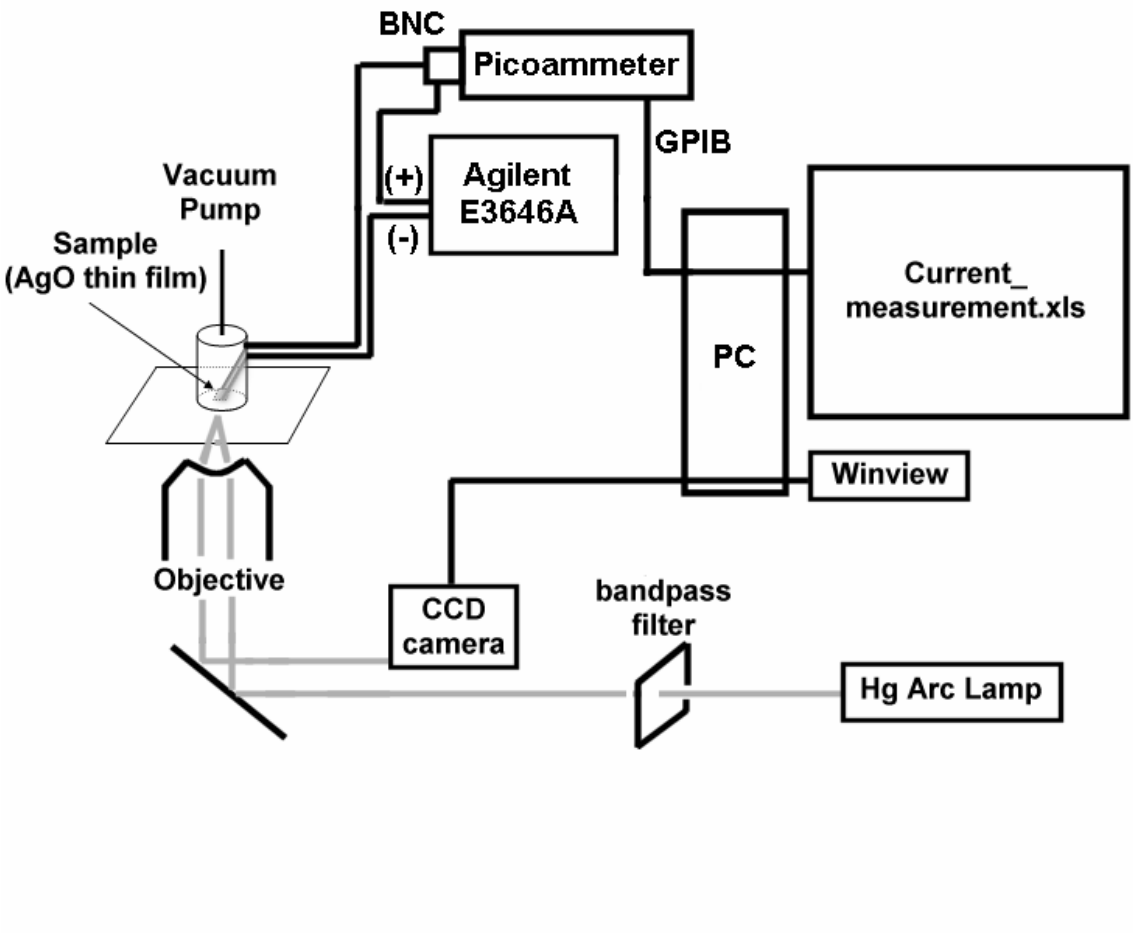

Figure 2-9-1. Schematics of the conductive path writing experiment. DC voltage was manually set so that a reasonable photocurrent is observed. Typically <20V is enough to see <100nA photocurrent with blue band pass filtered mercury excitation. The junction area was illuminated with a band pass filtered mercury arc lamp while the current and fluorescence image were recorded.

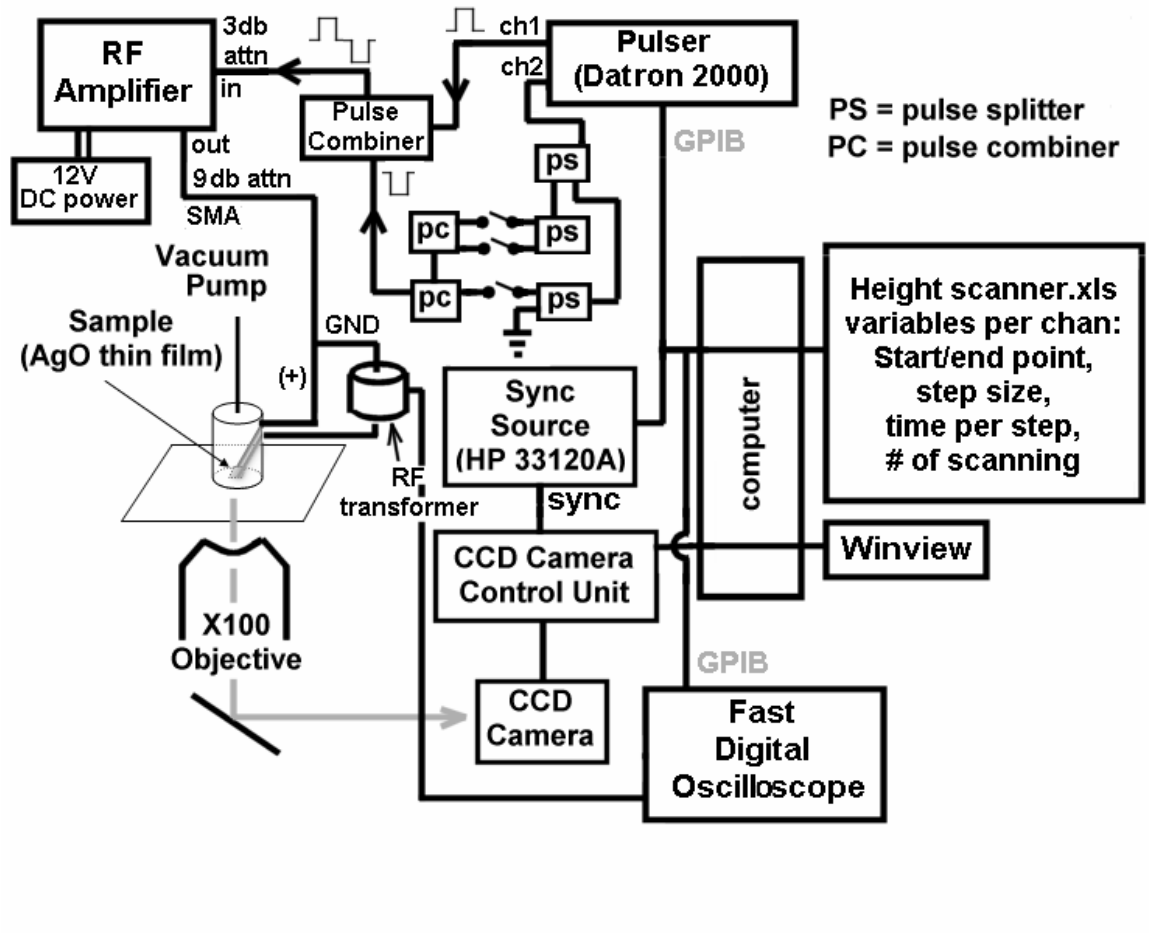

Figure 2-10-1. Schematics of optoelectronic logic operations with silver nanoclusters. One positive pulse (2.2V) is generated from channel 1 of Datron 2000. The second channel generates one negative pulse, which was subsequently divided into 4 equivalent smaller pulses. The final 4 pulses were measured with an oscilloscope to be -1.05V. The three -1.05V pulses out of four pulses were used as three inputs to implement the full adder. The electroluminescence images were simultaneously taken while the input pulses were switched manually.

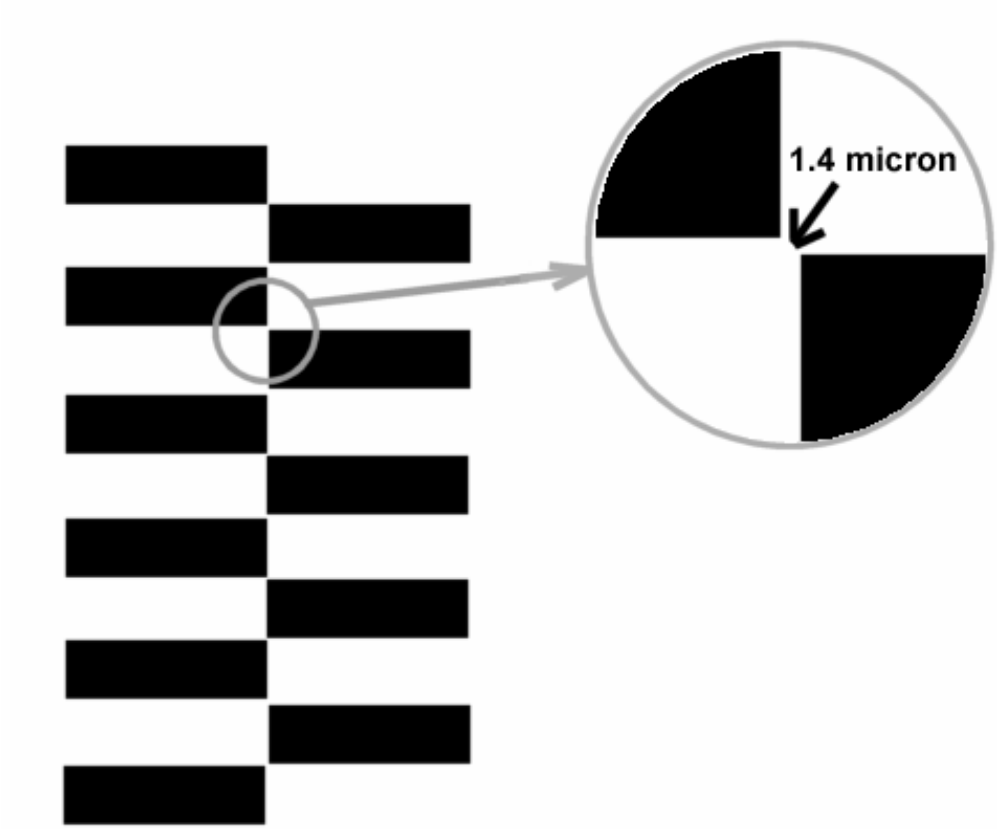

Figure 2-11-1. The mask used to photolithographically pattern the silver thin films to fabricate narrow junctions (~micron). ~5 sets of electrodes can be formed in the effective area for any experiments described here.

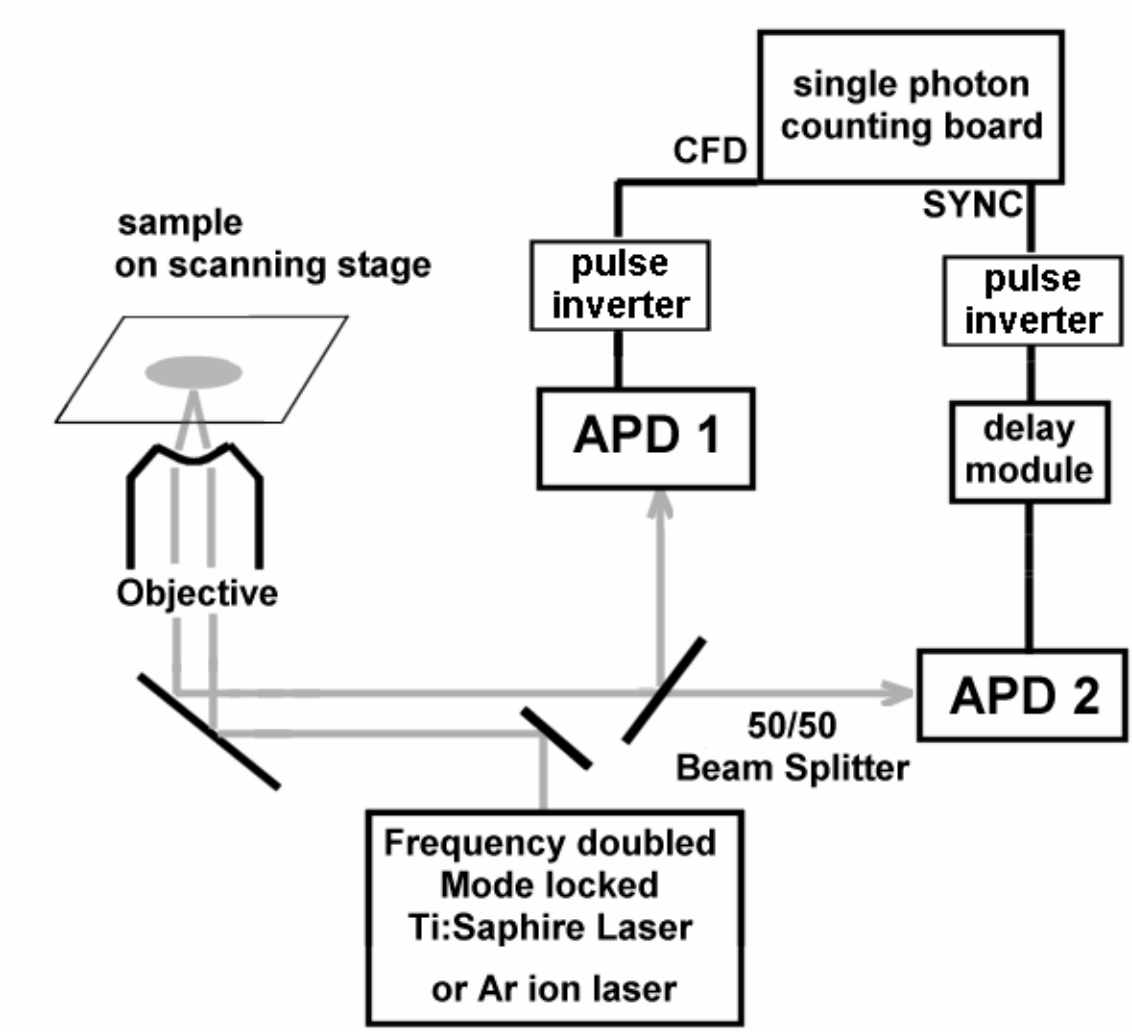

Figure 2-12-1. Experimental setup for antibunching experiments (Hanbury-Brown-Twiss setup). Two APDs were used to detect photons coming from the sample. The delay necessary for the Timeharp-100 photon counting board is longer than at least 70ns. The beam splitter is mounted on the microscope eye piece and connected to optical fibers to couple to the APDs.

CHAPTER III

RESULTS AND DISCUSSIONS

3.1 Junction formation

Nanometer scale junctions were fabricated through electromigration as described in 2.3. From this point, the anode is defined to be the electrode holding the higher potential during the electromigration process. The cathode is defined to be the opposite electrode holding the more negative potential or ground during the electromigration process. According to the SEM images, the junction gap ranges from several tens of nanometers to a couple of hundred nanometers. (figure 3-1-1) The typical threshold electromigration voltage ranges from <1V to >20V according to the initial film resistance and thickness. The typical charge consumption of the electromigration process is about 0.1 C/μm^2 for the cross section of the film. The junction gap and resistance strongly depends on the electromigration conditions. Higher electromigration voltage generally yields the wider junction gap and higher final junction resistance. The electromigration voltage is also dependent on the initial film thickness. Generally, thicker silver oxide films require higher electromigration voltages. Therefore, a thicker film yields wider gap and higher resistance. With a given thickness of initial films, one can control the gap distance by controlling the electromigration voltage.

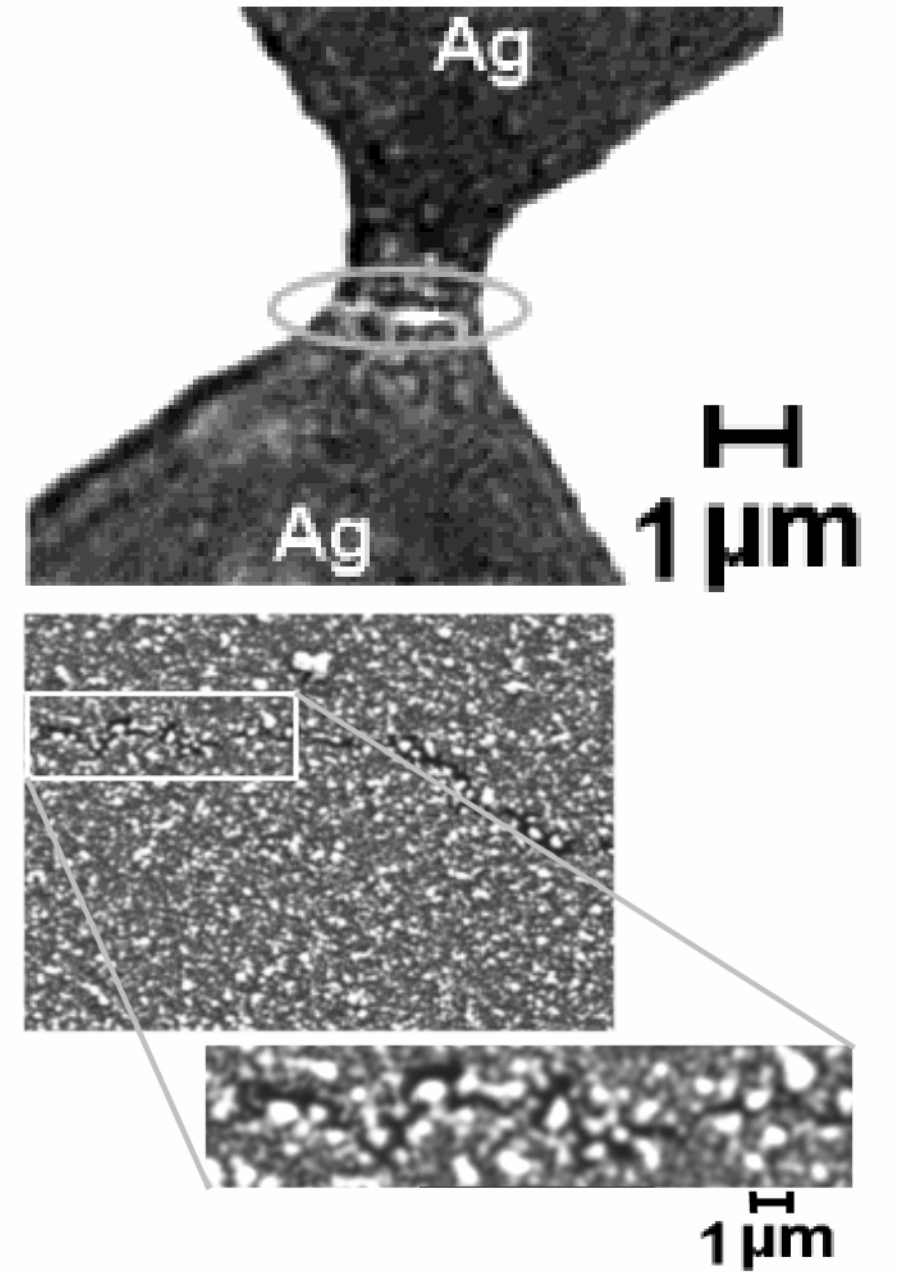

Figure 3-1-1. Nanoscale break junctions induced by the electromigration process. The junction gap ranges from several nanometers to several hundreds of nanometers by controlling initial film resistance, thickness, and electromigration voltages as described in the text.

While these characteristics of electromigration can be applied all silver oxide films prepared by different methods, it is easy to control the variables mentioned above with RF-sputtering method. Therefore, accurately controlled film creation and deposition methods were developed using RF-sputtering system in the MiRC cleanroom at Georgia Institute of Technology. Computer controlled electromigration was performed to create highly reproducible nanoscale break junctions. This consequence of higher electromigration voltage yielding the wider gap size should be attributed to the higher momentum from higher energy electron winds yielding facilitated diffusion and buildup of voids.[103-105] Another variable to control is the initial film resistance (silver oxide elemental composition). Higher oxygen levels in the initial films require higher electromigration voltages, but generally yield narrower gaps than do initial films with lower oxygen contents. This effect can be attributed to the obstructed diffusion of voids in the silver oxide films with higher oxygen contents due to the increased film rigidity generally the case with most metals and their oxides.

3.2 Electroluminescence characterization

DC Electroluminescence

When a DC electric field is applied to the formed junctions, bright electroluminescence is observed(figure 3-2-1).[134] For a given applied field, each electroluminescent spot can produce any of many different colors spanning the

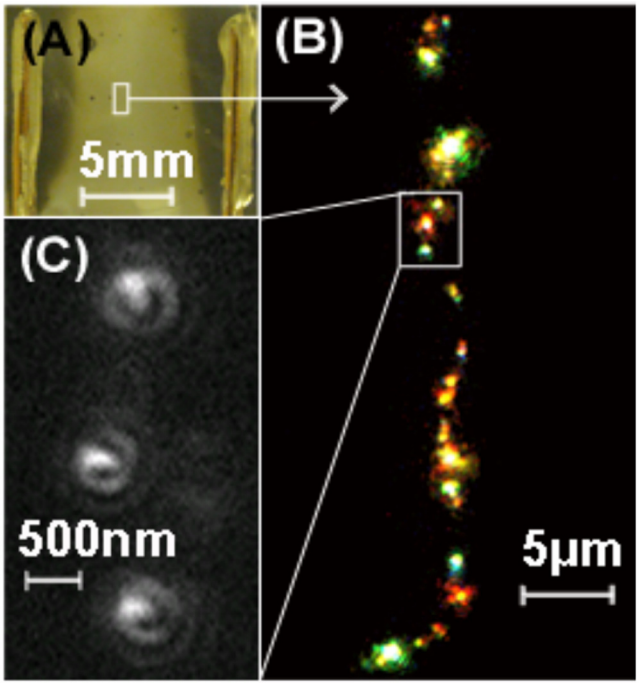

Figure 3-2-1. (A) Electromigration induced junction formed on a AgO film between copper electrodes on a glass substrate in vacuum (~10^{-5} torr). 9 V DC potentials were applied across the film. (B) Multicolored electroluminescence from single Ag_n (n=2~8) molecules occurs within the electrically induced nanoscale break junctions. (C) These features exhibit dipole emission patterns and blinking dynamics (not shown) characteristic of single molecule behavior.

visible spectrum. At all applied DC voltages (3.5 – 15 V), all diffraction-limited spots show both slow, high duty cycle blinking and dipole emission patterns characteristic of single molecules. The electroluminescence intensity shows several peaks as the applied field strength increases.(figure 3-2-2) Also, the current through the junctions was measured to behave similarly to the electroluminescence intensity. The DC electroluminescence of all nanoclusters in the junction shows the spectral range spanning the whole visible range as indicated in figure 3-2-2. The spectra slightly change integrating more and more of higher energy emission as the applied voltage is increased. The similarity to photoactivated single silver nanocluster fluorescence[109,135] suggests that both fluorescence and electroluminescence occur from individual Ag_n molecules. Since each Ag_n molecule has discrete electronic energy levels defined by its size and geometry and current is strongly correlated as EL, radiative electron-hole pair recombination occurs at the Ag nanoclusters within the electromigration induced nanogap junctions. Another interesting property of the nanoscale break junctions made of silver oxide is from that it is composed of very well conducting materials unlike other organic or oxide junctions. Accordingly, these junctions likely have very low dielectricity, which enables very high frequency excitation. Therefore, this narrow recombination zone with good conductors leads to extremely low film dielectricity, which enabled the efficient high frequency AC excitation described in the next section.

The emission caused by DC electric field is not stable and the I_{EL}-V characteristics shown in figure 3-2-2 are not reproducible after one scan. This

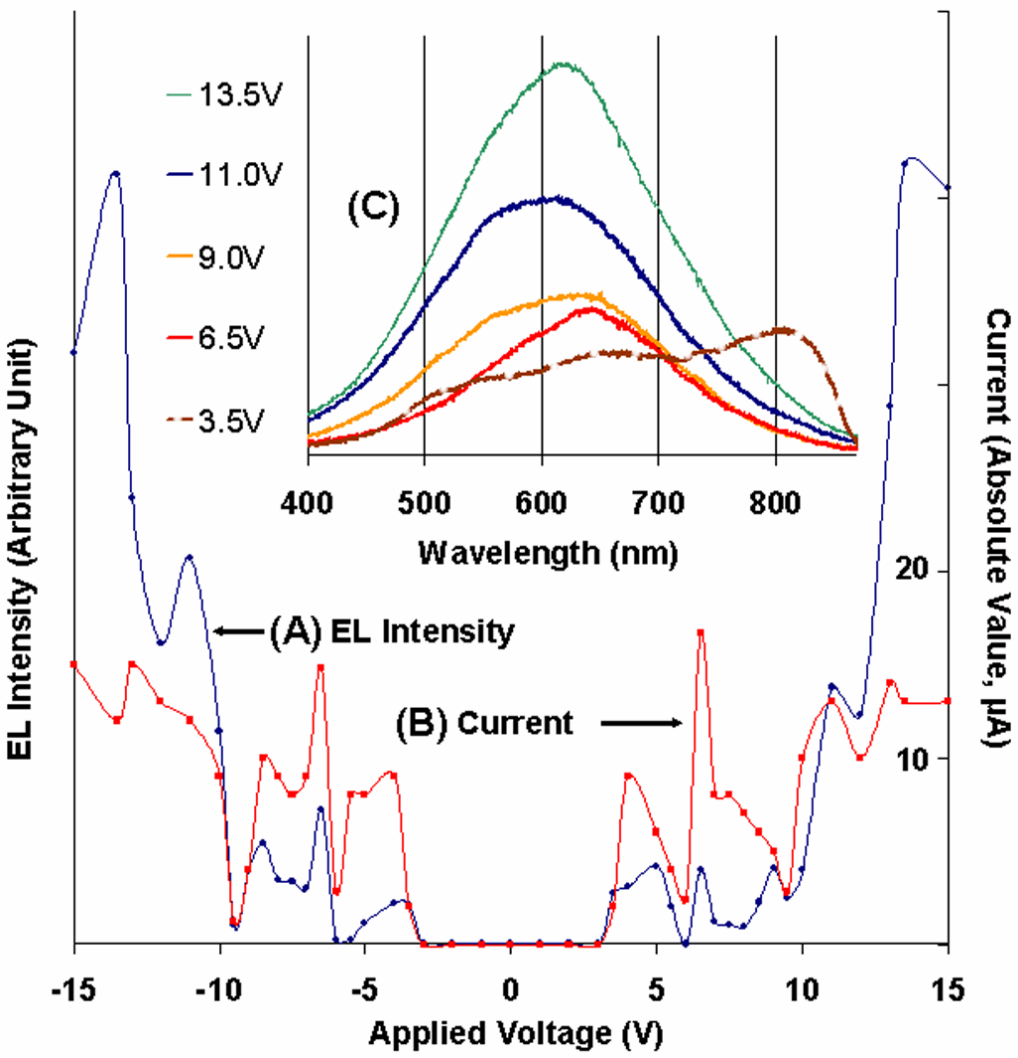

Figure 3-2-2. Typical voltage-dependent (A) electroluminescence intensity from and (B) concomitant absolute value of current flow through all species within the 100μm^2 field of view. Peaks in the emission intensity vs. applied voltage curve result from preferential electron extraction from and subsequent re-injection into subsets of specifically sized and shaped Ag_n molecules. The absolute voltages at which these peaks occur depend slightly on the electromigration process, with electroluminescence onset occurring between 3.5 and 5 V. These processes

result in the correlated conduction and subsequent electron – hole recombination within the Ag nanoclusters. Independent of field polarity and ground level, this must be field-induced conduction and electroluminescence. (C) Electroluminescence spectra (30-sec CCD exposures, 0.15-m monochrometer) corresponding to selected data points in (A) and (B). As applied DC voltage is increased, lower energy features burn out due to Joule heating resulting in peaks in (A) and (B) and corresponding spectral shifts to higher frequencies.

lack of reproducibility indicates that the peaks in I-V curve with DC field are at least partly consumed to change the nature of the junction leading to destruction. The most probable mechanism of this destruction is the thermal destruction caused by the joule heating with the high current density (~1μA/(100μmX50nm) = 20A/cm^2). Thus, the emission out of DC electroluminescence is broadened due to the chemical process that the silver nanoclusters undergo driven by the high current and high field strength. The correlated peaks in EL and current flow arise from thermal destruction and the thermal destruction of the device limits the practical EL experiments to about 15min. Despite the instability, many of the emissive spots show evidence of single molecular emission such as on/off blinking and dipolar emission patterns as shown in figure 3-2-2.

AC Electroluminescence

Formed junctions show very stable and strong emission under AC electric field at the frequency of junction resonance.(figure3-2-2) Although the resonance frequency is ~160MHz in most cases, the junction resonance can range from 130MHz to 200MHz varying with the samples. No systematic variable of electromigration conditions controlling the junction resonance frequency has been found. The resonance frequency is from the RLC component of the junction. One example of the RLC component values was reported.[136] In the example, R is measured to be 45Ω from the on resonance resistance measurement (=I/V, voltage is measured with oscilloscope and the current is measured with a transformer inducing voltage when the AC current is flowing to the sample), C

2.1pF, and L 0.48μH from the resonance peak width of 15MHz at 160MHz resonance frequency ($R=V_{out}/V_{in}$ with both voltages measured with oscilloscope, resonance frequency=$1/(LC)^{1/2}$, and resonance bandwidth = R/L, parallel resonance was assumed to model kinetic inductance of charges and junction capacitance, which independently add up to the total AC response of the system). The efficiency with AC excitation is often 4 orders of magnitude higher than that with DC. Differing from the DC spectra, individual electroluminescence spots that show very broad spectral range (the whole visible range) under DC excitation show markedly narrow spectra under AC excitation (figure 3-2-4) indicating the transitions between well defined local states yielding strong fluorescence. Thus, it indicates that AC excitation yields highly stable fluorescence-like electroluminescence by injecting charge at the optimal times and reducing thermal decay. The AC electroluminescence also shows blinking and dipolar emission patterns (figure 3-2-3), which further indicates that they are single molecular electroluminescent sources. The emission starts at as low as ±0.28V AC (±0.5V AC comparable to the emission under 5V DC) and its strength increases as AC voltage increases. The reproducibility as well as device lifetime is fairly long with AC excitation. The device still emits as strongly as the freshly made ones even after 5 hours of continuous excitation with ±2.0V AC. Therefore, it is concluded that, by using AC excitation, the junctions show extremely bright and stable single molecular electroluminescence. The previous reports of silver nanocluster spectra at low temperature in inert gas matrices[110,111,114,115] and the spectra of dendrimer encapsulated few atom silver nanoclusters[116] at room

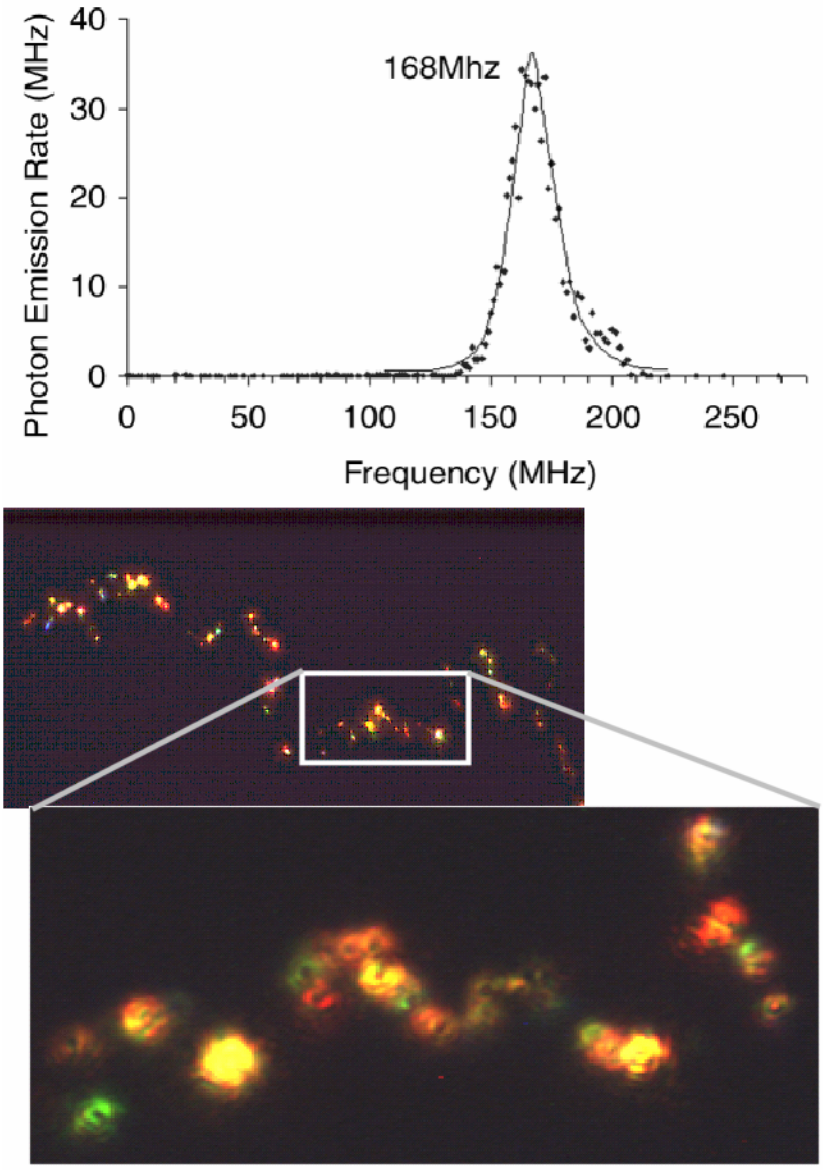

Figure 3-2-3. Typical AC electroluminescence intensity dependence on the frequency. ±2.5V was used to collect the emission from ~100 nanoclusters within a ~20 micron junction length. The emissive spots also show dipolar emission patterns as well as blinking indicating single molecular emission.

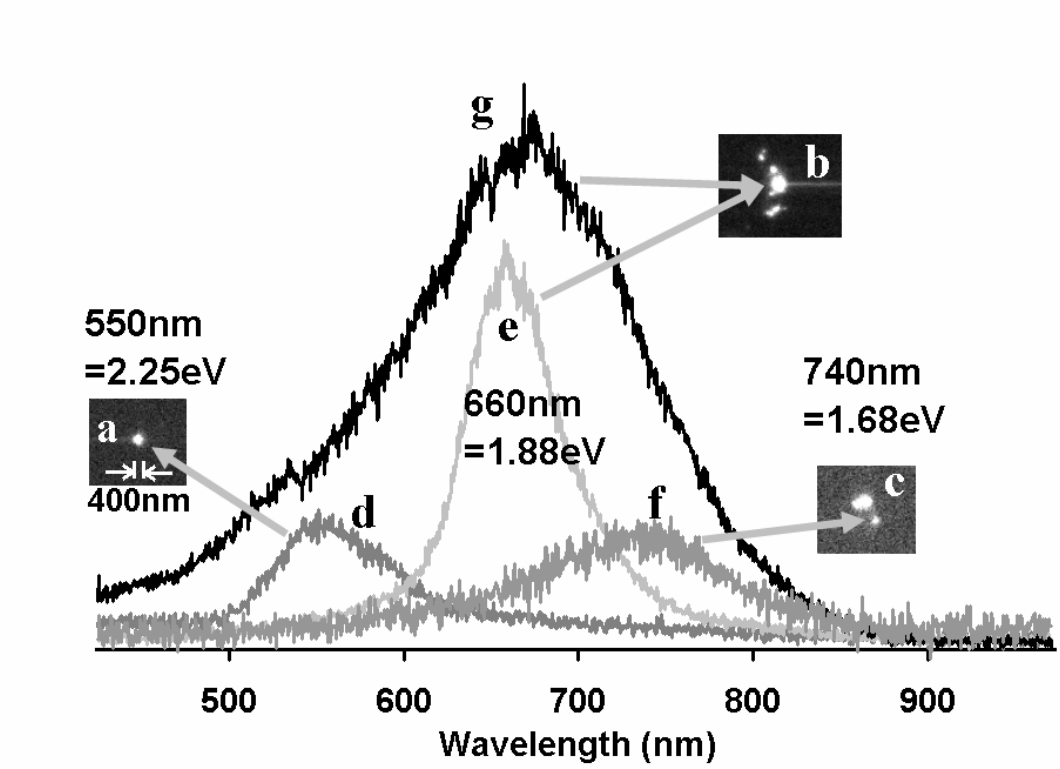

Figure 3-2-4. AC- and DC-excited single molecule electroluminescence spectra. Emission from spatially resolved individual molecules was imaged through a 300-mm imaging monochrometer (Acton) with a mirror in place of the grating. Slit width, position and CCD region of interest were adjusted such that upon rotating a 150 l/mm grating into the path, single molecule spectra are readily obtained. Single molecule images (a, b, c) have corresponding AC-excited (160 MHz, ±2V) electroluminescence spectra d, e, and f, respectively, with emission maxima at 550nm, 660nm, and 740nm (15-sec integration). All AC-excited spectra are very stable. Spectrum f is magnified (3x) so that peak can be clearly seen. The same nanocluster that yields spectrum e under AC excitation yields spectrum g under 7 V DC excitation, the voltage necessary to yield comparable EL intensity. Clearly

DC-excited emission is much broader due to fast spectral dynamics resulting from severe chemical changes in the nanocluster which end up destroying it after several minutes. The 400-nm scale bar in (a) shows that individual emitters yield diffraction-limited images.

temperature strongly suggest that the single molecular emission out of the junction is from silver nanoclusters of which size range from dimer to octamer. Additionally, measured lifetimes of the same electroluminescent nanoclusters under pulsed optical excitation described in section 2.6 (table 3-2-1 and figure 3-2-5) also indicate that these nanoclusters are similar species to those encapsulated in dendrimers.[116] The fluorescence lifetime measurement of the dendrimer encapsulated silver nanoclusters revealed that the nanoclusters (Ag_1~Ag_4) emitting 500~550nm fluorescence have 20~30ps of lifetimes. Based on these similar spectral ranges and lifetimes of the fluorescence, it is concluded that the electroluminescent nanoclusters within electromigration induced nanogap junctions are similar to those encapsulated in dendrimers.

	First component		Second component	
	Intensity	T1 (ns)	Intensity	T2 (ns)
700nm	41%	0.078	59%	1.056
680nm	72%	0.038	28%	0.985
650nm	87%	0.038	13%	0.917
630nm	95%	0.031	5%	0.763
615nm	90%	0.039	10%	0.812
600nm	90%	0.036	10%	0.831
580nm	92%	0.035	8%	0.767
550nm	94%	0.031	6%	0.653
530nm	95%	0.029	5%	0.580
500nm	96%	0.025	4%	0.553
All	63%	0.038	37%	1.035

Table3-2-1. Fluorescence lifetimes of silver nanoclusters formed on the electromigration induced nanogap junctions. The experimental setup is described

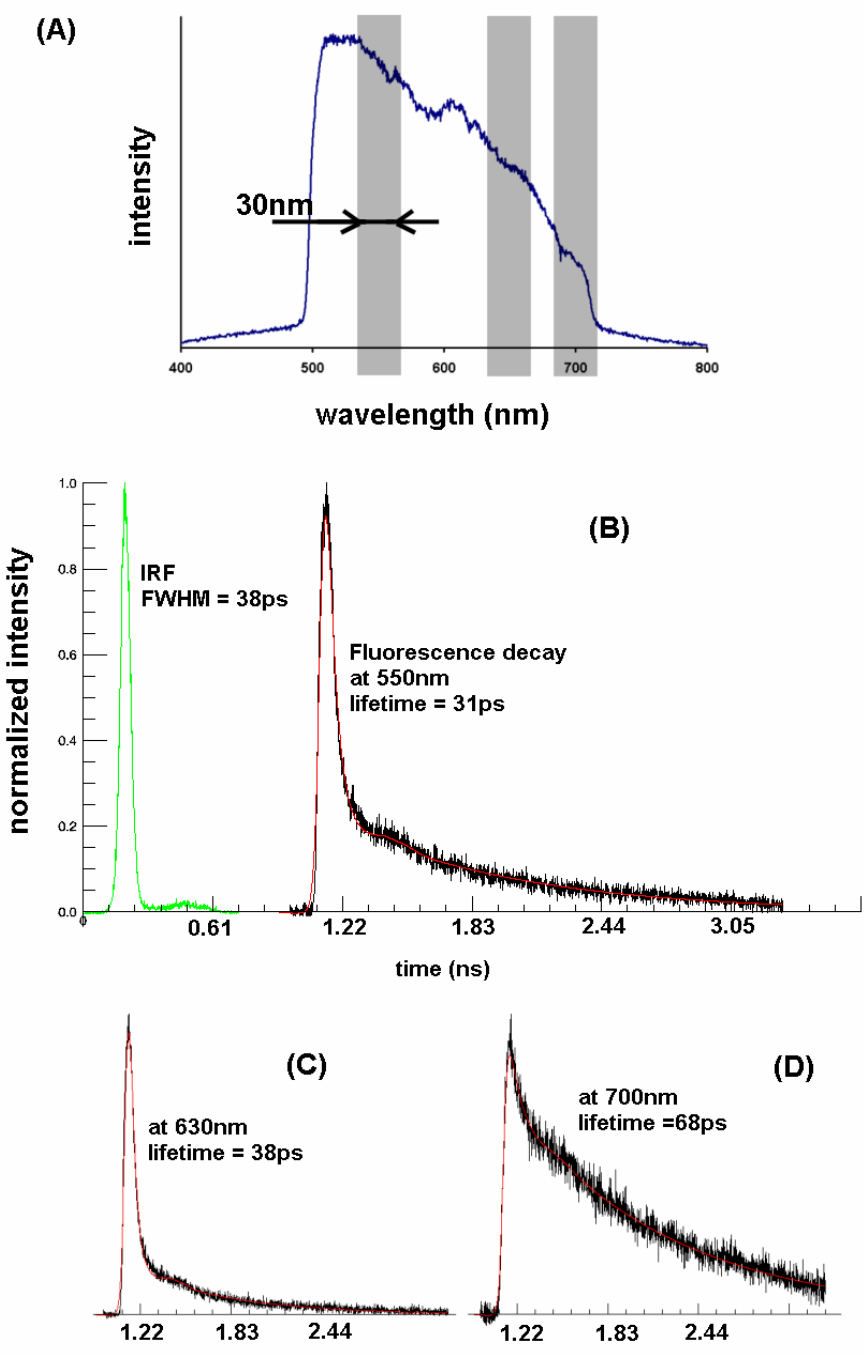

Figure 3-2-5. Lifetime measurement results of surface bound silver nanoclusters formed within the electromigration induced nanogap junctions. 1.35kW/cm^2 laser power was used at 400nm, ~200fs excitation and 84.1 MHz repetition rate. (A) Fluorescence spectrum of multiple nanoclusters formed within the junction. The

~30nm bandwidth of spectral range was selected through a monochromator (Acton Research, SpectraPro 300i) and directed to an MCP-PMT (Hamamatsu, R-3809) to yield the lifetimes of the nanocluster fluorescence. The instrument response function (IRF) was taken by reflecting the attenuated laser beam to the detector. Three different lifetimes of different spectral range are shown here to match the spectral range of AC electroluminescence shown in figure 3-2-4. Other results are also given in the table 3-2-1. Lifetimes were obtained by deconvoluting (deconv.pro in appendix) the IRF from the transient data. Lifetime resolution is a few ps in this setup.

in section 2-6 and the data are shown in figure 3-2-5. The individual spectral ranges are selected by a monochromator and has a bandwidth of 30nm. The intensity ratio between the fast and the slow components is the ratio between the two coefficients of the two exponential components. The fast component lifetimes indicate that these are similar species to those encapsulated in dendrimers.[116] Overall, the radiative lifetimes of these nanoclusters or their full spectral range is ~40ps. The “All” wavelength lifetime information was collected by reflecting the fluorescence with a mirror instead of a grating. Note that there is always a long lifetime component probably from the background fluorescence from the junction and optics due to the broad and strong UV excitation (370~430nm).

Microscopic analysis of the junctions and the electroluminescent species

Electrically formed junctions excited with blue or green Hg arc lamp excitation show strong fluorescence on only one side of the junction indicating their heterojunction nature (figure 3-2-6). To investigate the origin of this junction asymmetry, elemental analysis with EDS was performed. The EDS data show that the anode (i.e. the electrode holding higher potential during the electromigration process) has significantly lower oxygen content than does the cathode. This different oxygen content arises from the asymmetry in momentum transfer from the electrons during the asymmetric DC electromigration process. Although the abruptly formed junctions should ideally shut down the further significant current flow after formation, significant amount of current still continues to flow through the junctions while they are being formed. This

unavoidable high current during the junction formation arises from several seconds of junction formation process time indicated by the current fluctuation. The current fluctuation is due to the initial void formation during the electromigration process followed by the void buildup (figure 3-2-7). The electrons pumped around the junctions during the junction formation, thus, can provide enough energy to cause oxygen adsorption on the cathode side. Although there will also be some degree of oxygen adsorption on the anode side of junction due to the transferred heat from the cathode side, the amount of adsorbed oxygen on anode side is much less than that on cathode side. This kind of current induced oxide formation can also be found with STM experiments in the literature.[137,138] It is also well known that silver surfaces can be oxidized by being heated at lower than ~120°C.[ref] As the junction formation proceeds, the oxygen will keep adsorbed on the junction until the junction spans to the whole current path.

The slightly defocused fluorescence image of the junction reveals that there are many dipolar fluorescence centers around the junction and on the anode side of the junction. The spectral behavior of the fluorescence spots (center wavelengths and spectral widths) match very well with the electroluminescent spectra as well as the silver nanoclusters found in the literature, thus, strongly suggesting that the silver nanoclusters are composed of several silver atoms ranging from dimer to octamer.[109] The dendrimer encapsulated silver nanoclusters also show very similar excited state lifetimes to those of fluorescent/electroluminescent spots on the junctions shown in the figure

3-2-4 as measured with ~200fs laser pulses described in chapter II. These well matching photophysical properties of dendrimer encapsulated silver nanoclusters further verify that the fluorescent spots around the junctions are molecular silver nanoclusters composed of several silver atoms – dendrimer encapsulated silver nanoclusters mainly range from monomer to tetramer as revealed from the mass spectral data.[116] Only these nanoclusters at the junction light up when an electric field is applied and these species exhibit similar colors and dipolar emission patterns to the fluorescence under Hg blue and green excitation.(figure 3-2-8) To investigate the position of the emission centers, overly exaggerated junctions with wide junction gaps (>200nm gap width) were formed and electroluminescence images as well as SEM images were taken.(figure 3-2-9) The image analysis shows that the silver nanoclusters are within the gap – not on either side of the junction. The analysis was done by accurately overlapping a macroscopic feature found both in optical and SEM images.

Electroluminescence mechanism (energy levels and two pulse excitation)

Using the junction elemental analysis and the bridging Ag nanocluster spectral properties, the junction energy level diagram could be constructed using literature values for the absolute energies of all materials – both experimental and theoretical (figure 3-2-10). The shown figure is taking silver trimer as a possible emissive species within the junction. The energy level of the silver trimer is taken from the absorption spectra calculation[117-119], the HOMO energy level with respect to the vacuum is from a mass spectral experiment measuring

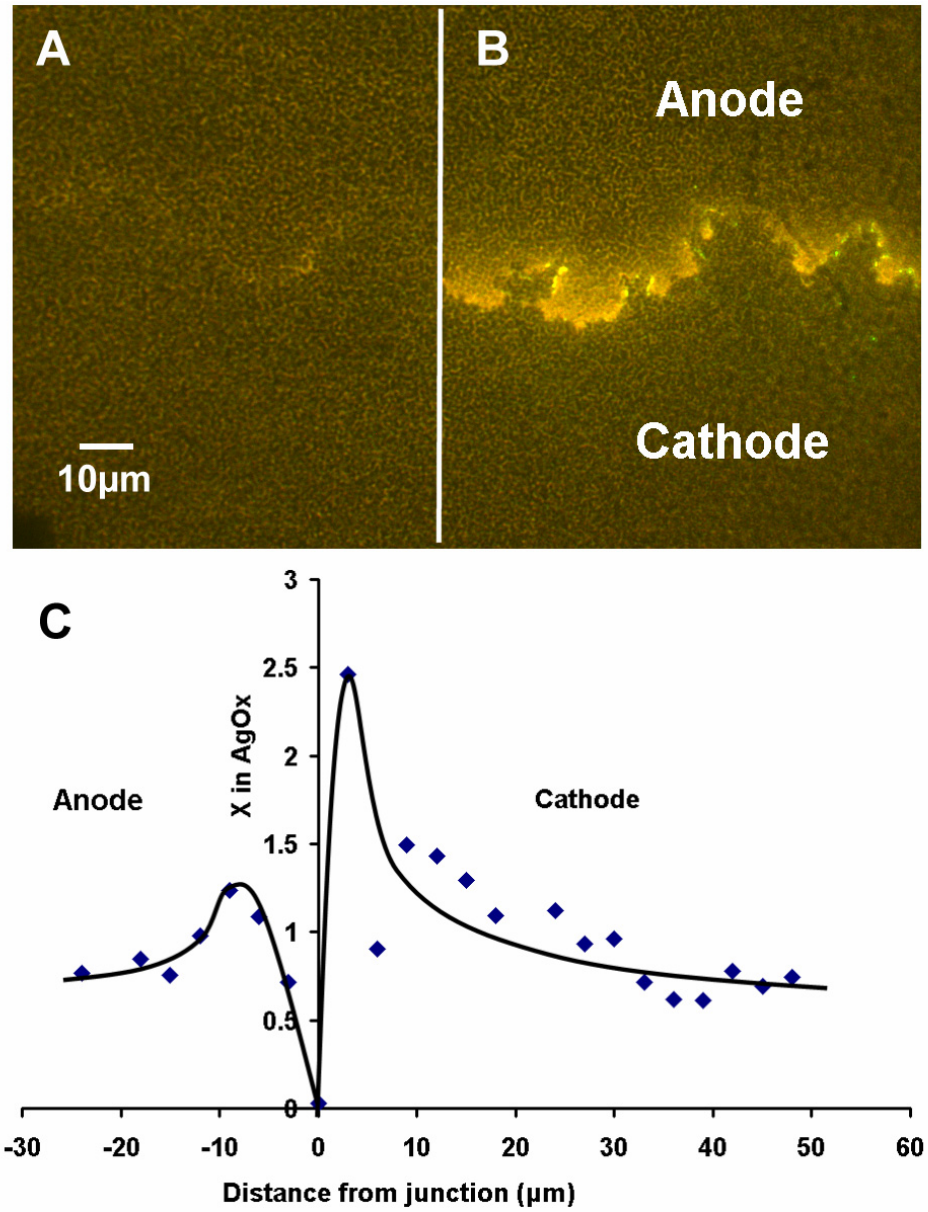

Figure 3-2-6. Typical microscopic images and elemental composition of a nanogap heterojunction made from a silver oxide thin film. CCD images were taken with a 100X 1.4NA oil immersion objective and Hamamatsu Orca 3 chip color CCD camera. (A), Transmitted light CCD image of the junction. No obvious junction is visible. (B), Combined fluorescent and transmitted light CCD image of the junction using room light and band pass filtered mercury lamp excitation

(450~480nm) through a 515nm long pass emission filter. Only the anode side of the junction is strongly fluorescent. The strongly fluorescent nanoclusters within the junction also show EL under an external electric field. (C), Corresponding elemental composition of the junction taken with a Noran EDS system attached to a Hitachi 3500H SEM. The anode has lower oxygen content than does the cathode, thereby yielding the polarity of this junction from the energy level asymmetry.

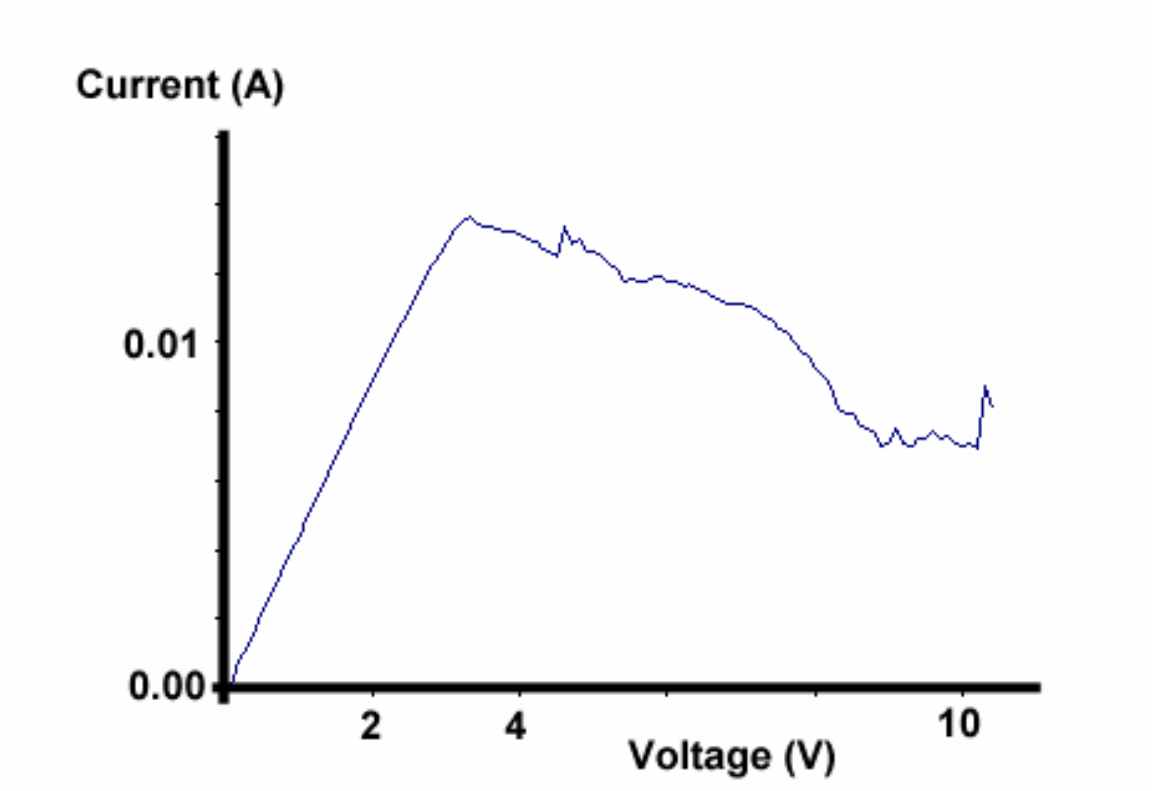

Figure 3-2-7. Typical current behavior during the electromigration process. Ohmic current is followed by severe fluctuation in the current indicating macro scale void formation. The threshold of this behavior ranges between <1V and 20V depending on the initial film composition and thickness. When the void spans the whole current path to form a nanoscale junction, the current is ceased due to the high resistance.

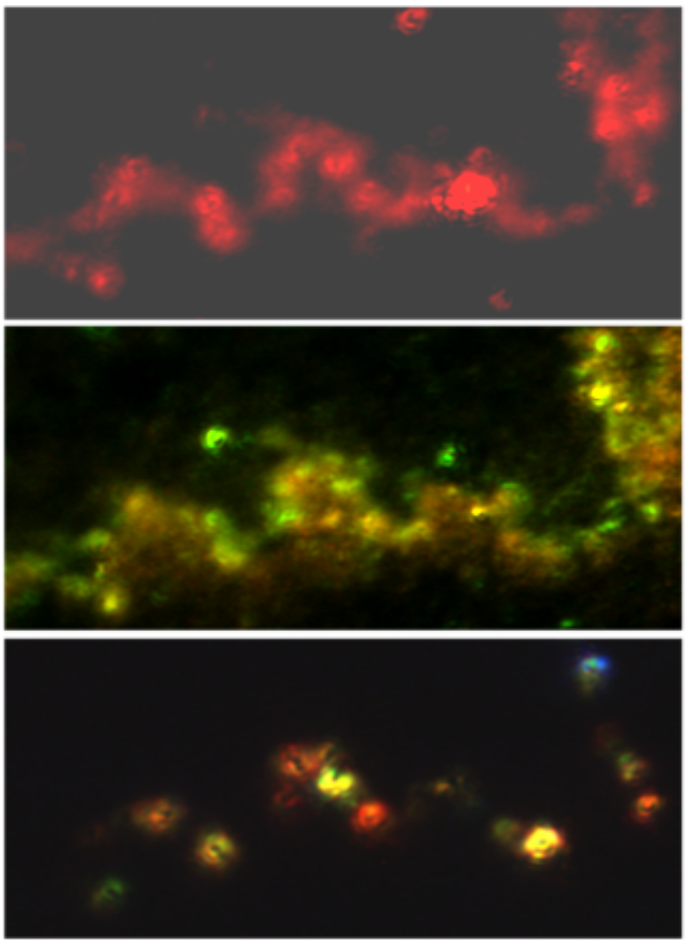

Figure 3-2-8. Typical junction photoluminescence and electroluminescence showing dipolar emission patterns. Although there are many silver nanoclusters showing photoluminescence on the film, those spots only within the junction yield both photoluminescence and electroluminescence. Many of the electroluminescence spots matches well to either green or blue excited fluorescence. It should also be noticed that one side of the junction (anode) yields much stronger photoluminescence than does the cathode.

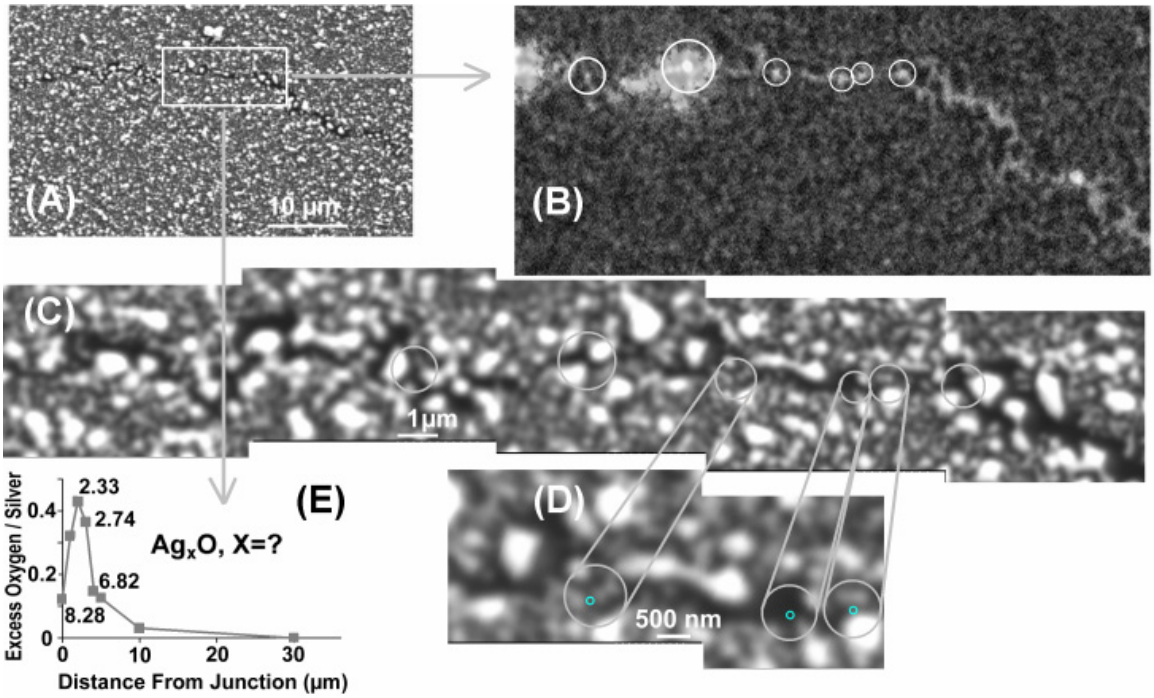

Figure 3-2-9. Microscopic images of a Ag nanocluster junction. (A) Scanning electron micrograph (SEM, Hitachi S-3500H, 15keV electron energy) of a typical silver nanocluster junction. (B) Optical image (0.2-sec CCD exposure collected with a 1.4 NA, 100 X oil-immersion objective) from the region bounded by the white box in (A). White circles represent the electroluminescent areas corresponding to those further magnified in the SEM images (C) and (D). Formed *in situ* by DC excitation,[134] AC-excited emission (163MHz sine wave with $5V_{pp}$(±2.5V) amplitude) arises from species too small to be observed with SEM (<5 nm).(E) Degree of oxidation with distance from the junction as determined with energy dispersive spectroscopy (EDS, ThermoNoran attached to Hitachi S-3500H) from 3-μm diameter regions. The poor EDS spatial resolution was necessary to obtain sufficient signals, but it still clearly indicates a silver rich

junction surrounded by silver oxide between the pure silver electrodes. Numbers on the curve (Ag:O ratio) are the inverse of the y-axis (O:Ag ratio) to more clearly indicate approximate Ag:O atomic ratios in different regions.

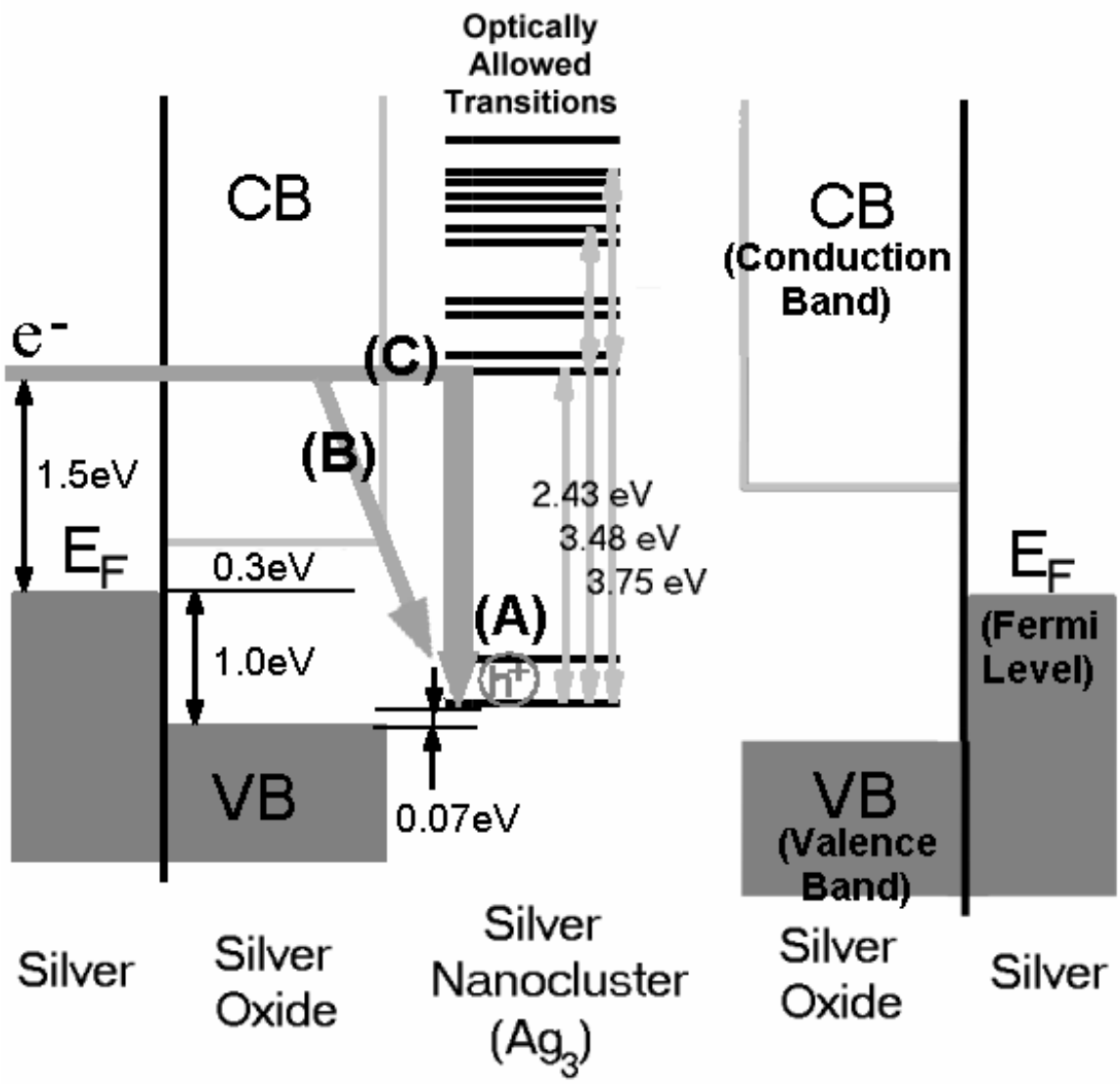

Figure 3-2-10. Composite energy diagram governing silver nanocluster electroluminescence. The photoelectric work function of Ag(111) (4.74eV)[1], x-ray and inverse photoelectron spectroscopy of the Ag_2O band structure[139], gas phase ionization potential (5.66eV)[140] and calculated electronic energy levels of Ag_3[118] are all plotted on the same energy scale to illustrate electroluminescence from silver trimer. Other small nanoclusters also have both visible emission and

molecular energy levels favorable for EL in this device geometry. (A) This diagram shows that holes can be trapped in silver nanoclusters because the hole (h^+) is located within the oxide band gap. After the hole is formed by field extraction, election re-injection causes either (B) non-radiative thermal decay or (C) excited state injection with subsequent emission.

nanocluster ionization potentials[140], the oxide band gap and energy levels were obtained from the XPS/Bremsstrahlung spectrum experiments.[139] Combined on he same relative energy scale with the well-known work function of Ag,[1] a composite junction energy level diagram was constructed. As revealed by the microscopic analysis, the silver nanoclusters are separated from the electrodes to yield a tunneling barrier that should preserve the discrete nanocluster energy levels. While nanocluster levels are gas phase values and AgO/Ag band/energy levels are from bulk, not from thin film data, the alignment is spectacular to yield EL. Taking these as realistic estimates of actual energies, the $Ag/AgO/Ag_n$ (n=3,5, and 9) system is naturally set up for Ag_n EL. The HOMO's of Ag_3, Ag_5 and Ag_9 are within the oxide band gap because the energy difference between the HOMO and valence band edge is larger than room temperature thermal energy (~0.028eV). This nanocluster energy setup for hole trapping/stabilization is crucial to yield electron-hole pair, a necessary intermediate state for EL.

The independence of DC EL intensity and conductivity on polarity and ground level suggests that electroluminescence results from a field dependent electron extraction(hole injection) and subsequent electron re-injection and radiative recombination. Since the electrode spanning Ag_n features are likely ~2 – 8 atoms, or sub-nm in size, the low voltages applied here can readily produce the very large fields necessary for extraction of electrons (~10^8V/m). When an electric field is applied across the junction, both silver cluster ionization and field emission out of the electrode surface can occur due to the high field strength even at 1V (1V/10nm = 1X10^8V/m). Resulting from HOMO levels of some

nanoclusters (Ag_3, Ag_5 and Ag_9) being within the bandgap of the semiconducting AgO electrode surface, some of the ionized silver nanoclusters can be reasonably stable even at room temperature. The combination of a tunneling gap and semiconducting electrodes limits energy level broadening due to interaction with the electrode DOS and enables positively charged Ag nanoclusters to survive until the field emitted electrons from the electrode surface can neutralize them. Some of the field emitted electrons can neutralize them by injecting charges into the excited states, thus, forming excited states of silver nanoclusters yielding electroluminescence when they radiatively decay. The ionization of silver nanoclusters will be referred to be “hole injection”, the neutralization will be referred to be “electron/charge reinjection”, and the radiative decay will be referred to be “charge recombination” from this point.

To verify this suggested mechanism, two-pulse excitation method was used to excite the junction and get the electroluminescence response out of the junction silver nanoclusters as described in the previous chapter. The polarity of the two pulses in one pulse sequence, the interpulse delay between them, pulse widths, and pulse amplitudes were controlled as the experimental variables. The designed role of the first pulse is to inject holes into the nanoclusters and the second pulse should reinject electrons into the nanoclusters, leading to electron-hole pair formation and radiative recombination to yield EL. The formed electron-hole pair should thermally decay or radiatively recombine, only the latter giving electroluminescence. Due to both size and environmental differences, the electroluminescence will exhibit different intensities from individual nanoclusters.

The total EL intensities from all nanoclusters within each junction will also depend on the different set of pulse variables – hole injection time/energy (first pulse width/amplitude), hole lifetime(interpulse delay), and electron reinjection time/energy(the second pulse width/amplitude).

LED behavior of the junctions and two terminal devices

Among the four possible two-pulse polarity sequences, only negative second pulses followed by positive first pulses yield significant electroluminescence (figure 3-2-11). This can be explained with the junction asymmetry evidenced from fluorescence microscopy and EDS as previously described – the anode has higher oxygen content than does the cathode. The different amount of oxygen on either side of the junction causes the different conductivity and different band structures. As measured with macro scale junctions (junction gap was in the same range of dimension as the usual junctions described above, but the film dimension was made wider ~5mm width), each side of the junction shows different conductivity. The cathode side of the junction shows lower conductivity (less than one order of magnitude difference). Different silver oxide films with varying oxygen content were made through RF sputtering to measure the electrical effects of increased oxygen contents so that the band gap can be approximated. Higher oxygen contents in the silver oxide films yield lower conductivity in the range of experiment (Ag:O = 2:1 ~ 1:1 = 0.1 ~ 20MΩ). As the samples were heated, the films with higher oxygen contents also show slower increase in conductivity. These two effects of higher oxygen (lower

conductivity as well as lessened conductivity increase with temperature increase) indicate a higher band gap with increased oxygen content. Therefore, the band gap of the cathode oxide must be wider compared to that of the anode oxide. Accordingly, the higher conductivity of anode will make it easier for charges to flow back and forth between the nanoclusters and anode oxide. The first pulse extracts electrons out of silver nanocluster HOMOs. If a positive pulse is applied, the electron will be extracted to the anode side. When a subsequent negative pulse is applied to the junction, the anode will be filled up with electrons to reinject charges into the excited states of silver nanoclusters. With the opposite pulse sequence (negative followed by positive), the charges have to flow back and forth between the cathode and the nanoclusters which is less efficient than that between the anode and nanoclusters due to the wider band gap or lower conductivity of the cathode – or, more efficient coupling between nanoclusters and the anode than is between nanoclusters and the cathode. If the same polarity pulses are used (positive-positive or negative-negative), the second pulse would be canceled with the junction oscillation caused by the first pulse since the pulse widths are in the range of junction RLC resonance frequency (130~200MHz varying with the samples). Therefore, more tightly coupled with the anode, silver nanoclusters will electroluminesce with positive-negative pulse sequence because electron reinjection into the excited states of silver nanoclusters from the anode should be achieved with negative pulse while electron extraction from the nanoclusters does not depending on the positive pulse polarity. Consequently, the necessity of having a negative electron

reinjection pulse (or negative second pulse) yields the LED behavior of the junction nanoclusters according to the second pulse polarity. Since the first pulse is necessary to extract electrons from the junction nanoclusters, it can be used as a gate pulse which makes the junction nanoclusters an LED for short period of time while holes are trapped in them – or, while they are still ionized.

After maximizing the electroluminescence intensity by controlling the pulse widths and interpulse delay, the pulse amplitudes were also controlled to further modulate the emission intensity. The maximum EL intensity was consistently achieved with ~3.2ns first pulse width, ~3.2ns second pulse width, and <3.2ns interpulse delay limited by the pulse widths. This optimal electroluminescence excitation waveform with the above pulse widths and interpulse delay is associated with the junction resonance frequency, and it changes in the same manner as the resonance frequency changes (if junction frequency goes up, the widths and interpulse delay gets shorter, to yield the similar shape to the sine wave that will resonate with the junction). At the pulse widths and delay of the highest EL efficiency, pulse amplitudes were changed to see how the EL efficiency changes. Results are plotted in figure 3-2-12. The EL intensity in the figure 3-2-12 is the summation of >100 silver nanoclusters within a simple nanoscale junction. As shown in the figure, the junction electroluminescence shows exponential increase as the second pulse gets more negative than -2.1V. As already explained earlier in this section, the positive second pulse doesn't yield any noticeable EL. Thus, this is LED behavior achieved by using the two pulse excitation. As suggested in the EL mechanism and two pulse excitation

scheme, the first pulse is supposed to inject the holes into the nanoclusters while the second pulse is supposed to reinject charges to the excited states of the silver nanoclusters to form electron-hole pairs. Due to the better coupling of the nanoclusters to the anode compared to the cathode as explained earlier, only a positive first pulse followed by a negative second pulse to the anode can inject holes and reinject electrons to the excited states of silver nanoclusters yielding electron-hole pair leading to radiative decay or electroluminescence. Another factor yielding this high frequency polarity dependence is the asymmetric distribution of nanoclusters with energy levels more closely tied to those of the anode. Due to the asymmetric material flow during the electromigration process, silver nanoclusters are likely closer to the anode, and are, therefore, more tightly coupled to the anode.

By using the two pulse excitation method, one can observe the LED behavior from the junctions by using the second pulse as the bias with constantly added positive first pulses for hole injection. Without the first pulses, the second pulse with reasonable amplitude does not yield any noticeable EL indicates that the first pulse is necessary to yield not only the diode behavior but also EL. In a sense, the first pulse can be considered to be a gate pulse to make the nanoclusters ready to be diodes within several nanoseconds when the subsequent second pulse or the bias pulse is applied. Thus, these nanoclusters can act as a two terminal transistors with electroluminescence output by using the first pulses as gate pulses and the second pulses as bias pulses. Only when

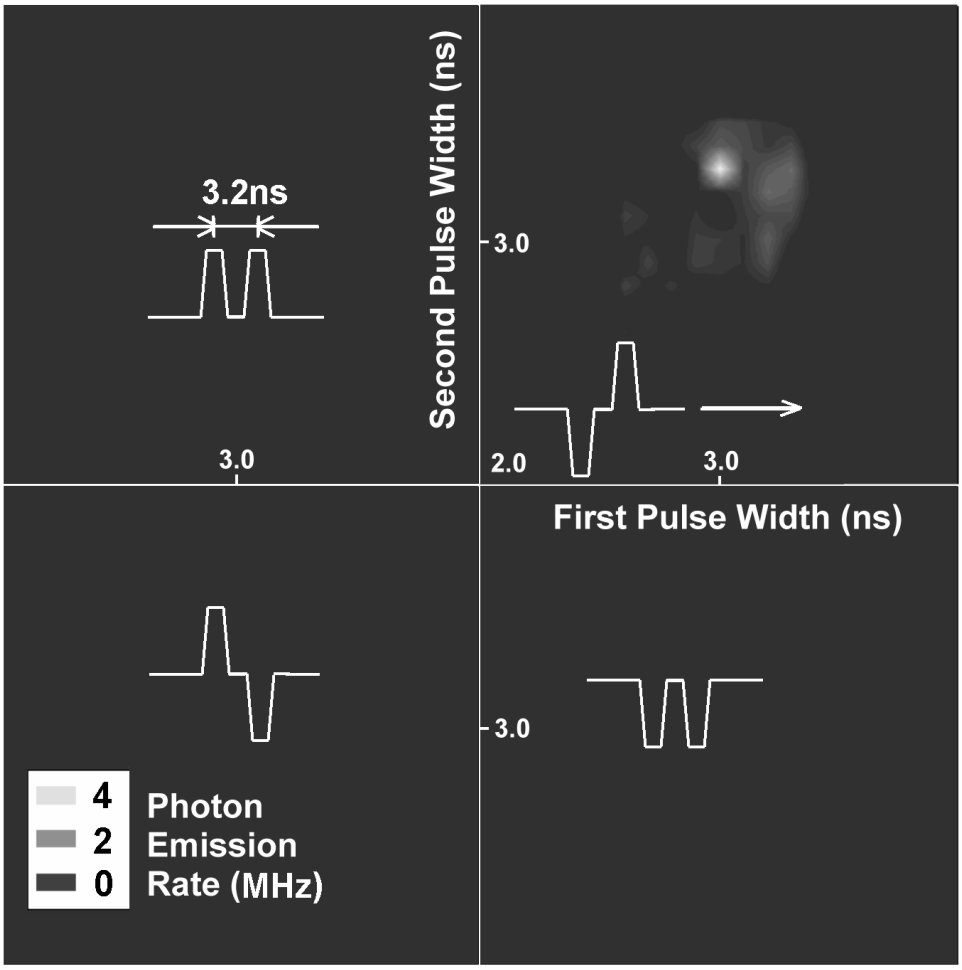

Figure 3-2-11. Typical EL intensity characteristics under various two pulse excitations. EL intensity vs 1st and 2nd pulse widths and polarities (both pulses were of 2.5V amplitude with 3.2-ns interpulse delay at 33MHz repetition rate). The 3.2-ns interpulse delay was chosen because it gives the highest EL intensity. Only positive pulses followed by negative pulses give detectable emission out of all possible pulse widths, polarities, and interpulse delays. The brightest emission was seen with a 3.0-ns first pulse, a 3.3-ns second pulse and a 3.2-ns interpulse delay.

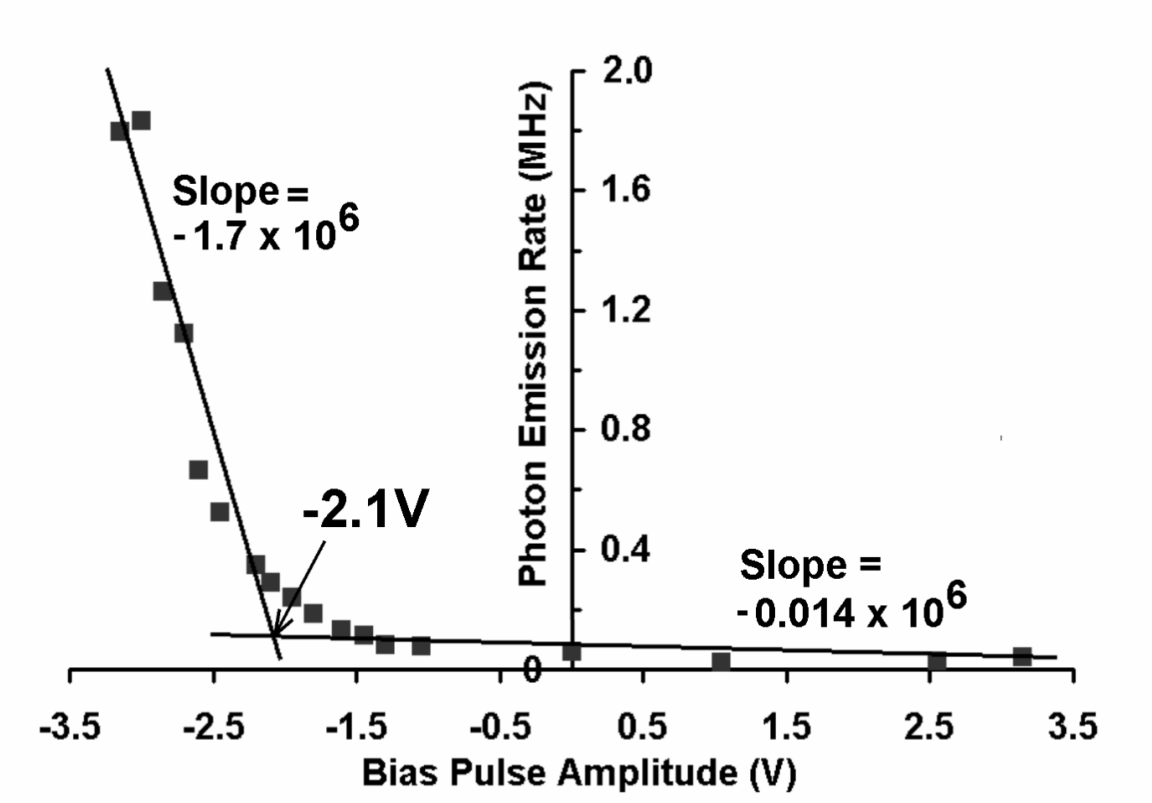

Figure 3-2-12. Typical EL intensity vs. negative second pulse amplitude with 2.5V positive first pulse at 40MHz repetition rate. Pulse widths and interpulse delay were 2.8ns and 4.0ns respectively. With increasingly negative second pulse (bias pulse) amplitude, all individual nanoclusters and, therefore, the entire electroluminescent silver nanocluster junction show LED behavior with a -2.1V threshold voltage. A change in slope of more than 2 orders of magnitude occurs at the threshold voltage.

the first pulses are applied, the second pulses yield LED behavior from the nanoclusters.

Single molecule LEDs

By reading out the responses of spatially resolved individual electroluminescent nanoclusters, the distinctive EL characteristics of individual silver nanoclusters become evident. The individual nanocluster responses differ significantly from the bulk behavior from all nanoclusters in the junction (figure 3-2-13). The figure shows the EL intensity behavior of 5 similarly behaving nanoclusters within one junction with upon varying the second pulse (bias pulse) amplitudes. As the second pulse amplitude increases for a constant 1.6V first pulse, four distinctive peaks are observed at -1.6V, -2.1V, -2.4V and -2.9V. Consistent with the suggested EL mechanism as hole injection with the first pulse followed by the electron reinjection with the second pulse, these peaks in the EL intensity should be related to the excited states of the silver nanocluster.

According to the suggested mechanism, the EL intensity should be proportional to the tunneling current from the electrode to the excited states of silver nanoclusters, provided that the first pulse is first applied for hole injection. As the quasi Fermi level of the anode increases with the increased second pulse amplitude, more channels for charge reinjection through the upper levels of silver nanocluster excited states should be added to the total charge conduction paths as in the Landauer conduction formula introduced in section 1.3. As a reminder, in this most referred formula in molecular electronics, electric current increases

stepwise as more channels for conduction is added to the total current paths. Conduction channels can be charging, scattering, or tunneling channels. As a result, the EL intensity in this junction should keep increasing stepwise as the second pulse amplitudes increases so that more tunneling channels (more Ag_n excited states for tunneling) can be available. The peaks in the $dI_{EL}/dV_{2nd\ pulse}$, therefore, should match the absorption spectra of the silver nanocluster instead of I_{EL}. However, the tunneling electrons have a narrow energy distribution because they are field emitted - the nanoclusters are separated from the electrodes by a tunneling gap and semiconducting silver oxide layer. Therefore, the electroluminescence intensity should be directly proportional to the overlap of the narrow energy distribution of the field emitted electrons and the silver nanocluster excited states. The field emitted energy distribution can be approximated from the Fowler-Nordheim theory of field emission which is described in chapter I.[42,66] According to the literature with detailed theoretical information about FN theory, the field emitted electrons from the metal surface can be made to have very narrow energy distribution. For example, at 300K, under 10V/10nm field strength, the FWHM does not exceed 0.15eV in the energy distribution of field emitted electrons out of the bare metal surface with a 4.5eV work function. The FWHM increases up to 0.2eV as the field strength increases to 30V/10nm. This theoretical distribution of field emitted electron energies can be formulated as in equation 1-4-1. Treating $\frac{df(E)}{dE} \cdot T(E)$ as the silver nanoclusters density of states enabling transmission of electrons, equation 1-3-1 can be combined with equation 1-4-2 to yield equation 3-2-1. Equation 3-2-1

describes the tunneling probability of field emitted electrons through the molecule at a certain energy level E. With applied voltage V, the range of quasi Fermi levels expected to give a net current from the anode to silver nanoclusters would be from E_f - eV/2 to E_f + eV/2 assuming the two electrodes being two parallel metal plates facing each other. Constant density of states in the electrode is also assumed in the range of E_f - eV/2 and E_f + eV/2. Since the electrodes are fairly well conducting surfaces (almost metallic), the rate of electron transfer or transition between the nanoclusters and the electrodes is also assumed to be constant. By integrating the product of field emitted energy distribution and the DOS of silver nanoclusters over the range of E_f - eV/2 ~ E_f + eV/2, one can estimate the tunneling probability of field emitted electrons through the excited silver nanocluster states, and therefore, the EL intensity(equation 3-2-2). Although the relative probability of tunneling at different voltages is not quantitatively estimated due to the assumptions described above, the relative positions of tunneling peaks along V axis are unchanged and are mainly dominated by the excited electronic states of silver nanoclusters.

$$I(E) \approx aV \exp(\frac{-b}{V}) \exp(\frac{cE}{eV \cdot \sqrt{\phi}}) \cdot f_{elec}(E) \cdot DOS_{mol}(E) \qquad (3\text{-}2\text{-}1)$$

In the above equation, I(E) is current, V is voltage, E is energy of charges, $f_{elec}(E)$ is Fermi distribution function in the electrode as a function of electron energy, $DOS_{mol}(E)$ is density of states in the molecule as a function of electron energy, φ is work function of the electrode, a, b, and c are constant independent

of field or work function. a and b are independent to each other. Although a and c are somewhat related by using a common parameter (but in different order of magnitude), similar field emitted electron energy distribution to those in the literature[41] could be simulated by adjusting them independently. Directly related to the net current flow, the EL intensity (I_{EL}) is given by equation 3-2-2 by integrating the current (equation 3-2-1) in the effective transmission range. Note that Fermi distribution is moved toward higher energy (eV/2) due to the applied voltage (V) in equation 3-2-2.

$$I_{EL}(V) \approx aV \exp(\frac{-b}{V}) \int_{E_f - \frac{eV}{2}}^{E_f + \frac{eV}{2}} \exp(\frac{cE}{eV \cdot \sqrt{\phi}}) \cdot f_{elec}(E - \frac{eV}{2}) \cdot DOS_{mol}(E) dE \quad (3\text{-}2\text{-}2)$$

By using the calculated absorption spectra of Ag_2~Ag_7 [117-119] as the density of silver nanocluster excited states, the simulated I_{EL} vs V characteristics with Ag_5 is found to closely match the experimental EL intensity in the inset of figure 3-2-13.(figure 3-2-14 and figure 3-2-15) The parameters a,b, and c in equation 3-2-2 should be fit to produce reasonable peak widths of the field emitted electron energy distribution. The relative position of E_f with respect to the silver nanocluster HOMO energy levels cannot be determined solely from the theory due to the high degree of local geometry variation surrounding the individual nanoclusters. The simulation results, however, indicate that the peaks in EL intensity should match the peaks of the silver nanocluster absorption spectra with an arbitrary offset not far exceeding the normal range of HOMO-LUMO gap of the nanoclusters (=2~3eV). Because visualization and analysis of

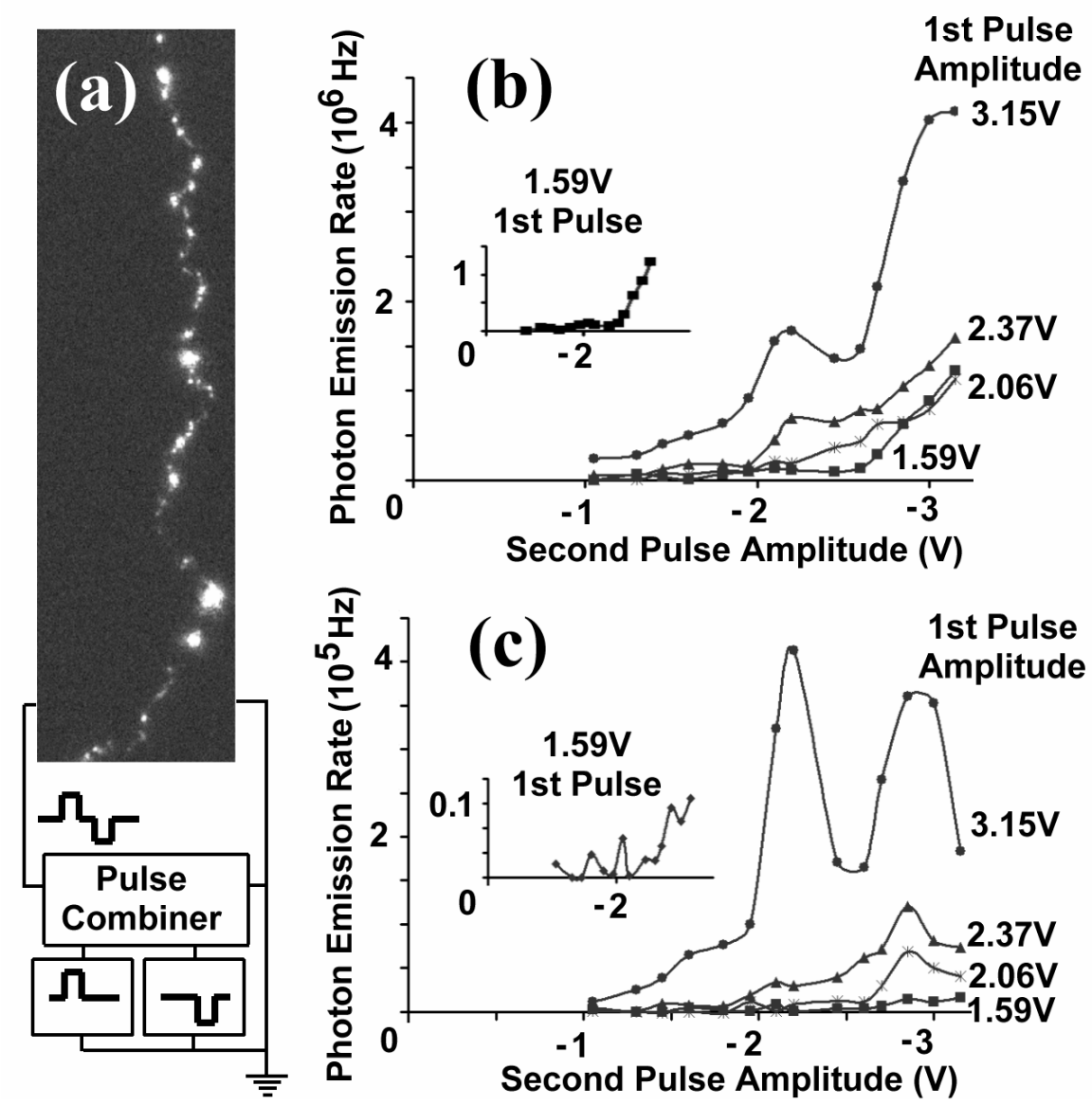

Figure 3-2-13. Quantum optoelectronic characteristics of typical Ag nanocluster junctions. (A) Typical Ag_n electroluminescent region with two consecutive pulse excitation (25MHz repetition rate) exhibiting blinking and dipole emission patterns characteristic of individual molecules. The EL shows a strong pulse polarity dependence and is detected only with a positive followed by a negative pulse with proper widths (2~4ns), amplitudes, and interpulse delay (<4ns). Other two-

pulse polarity combinations yield no detectable emission. The EL intensity also depends strongly on the amplitudes of the positive first and negative second pulses. (B) Integrated EL from ~30 molecules exhibits nearly monotonically increasing emission with both first and second pulse amplitudes. Positive pulses 4 ns ahead of the negative pulses, each with 2.6ns pulse widths and 1.0ns transition times, were used. On/off ratios of 15 were obtained with -2.1V signal pulses (the second pulse) following either 1.59V (Off) or 3.15V (On) gate pulses. The inset expands the lowest voltage case, showing the threshold behavior. (C) Integrated emission from 5 similar molecules exhibits three clear peaks along the second pulse amplitude at -1.6V, -2.1V and -2.85V. EL increases monotonically with first pulse (gate) amplitude, showing no discrete features except as a function of second pulse amplitude. The inset expands the lowest first pulse amplitude trace to show the high contrast obtained and therefore the discrete nature of the individual molecular/nanocluster energy levels.

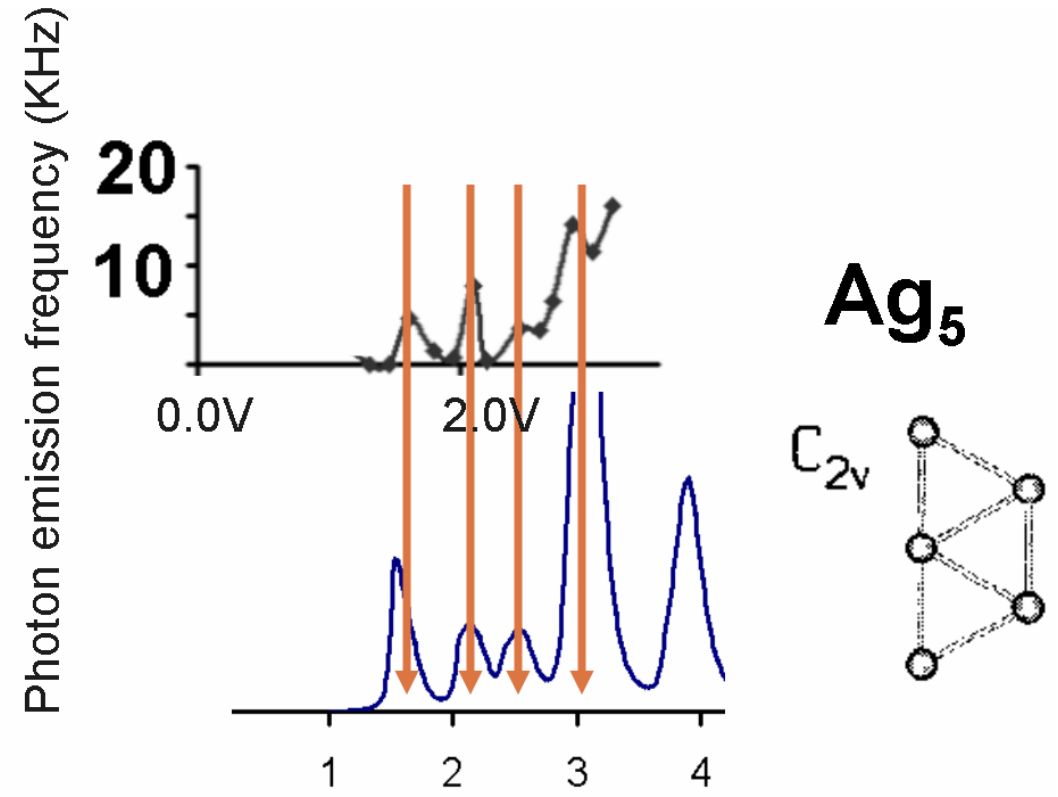

Figure 3-2-14. Simulation result (equation 3-2-2) matching the inset of figure 3-2-13 (C). This simulation result shows that the relative positions of EL intensity peaks of figure 3-2-13 (C) inset match the calculated absorption spectra of Ag_5 indicating that the electroluminescent nanocluster is Ag_5. Approximately, if parallel plate model is assumed to charge the electrodes, the absorption spectra with twice expanded energy axis will match the EL peaks with an arbitrary offset due to the local variation of the electrode geometry. In other words, one has to apply 2V to get the desired electron energy level (eV) in the anode by increasing the anode only V (=2V/2 for one electrode in parallel plate capacitor model) by applying voltage 2V.

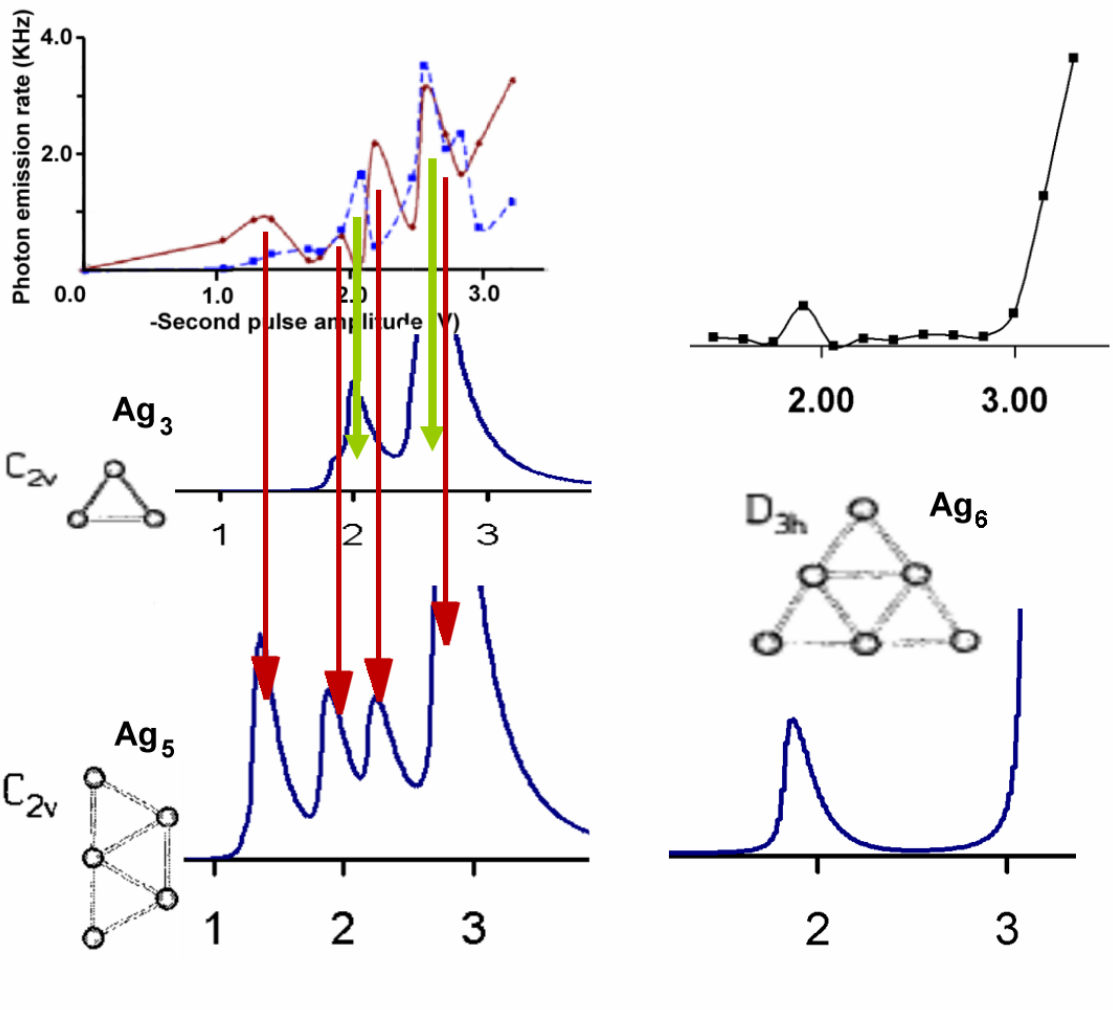

Figure 3-2-15. Simulation results of different EL species within electromigration induced nanogap junctions. The matching absorption spectra of silver nanoclusters indicate that the emissive species are Ag_3, Ag_5 and Ag_6.

sub-nm clusters on heterogeneous films is challenging at best, we must rely on connections with theory. Using the gas phase absorption of Ag_2-Ag_7, EL features corresponding to Ag_3, Ag_5 and Ag_6 are readily identified. Using the calculated absorption spectra[117,118], simulated EL peaks strongly suggest that Ag_3, Ag_5 and Ag_6 are found within the junctions.(figure 3-2-15)

3.3 Single molecule electroluminescence based optoelectronic logic gates

The complicated on/off behavior of silver nanocluster EL with the applied voltage can potentially be used to improve the efficiency of electronic circuits. Compared to current FET based electronic circuits that rely on the two state switching schemes, complex switching can yield much more compact electronics by providing a way to engineer the same function with much fewer switching elements.[26,53] As an example, Ag_3 and Ag_5 molecules can act as AND and XOR gate, respectively (figure3-3-1). Although the output is light instead of current, the output EL intensity is a direct probe of current passing through the junction nanoclusters. Furthermore, a full adder employing individual Ag_3 and Ag_5 molecules was implemented.[26] A full adder is a combination of different logic gates that performs an arithmetic addition operation of 3 input bits to generate 2 output bits (figure 3-3-1). In terms of the logic operation, the 2^1 and 2^0 bits – i.e., the carry and sum bits of a full adder correspond to the results of the logic operation of (P1 AND (P2 XOR P3)) OR (P2 AND P3) and ((P2 XOR P3) XOR P1), respectively with three bits of inputs (=P1, P2 and P3). While readily performed by only two nanoclusters within a single 2-terminal device, this

“simple” addition operation normally requires at least 25 normal two-state FETs. As the two full adder output bits, Ag_3 and Ag_5 EL were used, and three (0.00V or -1.05V) input pulses were used as three input bits. The three independent input pulses were combined with two pulse combiners to give one bias pulse which will be either 0.00V, -1.05V, -2.1V, or -3.15V. Combined with 1.6V first pulse added to the one bias pulse which was generated by the three input pulses, the 4 different final pulse trains yield different on/off behavior of the two silver nanoclusters as shown in figure 3-3-1. By matching the “on” and “off” state of the EL to “1” and “0”, the EL output of Ag_3 corresponds to the “carry” bit of a full adder while the EL output of Ag_5 corresponds to the “sum” bit of a full adder. With careful control of the emission strength by adjusting the pulse amplitudes for inputs, one can control the on/off ratio of the output to a degree. The demonstrated example of full adder shows reasonably good on/off ratio which ranged from 6.0 to 12.2. One can build true electronic circuits by conveying the EL outputs of the logic operations to the next silver nanoclusters utilizing the photoconductivity of the nanoclusters, experimental results of which will follow in the next 2 sections.

By utilizing the complex on/off behavior of the single molecular EL based on the field emitted electron tunneling through the discrete electronic states of the individual molecules, one can build highly efficient electronic circuits, for example, a full adder employing 2 silver nanoclusters instead of at least 25 normal FETs.

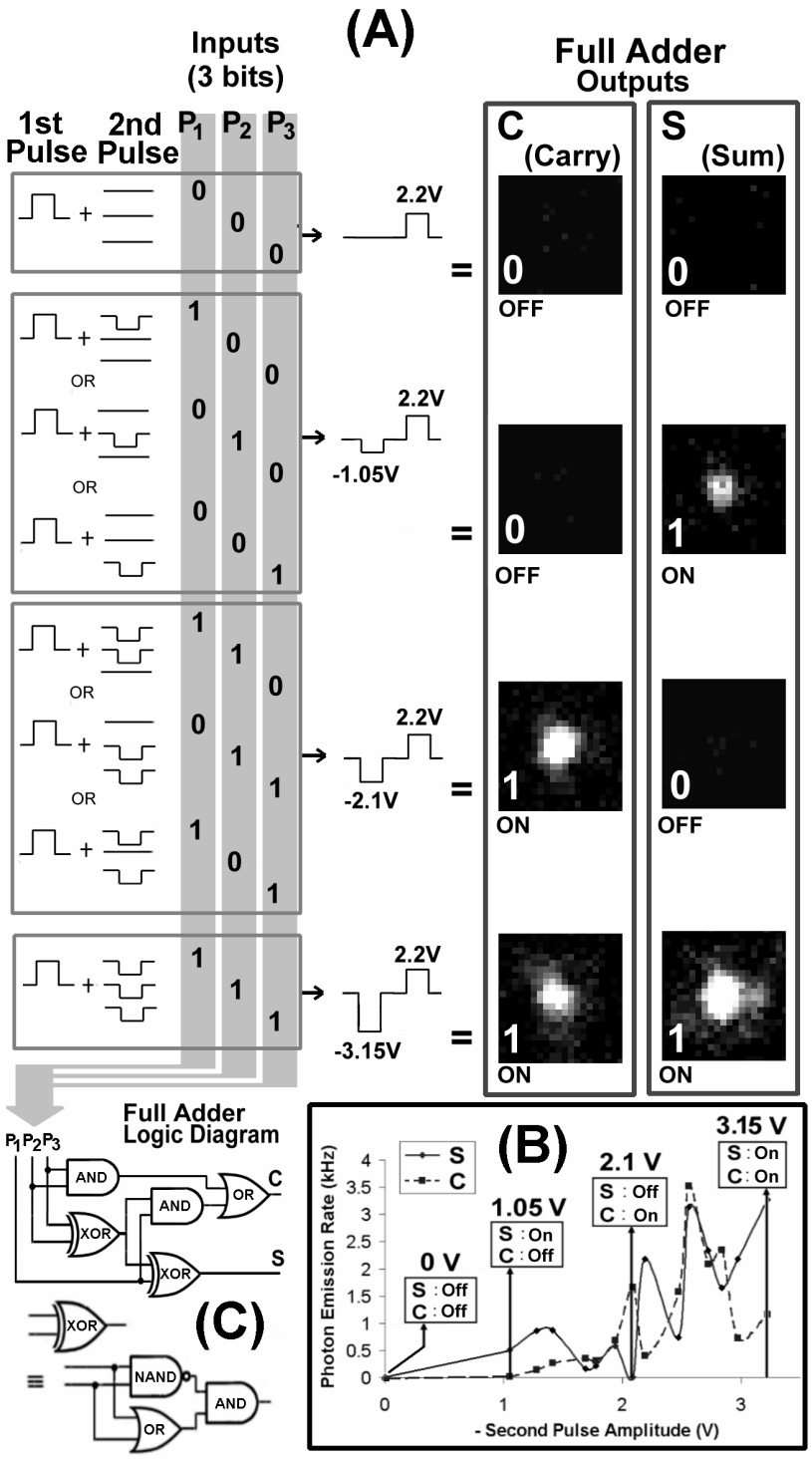

Figure 3-3-1. Quantum optoelectronic logic operations with coupled individual silver nanoclusters at room temperature. (A) Utilizing 2.6ns pulses at 25MHz repetition rates, a 2.2V first pulse was always added prior to the second

composite pulse, which, itself was constructed from three separate input pulses (P1, P2, P3), each with either 0.0V or –1.05V amplitude. Voltages described below refer to the composite second pulse amplitudes. (B) Nanocluster Ag_5 (“S” or sum) is turned on (“1”) at –1.05V and -3.15V, and turned off (“0”) at –2.1V. Nanocluster Ag_3 (“C” or carry) is turned on at –2.1V and –3.15V, and turned off at –1.05V. When only two input pulses with 0V (=“0”) or –1.05V (=“1”) amplitude are used, Ag_5 and Ag_3 act as XOR and AND gates, respectively to constitute a half adder. For example, if only P2 and P3 are used as inputs, Ag_3 EL output = ((P2 OR P3) AND NOT(P2 AND P3)) and Ag_5 EL output = (P2 AND P3). The on/off ratios for XOR and AND molecules are 6.0 and 12.2, respectively. The same molecules can also be fed with 3 inputs to work as a full adder. Input pulses and results for arithmetic addition of the corresponding three bits are shown in (A). (C) The discrete EL-producing energy levels of these two nanoclusters enable operation as a full adder. Nanoclusters Ag_5 and Ag_3 act as the output nodes in the logic diagram incorporating 9 basic binary logic gates typically requiring at least 25 standard field effect transistors. In the full adder implementation demonstrated in (A), nanocluster Ag_5 EL output = ((P2 XOR P3) XOR P1) and nanocluster Ag_3 EL output = (P1 AND (P2 XOR P3)) OR (P2 AND P3), in which XOR is defined as: a XOR b = ((a OR b) AND NOT (a AND b)).

3.4 The junction asymmetry (current and photocurrent)

DC electric response of the junction (diode behavior)

As revealed from fluorescence microscopy and EDS, the electromigration-induced silver oxide junctions are naturally heterojunctions. Therefore, in contrast to figure 3-2-2, the junctions should show electrical asymmetry – asymmetric current with the opposite field polarity. This lack of observed asymmetry is in DC excitation results from the very high field strength and the large current it induces. Such high powers are large enough to not distinguish the apparently small energy level differences in the heterojunctions that result from the different oxygen concentrations. Only when the sub-nanoampere currents were measured with relatively weak field strengths (<4V/10nm), the heterojunction nature was revealed (figure 3-4-1). Although created simply by applying a field to a continuous, single component film, the junction reproducibly shows strong polarity dependence and unidirectional current flow, yielding typical diode behavior with a 2.4V threshold forward bias and a forward to reverse bias conductance ratio of 71 (figure 3-4-1 (a)).[141] The threshold voltage and resistance strongly depend on initial film resistance, film thickness, and electromigration voltage. These parameters can be controlled to produce heterojunctions with nearly any desired impedance as illustrated by the range of behaviors demonstrated in the figures. This diode behavior arises from the different conduction band edge energies on each side of the heterojunction. As confirmed with the RF sputtered silver oxide films with different oxygen contents,

higher oxygen content generally leads to higher electrical resistance and smaller conductance increase with temperature. Thus, the cathode oxide must have a wider band gap or higher conduction band edge than the anode oxide (figure 3-4-1 (b)). With forward bias applied, electrons are pumped into the conduction band of the cathode oxide to establish an electric field across the junction. As electrons are pumped into the cathode oxide conduction band, they tunnel to the anode oxide conduction band (figure 3-4-1 (c)). Holes should also move accordingly. Yielding an exponential current with forward bias, nanoclusters are expected to act simply as tunneling bridges since no significant EL is detected with low voltage forward DC bias. On the other hand, with reverse bias applied, only capacitive current to charge the conduction band of the anode oxide is possible until it is charged to the level matching the conduction band edge of the cathode oxide. As a result, no significant current is allowed with reverse bias applied (figure 3-4-1). The asymmetric current is reasonably reproducible with multiple scannings if the highest field strength applied does not exceed ~4.0V/~10nm. This directly demonstrates diode behavior from the electrically written structures from an initially single component film. Thus, it is concluded that, through one simple step of DC current application, one can easily write diodes, or heterojunctions based on the oxidation level difference between the two sides of the nanogap junctions.

This electrical junction asymmetry shown in the figure 3-4-1 does not have much to do with the field emission/tunneling based AC EL process. Since the AC EL is from the tunneling through the junction nanoclusters while the DC electrical

current is from the tunneling between the two oxide layers, they do not necessarily show same polarity dependence. As a result, AC EL prefers negative pulse to more efficiently pump charges in to the excited states, not to the other side of the electrode, while the DC current prefers positive bias to more efficiently yield a tunneling current from the cathode to the anode. The important result of these experiments is that while EL is representative of the current flow through the silver nanoclusters, current measurements are dominated by other pathways that do not reflect almost anything about the charge transport through the single silver nanoclusters within the junction. This also proves the validity of the charge transport dynamics study through single molecules via electroluminescence, not solely electric current.

Photoconductivity and asymmetry of the photocurrent

As the junction nanoclusters show electroluminescence, it would be reasonable to expect such junctions to be photoconductive – the reverse process of electroluminescence. The junctions show reasonable photoconductivity when illuminated with light in the UV-Vis spectral range. Figure 3-4-2 shows the photoconductive nature of the junction with chopped light illumination. The photo conductivity response time of the junction is not measurable with a mechanical chopper up to 3.8kHz of chopping rate as shown in the figure 3-4-2. The photoconductivity normally ranges from 0.01~5nA/V with 0.1~1kW/cm^2 power from 514nm beam illumination over a 100μmX100μm area. Although largely independent of film preparation method, stronger photoconductivity is usually

observed with RF sputtered films. The photoconductivity shows no hysteresis with up to 3000 seconds of continuous illumination. Although it does not show hysteresis, illuminated films require some time to stabilize the photoconductivity due to the photoactivation of the silver oxide into silver nanoclusters to yield continuously better conductivity (see the next section). The photoconductivity is produced by illuminating only the junctions or slightly to the anode side, where the strong fluorescence is observed under photoexcitation. As evidenced from the fluorescence microscopy and spectroscopy with the comparison to the other results.[109-116] These emission centers at the junction and anode sides are silver nanoclusters or silver nanoclusters mixed with the silver oxide surface. Therefore, the junction photoconductivity is from the excited silver nanoclusters decaying through charge transfer to the electrodes.

Photoconductivity should also be asymmetric, following the observed electroluminescence and electric current asymmetries. To examine this photocurrent asymmetry, identical excitation is used under both forward and reverse bias (figure 3-4-3). With forward bias applied, excited electrons in the anode oxide region and within the junction will be excited and flow to the silver electrode. Thus, the amount of photocurrent with different photoexcitation wavelengths should be proportional both to the excitation profile of Ag nanoclusters and to the density of states (DOS) in the conduction band of the anode oxide to which the electrons are excited.[108,135] Since the silver nanocluster excitation profile shows the highest efficiency under blue excitation,[135] blue excitation is expected to yield the highest photocurrent efficiency with forward

bias. With reverse bias applied, however, the excited electrons must tunnel to the cathode across the cathode oxide with its higher conduction band edge than that of the anode oxide. Conversely, in the reverse bias case, the photocurrent is proportional to the energy of the incoming photons (i.e. to that of excited electrons). As seen in figure 3-4-3, the strong asymmetry in photoconductivity demonstrates that the higher conduction band of the cathode to which the excited electrons must tunnel is accessible only when the optically excited electron has high enough energy. As a result, the ratio of reverse to forward photoconductivity (i.e. the symmetry of the photoconductivity) depends on the energy of the photons exciting the anode oxide valence electrons (figure 3-4-3). Thus, this asymmetry in the photoconductivity can be utilized not only to detect photons, but also to measure the wavelength of photons at the nanoscale.

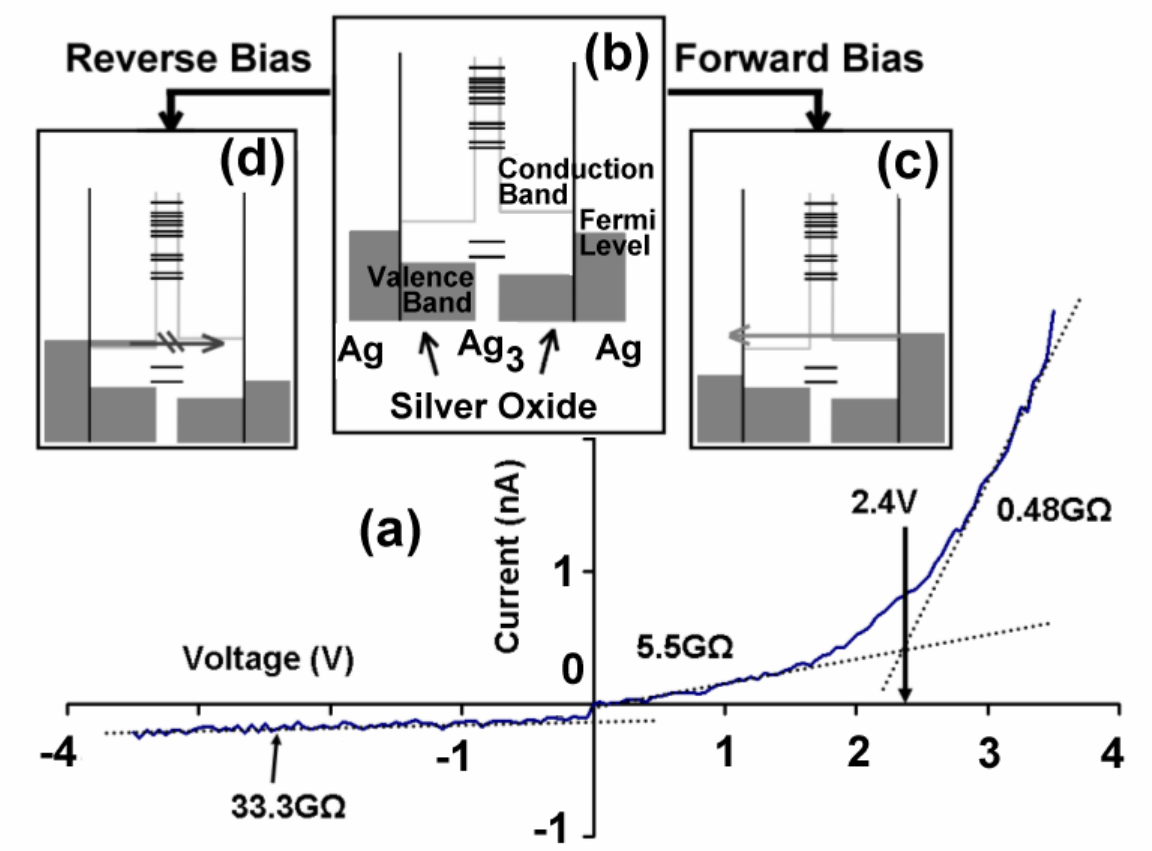

Figure 3-4-1. DC electric current through a nanoscale silver oxide heterojunction. The junction is formed on a chemically deposited silver oxide film with 4.5V DC electromigration voltage. (a), I-V characteristics of the heterojunction. Forward and reverse bias up to 3.5V is applied to examine the heterojunction polarity. Only forward bias yields noticeable current flow. The exponential I-V characteristic of the forward bias current suggests that it is due to the tunneling of charge carriers across the junction. Below threshold (2.4V forward bias), the forward bias conductance is 4.1 times higher than the reverse bias conductance. Above threshold, the value rises to 71. The ratio between the conductance above and below the threshold with forward bias is as high as 17. (b), Energy level

schematic of the junction without bias. Different oxygen contents of the anode and cathode silver oxides produce different band gaps on either side of this heterojunction with spanning Ag nanoclusters (e.g. Ag_3). (c), Energy level setup of the junction with forward bias. (d), Energy level setup of the junction with reverse bias. Only forward bias can allow significant current flow as indicated with the arrows. With reverse bias, tunneling is prevented due to the higher conduction band edge of the cathode oxide.

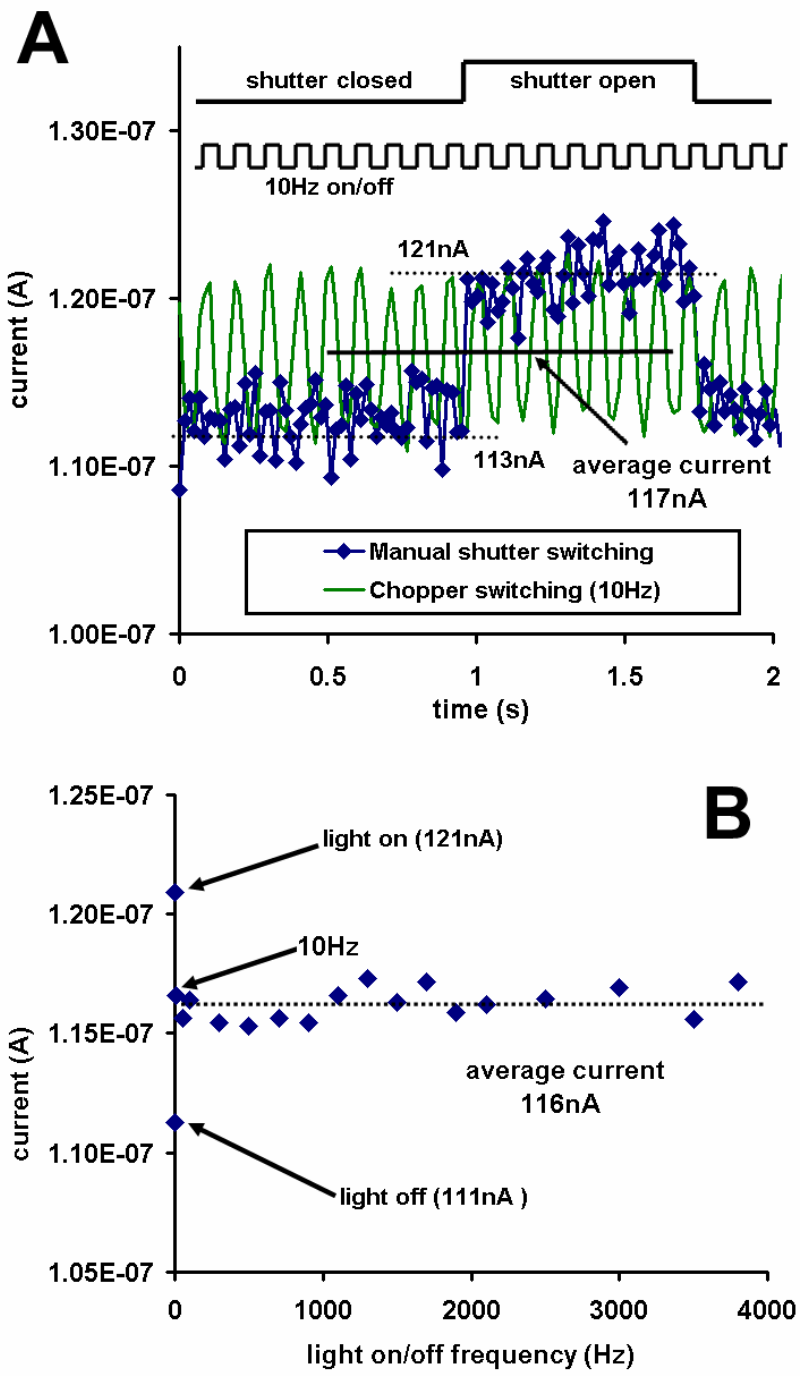

Figure 3-4-2. Photocurrent from a nanoscale silver oxide heterojunction with silver nanocluster tunneling bridges. An RF sputtered silver oxide film (200W RF power, deposition for 420 seconds in 1:2 Ar:O_2 environment) is applied with 15V electromigration voltage. Initial resistance and current are tunable with creation

conditions. Photocurrent of the junction was measured under chopped (10Hz) 514nm excitation (125W/cm^2) with 12V external field applied. (A), Photoconductivity response of the junction. The current reproducibly changes from 113nA to 121nA when the junction is optically excited by the chopped laser. The on and off photocurrent levels (the gray line in the chart) are in good agreement with those at much slower rates with a slow mechanical shutter (~1Hz) blocking the excitation source. No hysteresis from thermal effects is detected up to 3000 seconds of continuous excitation (the photoinduced current remains same) although the baseline current increases over time sometimes up to 40 times higher than the initial value (not shown) due to the photoactivation of silver oxide to better conducting silver nanoclusters. (B) Photoconductivity response time of the junction. A mechanical chopper was used to measure the response time of the junction photoconductivity. ~1000 measurements during 18 second illumination periods were made to give each point in the chart. Values of the current (baseline current, photocurrent and the average photocurrent) are in good agreement with the cases shown in A. Limited by the chopper frequency and macroscopic laser beam size (3mm diameter), the photo-induced current response was in all cases faster than we could measure.

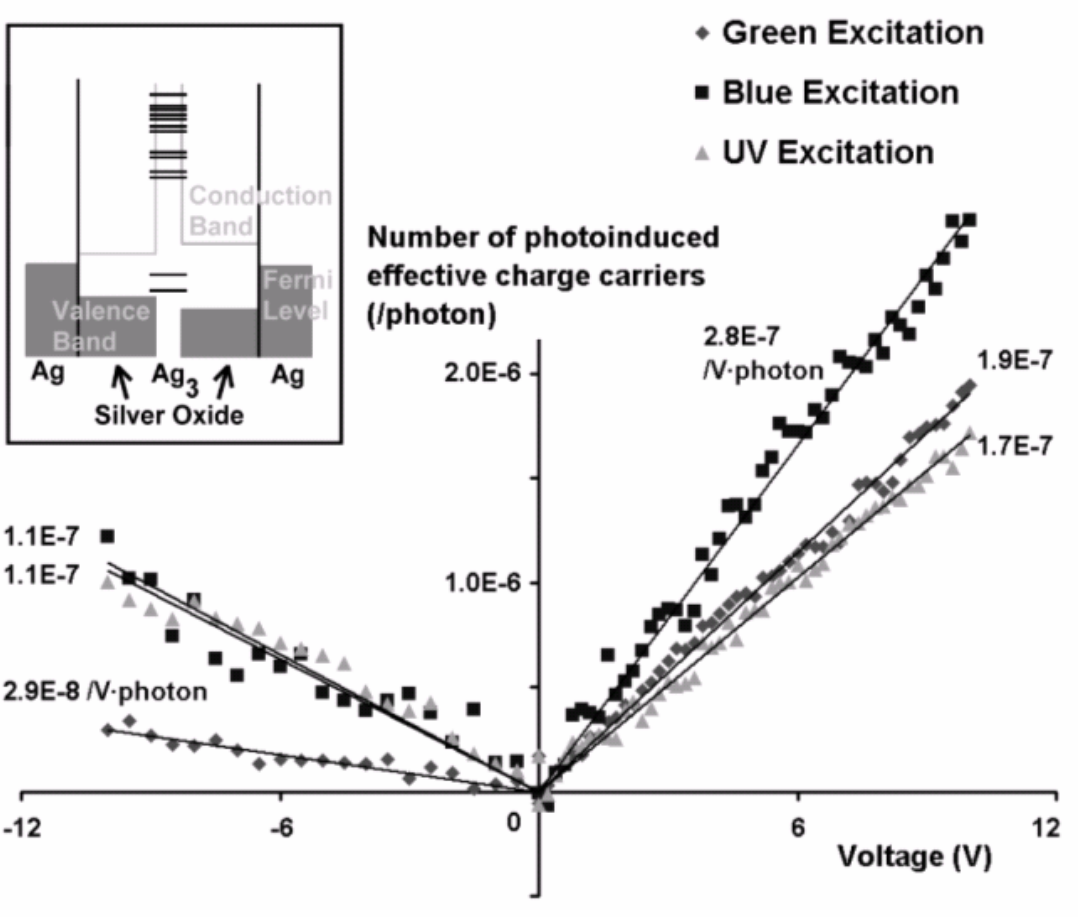

Figure 3-4-3. Photoconductivity asymmetry of the silver oxide junction with varying excitation energy. Initial experimental conditions are as in figure 3-4-2 except the excitation wavelengths and intensities. Using a 100-W Hg lamp in an epi-illumination geometry, 510~550nm, 450~480nm, and 360~390nm band passes were used for green, blue, and UV excitation, respectively. Reflecting the heterojunction behavior, the symmetry of photoconductivity (ratio of photoconductivities with reverse and forward bias) increases as photon energy increases – 0.15 for green, 0.41 for blue, and 0.63 for UV. The inset shows the schematic energy diagram of the junction showing asymmetric band edge levels.

The difference in silver oxide conduction band edges yields the photoconductivity asymmetry under forward and reverse bias. The higher cathode oxide conduction band edge provides a threshold that preferentially enables only higher energy photoelectrons to produce current in reverse bias. An Ag_3 nanocluster is used as an example of a tunneling bridge.

3.5 Applications of the electromigration induced silver oxide heterojunctions (conductive path writing, diodes, FETs and circuits-on-demand)

Electromigration induced heterojunction based diodes and FETs

The heterojunction nature of the electromigration induced silver oxide nanogap junctions holds promise in creating the electrically writable active electronics components such as diodes and FETs. The diode function of electromigration induced silver oxide nanogap junctions were tested as shown in figure 3-5-1. To utilize the heterojunction nature of these electrically written heterojunctions, AND and OR diode logic gates were implemented and tested. AND gates were created by electrically writing two heterojunctions in parallel with a common anode. Writing OR gates merely requires writing nanogap junctions with opposite polarity to that of the AND gates, thereby producing two diodes with a common cathode. In both cases, the voltage drop for varied inputs is measured with a properly matched resistor. As shown in figure 3-5-1, the junctions act as perfect diodes when proper circuit resistance is used. Because the junction has relatively high resistance, relatively high output resistance was used to make the forward junction resistance negligible. With 113MΩ output load, the junctions in the OR gate implementation act as perfect diodes. With slightly lower circuit resistance (23 MΩ), the junctions in the AND gate implementation also act as good diodes, such that the low state is clearly discriminated from the high state. Although the junction impedance with forward bias is still high compared with commercial diodes, this facile heterojunction fabrication method is the first one

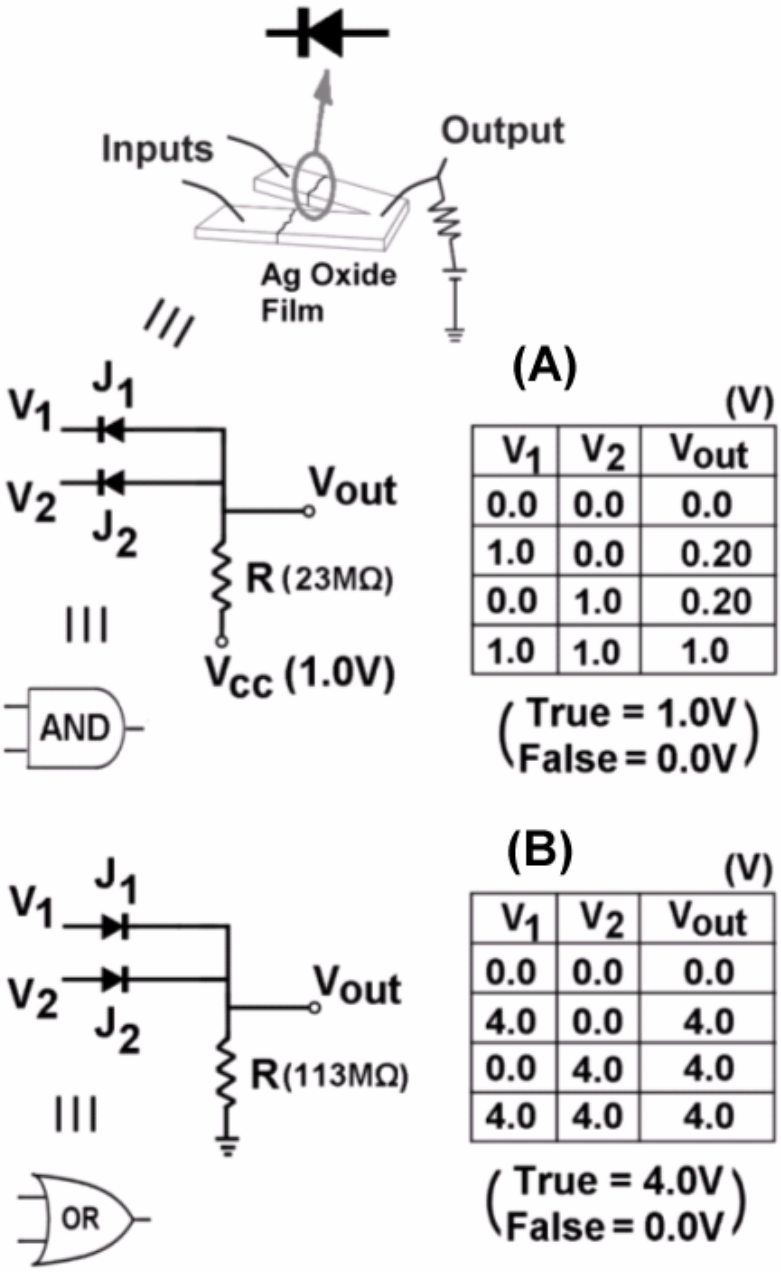

Figure 3-5-1. Diode logic gate implementation based on multiple junctions written within a single film. Two 100μm width strips were patterned on one silver oxide film to form two heterojunctions or diode junctions – one per strip. As indicated in the upper panel, the two strips were merged on one end. Each strip is separately

applied with a DC field to form nanoscale diodes through electromigration as described in the text. The direction of the formed diode is the same as that of the DC field used in electromigration. (A), Diode AND gate made of two electromigration induced heterojunctions. Junctions were formed at 1.8V electromigration voltage. 1.0V is used for “high” or “true”. Forward bias resistances were measured to be 2.1MΩ and 2.3MΩ for J_1 and J_2 respectively. Low states for “1 AND 0” or “0 AND 1” reproducibly appear to be 20% of high state, which are clearly distinguishable from the high state. (B), Diode OR gate made of similar junctions to those used in the AND gate implementation. 4.0V is used for “high” or “true”. Junctions were formed at 5.0V electromigration voltage. Forward bias resistances were measured to be 11kΩ and 8.6kΩ for J_1 and J_2 respectively. By using a high output load (113MΩ), the gate reproducibly performs perfect OR logic operations.

capable of directly and instantly writing electronic devices from a single component system.

To further verify the potential of electrically writing active electronic components through electromigration, FETs were created utilizing the electromigration induced silver oxide nanogap junctions. To fabricate the FETs based on these junctions, a silicon oxide layer was coated onto a junction as shown in figure 3-5-2. A gold electrode layer was added onto the top of the silicon oxide insulator layer to apply an electric field to the junction modifying the electrochemical potential of the silver oxide layers. This applied field should modulate the current through the junction. Figures 3-5-3 and 3-5-4 show the results of the transistor performance measurements. Although they do not yet show good performance as practical FETs (on/off ratio of 7 vs >100 for conventional FETs), it is proven that these junctions can act as FETs without additional molecules. As these junctions are commonly utilized in molecular electronics, these results provide important and missing controls on nanoscale charge transport. The limited voltage range yielding only a starting edge of the exponential current prevents the thermal destruction of the device due to passage of too high current. This stays below the threshold to enter into the exponential current regime. The demonstrated results are within the “safe” range of the voltage yielding reasonably reproducible I-V characteristics upon repeated scanning over the same voltage range. Therefore, it is possible to electrically write active electronic components such as diodes and FETs on a single component AgO thin films utilizing simple one-step electromigration process.

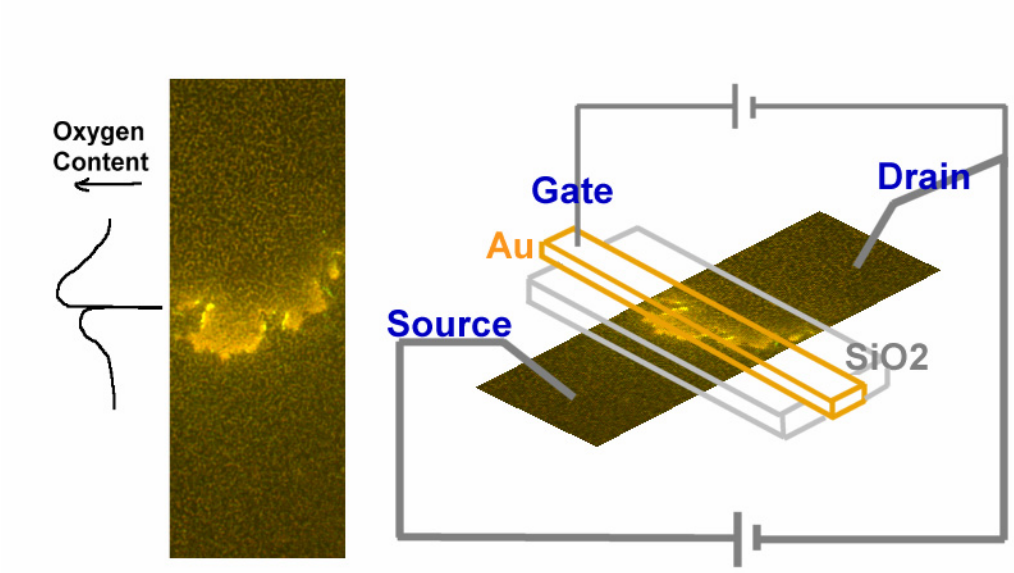

Figure 3-5-2. Schematics of the FET structure made from electromigration induced AgO nanogap junctions. Two different power suppliers were used to test FET performance. Chemically deposited silver oxide film of 80nm thickness was processed to a thin wire of 100micron width and SiO_2 layer was overcoated (~240nm thickness, RF sputtered for 3 hours at 1500W RF power in 6mTorr Ar environment). A thin gold layer (~40nm) was DC sputtered on top of the SiO_2 layer. The electromigration induced junction was formed at <3.0V after the overlayers were coated.

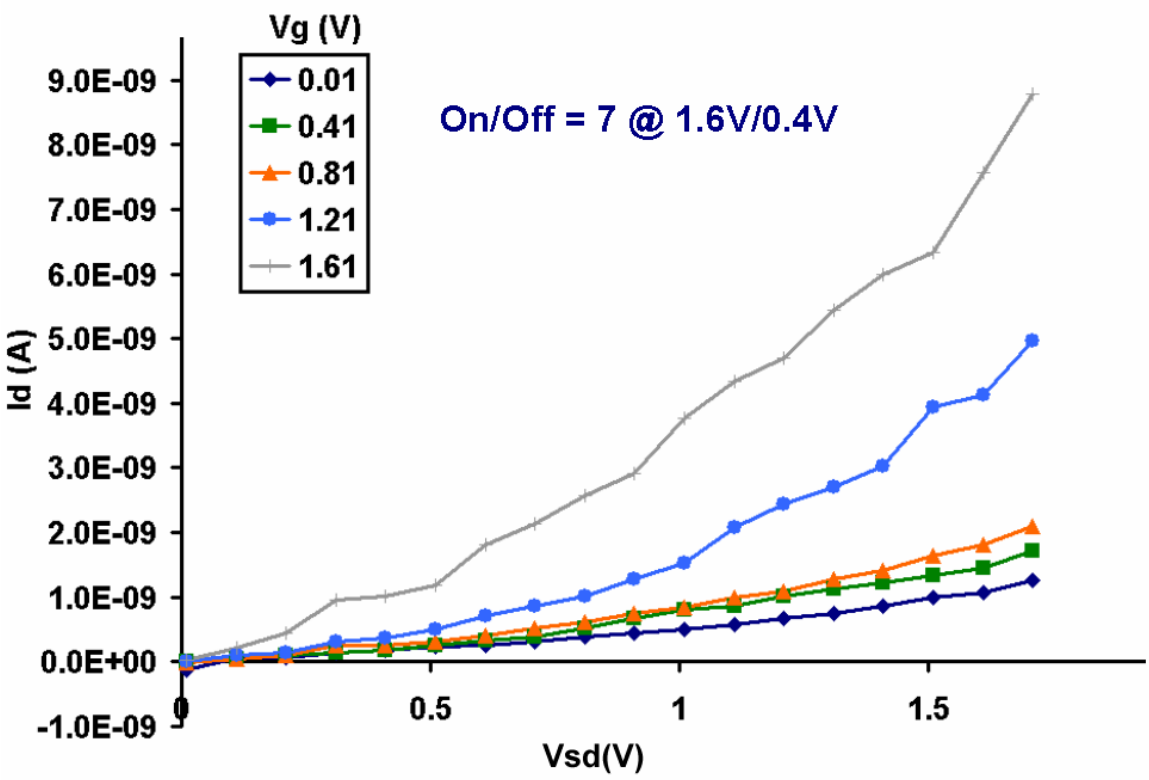

Figure 3-5-3. FET behavior of electromigration induced silver oxide nanogap junctions (figure 3-5-2). With a turn on gate voltage of 1.0V (see figure 3-5-4), the FET turns on. The on/off ratio below and above the turn on voltage is 7.0 (on at 1.6V/ off at 0.4V). Only slight exponential behavior of source-drain current is shown due to the device instability at higher voltage. Only under ~2V, the device shows reasonable reproducibility because the exponential increase in the current starts thermal destruction of the device.

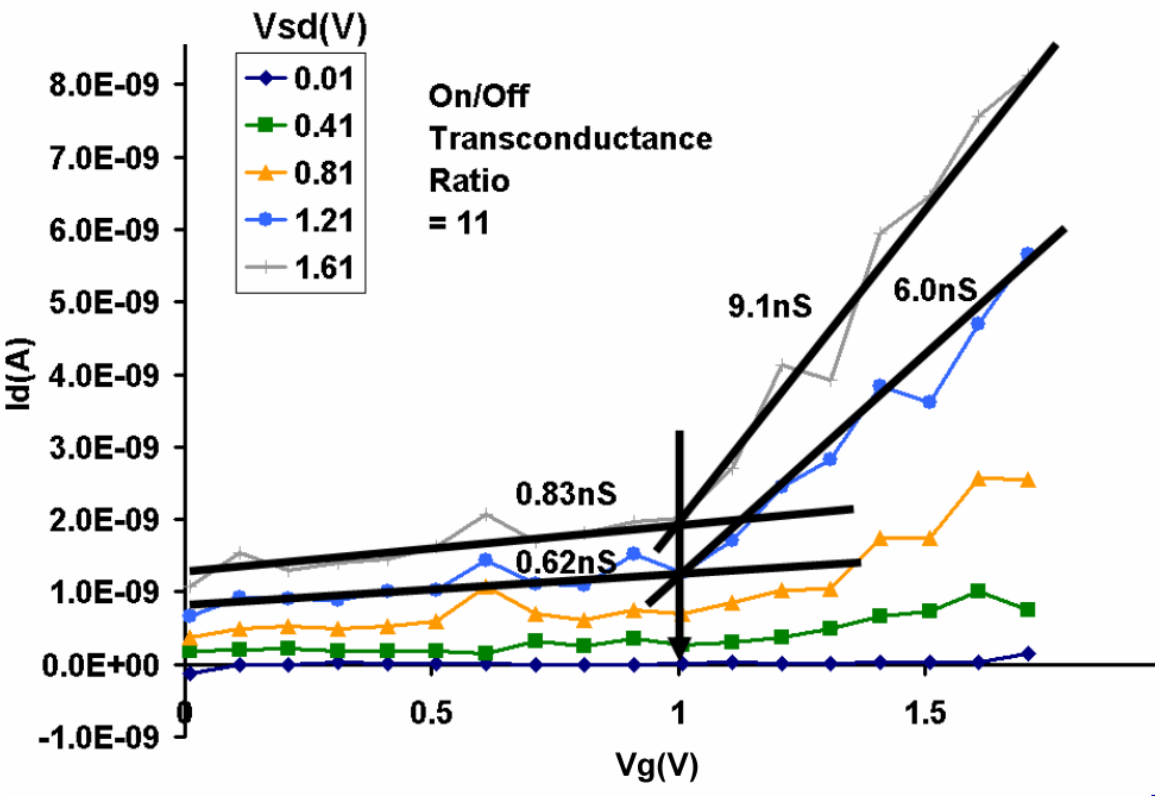

Figure 3-5-4. Transconductance of the same device shown in figure 3-5-3. Transconductance is defined to be I_{sd}/V_g. The turn-on threshold of gate voltage is 1.0V. Below and above the turn on gate voltage, the conductance ratio is as high as 11.

Electrical current path writing with light illumination

It is well known that silver oxide can be photoreduced through visible illumination. Previously, silver nanoclusters with similar photophysical properties to those within the junctions were formed on a thin silver oxide film by illuminating with blue or UV light. The photoactivation or optical writing of silver nanoclusters on silver oxide thin films not only changes the optical properties of the surface, but also, may change the surface electrical properties. To test this idea, the electromigration induced junction oxide area is illuminated with blue light (from a Hg arc lamp, definition in chapter 2) while the conductivity is measured. Figure 3-5-5 shows the results of this measurement. As the illumination turns on, the junction conductivity increases. But with the illumination off, the conductivity does not return to the original value. Part of the conductivity that goes away with the illumination off is due to the photoconductivity. The remaining conductivity increase is permanent and does not decrease again within several hours in vacuum. This optically written conductivity results from the silver nanoclusters written in high density on the surface and offers a promising path to optically write wires to connect electrically written active elements described in previous section. The photoconductivity portion gets weaker and weaker as the photoreduction gets saturated in the given illumination area as indicated in figure 3-5-5. Therefore, it is proven that one can optically write electrical current path through the junctions. The efficiency of the optical writing of the current paths is the highest with UV followed by blue illumination.

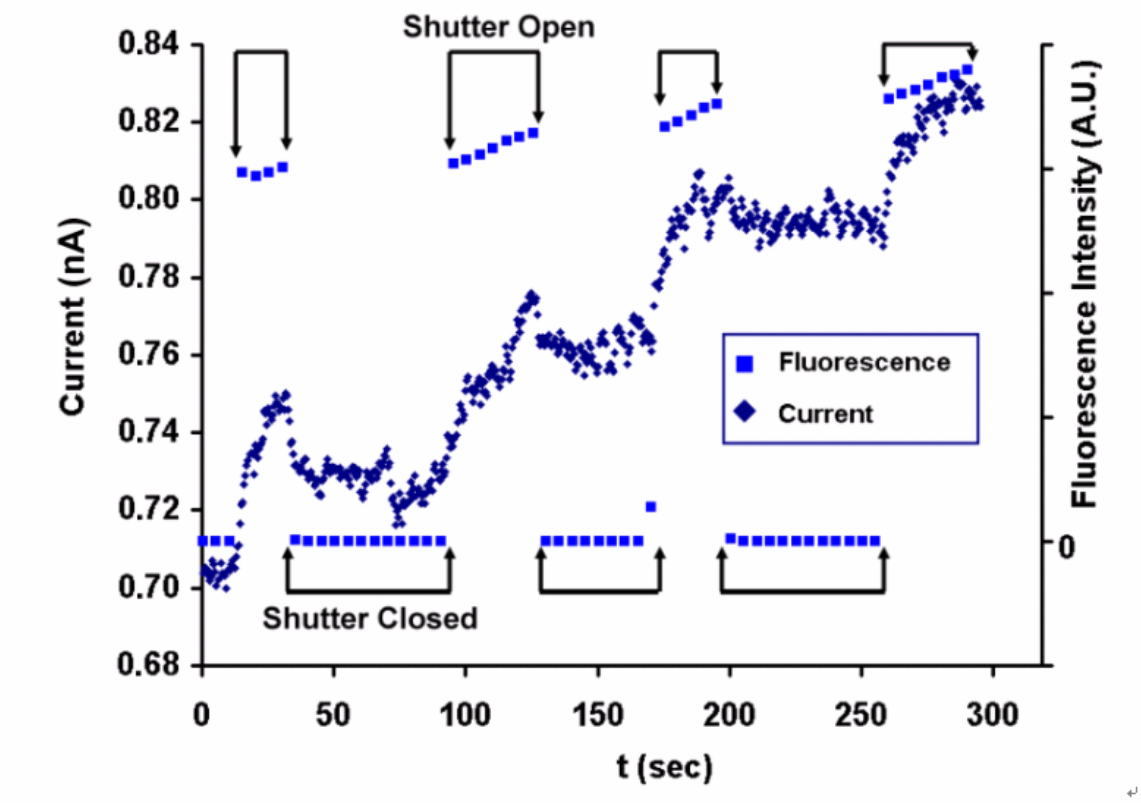

Figure 3-5-5. Photoactivation of the junction. Illuminating the junction oxide area by opening a shutter from the light source, both conductivity and fluorescence intensity increase due to the photoreduction of the oxide to silver nanoclusters. The elevated conductivity as well as the nanocluster concentration stays constant while the shutter is closed. The changed conductivity stays the same for days after the writing. Filtered mercury arc lamp (450~480nm) excitation was used to reduce the silver oxide region to silver nanoclusters. The increase in conductivity can take place both on the anode and the cathode oxide area and, thus, it is possible to erase the heterojunction by illuminating it with light.

3.6 Antibunching of silver nanoclusters fluorescence

Figure 3-6-1 illustrates two sample systems demonstrating antibunched single molecular emission schematized in figure 2-12-1. As described in section 1.9, figure 1-9-1 and equation 1-9-1/1-9-2, both antibunching signatures in figure 3-6-1 are manifested by the minimum $g^2(\tau)$ at $\tau = 0$.The dips at zero delay shown in the figure is not reaching absolute “zero” because the jitters of two APDs used in the experiments give ~1.1ns total error (Pythagorean sum of 1.0ns for one APD and 0.4ns for the other APD). With the lifetime not significantly longer that the jitter summation, the zero dip depth is severely limited by the jitter of the detectors. Simulation indicated that the zero dip depth with 1.1ns jitter would be ideally ~0.6. Therefore, having ~4ns lifetimes, the two sample systems – CN-PPV and CdSe quantum rods – show reasonably good antibunching signature proving they are quantum emitters. The non-zero baseline of CdSe quantum rods under pulsed excitation is due to the relatively fast repetition rate of the pulses compared to their lifetimes.

Due to the extremely fast lifetime of silver nanocluster excited states (two orders of magnitude faster than the jitter of the APD signal), only pulsed excitation could be used to see the antibunching signature. Unfortunately, most silver nanoclusters do not absorb strongly at the UV. Using the frequency doubled Ti:Sapphire laser to produce 430nm, ~200fs pulses at 84.1MHz repetition rate, the chromophores are poorly excited but with much background due to ubiquitous UV fluorescence from glass and impurities in solution. The laser was filtered with a 420 long pass filter to remove the shorter wavelength

components. This minimizes the UV excited background emission from optics and polymers in the sample. To enhance the fluorescence from silver nanoclusters, the pulsed excitation source center wavelength was shifted to ~425nm by cutting the shorter wavelength portion of the laser beam from the Ti:Sapphire crystal. One more issue with the antibunching of silver nanoclusters is to avoid the significant amount of Raman signal which is instantaneous process and shows shorter process time than the laser pulses (~200fs). To avoid such short time process that will severely degrade the antibunching contrast, a long pass emission filter was used. The emission filter used was 545nm long pass filter, which filtered out most of the Raman signal. Figure 3-6-2 shows the result of the highly filtered and therefore, highly attenuated antibunching experiment with dendrimer encapsulated silver nanoclusters. Despite the low coincidence counts due to the emission filter cutting not only Raman signal but also most of the fluorescence, the antibunching nature of the silver nanocluster emission is manifested by the significantly low incident count at zero delay between two successive photons.

Although it is promising that the silver nanocluster electroluminescence can be utilized as electrically driven single photon sources at room temperature, their extremely short lifetimes limit the demonstration of such application simply because the relevant electrical pulse generator with enough power is not commercially available.

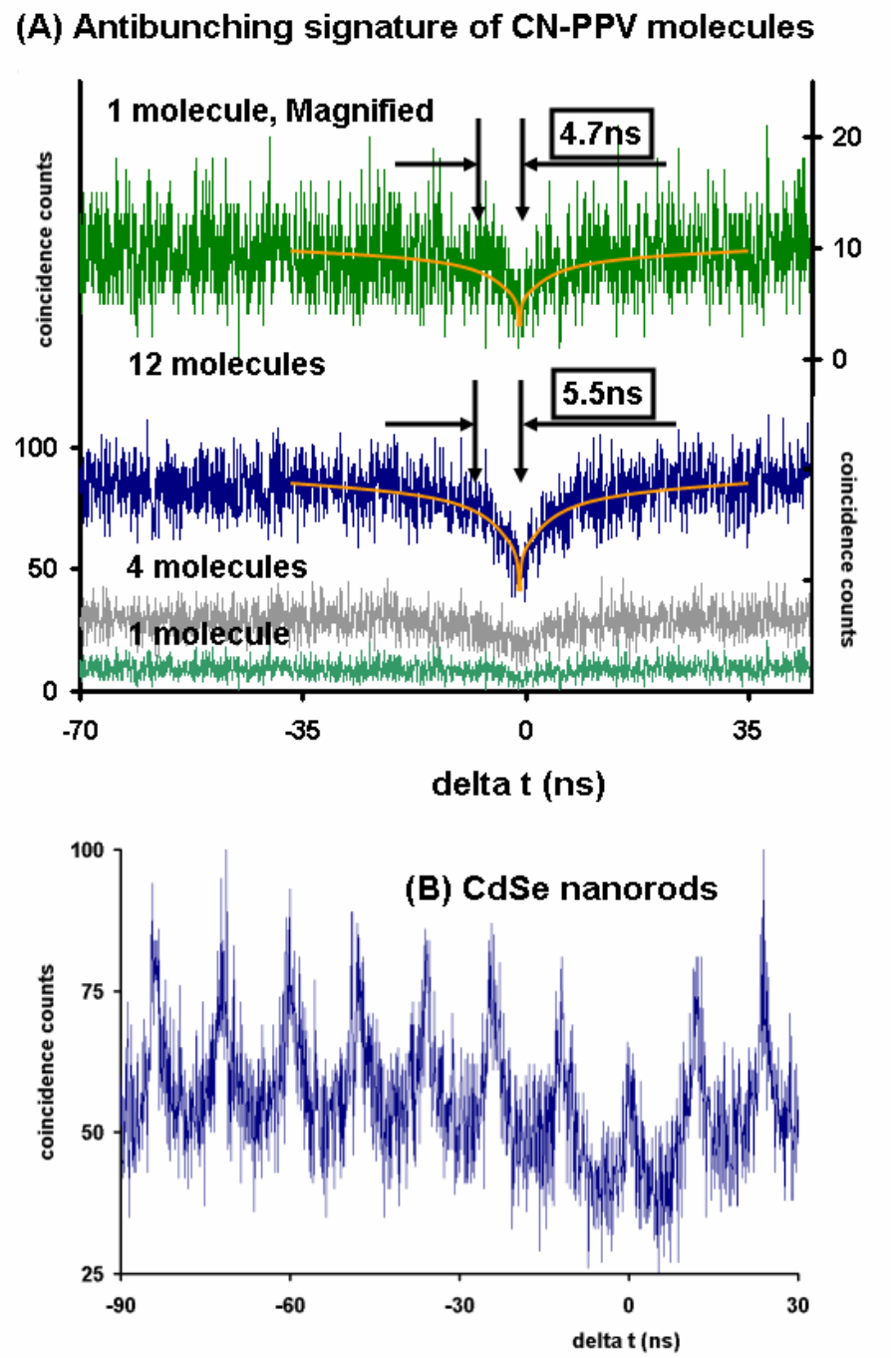

Figure 3-6-1. Antibunching signatures of sample systems. (A) Cyanonitrile substituted poly-paraphenylenevinylene (CN-PPV) under 514nm Ar Ion laser excitation with ~1kW/cm^2 power and (B) CdSe quantum rods under 400nm frequency doubled Ti:Sapphire laser with 84.1MHz repetition rate and

~1.4kW/cm^2 power. (A) Under continuous excitation source, the probability of finding two photons from one molecule at the exactly same time reaches zero yielding zero dip near zero $\Delta\tau$ as shown here. (See ideal case as shown in figure 1-9-1 and equation 1-9-1) Due to the APD pulse jitter (~1.1ns) as described in section 3-6, the dip depth does not reach zero (~0.6). However, with the consideration of the jitter, the results nicely match the simulated dip depth (~0.64). Despite the error introduced by the jitter, the lifetime measured with this experiment is in reasonably good agreement with the simple lifetime measurement experiments.[142,143] (B) Under pulsed excitation, the probability of finding two fluorescence photons within a single pulse should be zero if the pulse width is significantly shorter than the excited state lifetime. Due to the relative photochemical instability of CdSe quantum rods, a scanning stage was used to scan and collect the histogram data over hundreds of single nanorods (provided by Dr. Mostafa El-Sayed). Since very broad and strong UV excitation was used, the background fluorescence was unavoidable without shifting the excitation wavelength, which had to be done before proceeding to silver nanocluster antibunching experiments.

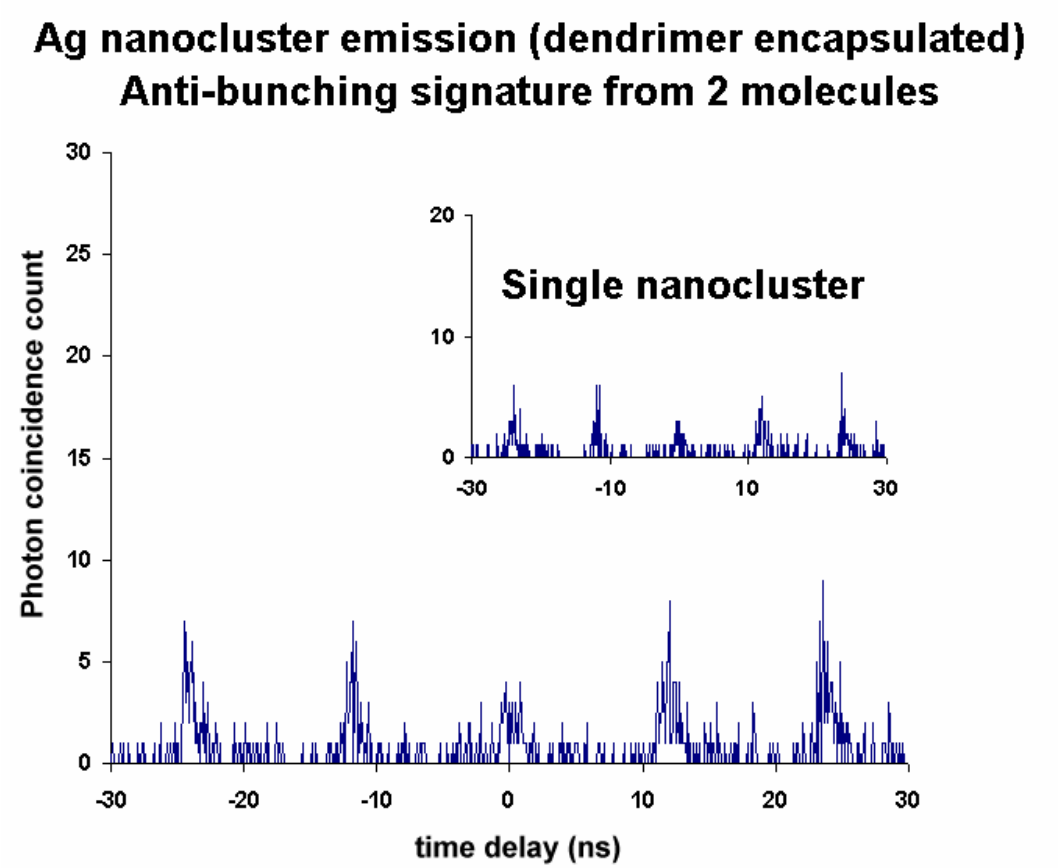

Figure 3-6-2. Antibunching signature of dendrimer encapsulated silver nanoclusters. Experimental setup is described in section 2-12. As evidenced by the smaller peak at time delay zero, the silver nanoclusters are proven to be single quantum emitters. 420nm pulsed excitation (84.1MHz repetition rate, <ps pulse width) was used. The excitation was cut with a 420nm long pass filter and the emission was also filtered with a 545nm long pass filter. The measured excitation intensity was 99W/cm^2. Due to the background emission from dendrimers, the photon incidence count at zero delay is not zero. The spacing between peaks shows the inverse of laser pulse repetition rate 84.1MHz.

CHAPTER IV

CONCLUSIONS

Charge transport dynamics study with more specific feedback – electroluminescence: single molecular charge transport through silver nanoclusters and its applications

Revealed by this research, electromigration induced silver oxide nanogap junctions enable single molecular charge transport dynamics to be studied through much more sensitive and specific feedback - electroluminescence. By simply fabricating the electromigration induced nanogap junctions out of silver or silver oxide thin films, one can *in-situ* form the silver nanoclusters within the junctions. These in-situ formed silver nanoclusters inside of the gap show strong and stable electroluminescence when an external electric field is applied. The similar photophysical properties of the emissive spots to those of dendrimer encapsulated and surface formed silver nanoclusters[110-116] confirm that the electroluminescent spots within the junction are molecular silver nanoclusters (Ag_2~Ag_8). By looking at the sensitive and site specific output (EL), the detailed charge transport dynamics through each site (or nanoclusters) could be studied. Extreme difficulty in measuring single electrons at room temperature can be avoided by using photons as probe for the charge transport. The results of EL

based charge transport study, therefore, are free of controversy and the photon output is representative of charge transport through junction nanoclusters. The results indicate that, even at room temperature, the charge tunneling through the excited states of individual silver nanoclusters yields clear NDR type I_{EL}-V behavior. The narrow energy distribution of the field emitted electrons combined with the resonant tunneling of electrons to the silver nanocluster excited states is the origin of the NDR behavior of the junction electroluminescence. Although the output cannot conveniently be utilized as directly conveyable electric charges to the next device, the electroluminescence output is representative of current flow and can be converted to the electric charges by utilizing the photoconductive nature of the junction clusters. The EL output itself also showed stable and reproducible complex switching behavior yielding a full adder based on two nanoclusters instead of >25 conventional FETs.

Although not directly proven, the application of the single molecular electroluminescence from spatially resolvable silver nanoclusters as room temperature single photon sources is also promising based on the photoexcitation photon antibunching signature of the same species in dendrimers.

Electromigration induced heterojunctions and their applications

Also revealed through current measurements of the junction, the current through the junction is not dominated by charge transport through the molecules within the junction. Instead, it is dominated by the heterojunction nature of the electromigration induced nanogap junctions and field emitted electrons.

Confirmed by the asymmetric current flow through the junction, the heterojunction nature of the electromigration induced nanogap junctions was first discovered by fluorescence microscopy and analyzed with EDS. Having different amounts of oxygen (higher in the cathode) on either side of the junctions, the nanogap junctions show asymmetric current and photoconductivity upon the application of electric fields opposite polarities. These nanogap diodes could perform diode to diode logic operations (DDL) such as AND and OR reproducibly. Oxygen content asymmetry based FETs were also fabricated and the performance was tested to show the junctions can perform the charge switching role of FETs. The asymmetric photoconductivity can potentially be utilized to fabricate nanoscale photon detectors and wavelength meters.

By combining the two techniques – electrical writing of active electronics components and optical writing of the conductive path, one can visualize optically and electrically writable electronic circuits on a silver oxide surface. The heterojunctions formed through electromigration would yield diodes and FETs on a properly prepared silver oxide thin film surface. Then the electric current path would be written optically by illumination light on the desired area of the silver oxide surface. Without involving any complicated processes such as photolithography, thus, one can potentially form electronic circuits as needed. This on-demand fabrication of electronic circuits would be useful in many space limited applications to conveniently convert downloadable software into hardware with desired functions.

REFERENCES

(1) Kittel, C. Introduction to Solid State Physics. In *Introduction to Solid State Physics*; 7 ed.; John Wiley & Sons, Inc.: New York, 1996.

(2) Williams, M. R. *A history of computing technology*, Rev. Ed. ed.; IEEE Computer Society Press: Los Alamitos, CA, 1997.

(3) Schoenmaker, W. *Quantum transport in submicron devices : a theoretical introduction*; Springer: Berlin, New York, 2002.

(4) Aviram, A.; Ratner, M. A. Molecular rectifiers *Chem. Phys. Lett.* **1974**, *29*, 277.

(5) Mujica, V.; Nitzan, A.; Datta, S.; Ratner, M. A.; Kubiak, C. P. Molecular Wire Junctions: Tuning the Conductance *J. Phys. Chem. B* **2003**, *107*, 91.

(6) Basch, H.; Ratner, M. A. Binding at molecule/gold transport interfaces. II. Orbitals and density of states *J. Chem. Phys.* **2003**, *119*, 11943.

(7) Basch, H.; Ratner, M. A. Binding at molecule/gold transport interfaces. I. Geometry and bonding *J. Chem. Phys.* **2003**, *119*, 11926.

(8) Mujica, V.; Roitberg, A. E.; Ratner, M. Molecular wire conductance: Electrostatic potential spatial profile *J. Chem. Phys.* **2000**, *112*, 6834.

(9) Tian, W.; Datta, S.; Hong, S.; Reifenberger, R.; Henderson, J. I.; Kubiak, C. P. Conductance spectra of molecular wires *J. Chem. Phys.* **1998**, *109*, 2874.

(10) Haug, H. *Quantum kinetics in transport and optics of semiconductors*; Springer: Berlin, New York, 1996.

(11) Mujica, V.; Kemp, M.; Roitberg, A.; Ratner, M. Current-voltage characteristics of molecular wires: Eigenvalue staircase, Coulomb blockade, and rectification *J. Chem. Phys.* **1996**, *104*, 7296.

(12) Barner, J. B.; Ruggiero, S. T. Observation of the incremental charging of silver particles by single electrons *Phys. Rev. Lett.* **1987**, *59*, 807.

(13) Jiang, C. S.; Nakayama, T.; Aono, M. Spatially resolved observation of Coulomb blockade and negative differential conductance on a Ag cluster on the clean GaAs(110) surface *Appl. Phys. Lett.* **1999**, *74*, 1716.

(14) Lambe, J.; McCarthy, S. L. Light emission from inelastic electron tunneling *Phys. Rev. Lett.* **1976**, *37*, 923.

(15) Jaklevic, R. C.; Lambe, J. Molecular vibration spectra by electron tunneling *Phys. Rev. Lett.* **1966**, *17*, 1139.

(16) Park, H.; Park, J.; Lim, A. K. L.; Anderson, E. H.; Alivisatos, A. P.; McEuen, P. L. Nanomechanical oscillations in a single-C60 transistor *Nature* **2000**, *407*, 58.

(17) Gaudioso, J.; Lauhon, L. J.; Ho, W. Vibrationally Mediated Negative Differential Resistance in a Single Molecule *Phys. Rev. Lett.* **2000**, *85*, 1918.

(18) Chen, J.; Wang, W.; Reed, M. A.; Rawlett, A. M.; Price, D. W.; Tour, J. M. Room-temperature negative differential resistance in nanoscale molecular junctions *Appl. Phys. Lett.* **2000**, *77*, 1224.

(19) Chen, J.; Reed, M. A.; Rawlett, A. M.; Tour, J. M. Large on-off ratios and negative differential resistance in a molecular electronic device *Science* **1999**, *286*, 1550.

(20) Xue, Y.; Datta, S.; Hong, S.; Reifenberger, R.; Henderson, J. I.; Kubiak, C. P. Negative differential resistance in the scanning-tunneling spectroscopy of organic molecules *Phys. Rev. B* **1999**, *59*, R7852.

(21) Nitzan, A.; Ratner, M. A. Electron Transport in Molecular Wire Junctions *Science (Washington, DC, United States)* **2003**, *300*, 1384.

(22) Park, H.; Lim, A. K. L.; Alivisatos, A. P.; Park, J.; McEuen, P. L. Fabrication of metallic electrodes with nanometer separation by electromigration *Appl. Phys. Lett.* **1999**, *75*, 301.

(23) Klein, D. L.; Roth, R.; Lim, A. K. L.; Alivisatos, A. P.; McEuen, P. L. A single-electron transistor made from a cadmium selenide nanocrystal *Nature* **1997**, *389*, 699.

(24) Klein, D. L.; McEuen, P. L.; Katari, J. E. B.; Roth, R.; Alivisatos, A. P. An approach to electrical studies of single nanocrystals *Appl. Phys. Lett.* **1996**, *68*, 2574.

(25) Reed, M. A.; Zhou, C.; Muller, C. J.; Brugin, T. P.; Tour, J. M. Conductance of a molecular junction *Science* **1997**, *278*, 252.

(26) Lee, T.-H.; Dickson, R. M. Two-terminal single nanocluster quantum optoelectronic logic gates *Proc. Natl. Acad. Sci. USA* **2003**, *100*, 3043.

(27) Service, R. F. Moecular Electronics: Next-generation technology hits an early midlife crisis. In *Science*, 2003; Vol. 302; pp 556.

(28) Sze, S. M. *Modern semiconductor device physics*; Wiley: New York, 1998.

(29) Nussbaum, A. *Semiconductor device physics*; Prentice-Hall: Englewood Cliffs, NJ, 1962.

(30) Neamen, D. A. *Semiconductor Physics & Devices*, 2nd ed. ed.; Irwin/McGraw-Hill: New York, 1997.

(31) *The International Technology Roadmap for Semiconductors*, 2001 Ed. ed.; International Sematech, 2001.

(32) Cox, P. A. *The electronic structure and chemistry of solids*; Oxford University Press: Oxford; New York; Tokyo, 1986.

(33) Heeger, A. J. Charge storage in conducting polymers: Solitons, polarons, and bipolarons *Polymer Journal (Tokyo, Japan)* **2002**, *34*, 148.

(34) Foster, C. M.; Heeger, A. J.; Kim, Y. H.; Stucky, G.; Herron, N. Photoexcited polarons in high-temperature superconducting oxides: structural

distortion and low frequency polarizability *Reviews of Solid State Science* **1990**, *4*, 601.

(35) Kim, Y. H.; Nowak, M.; Soos, Z. G.; Heeger, A. J. Strongly localized photogenerated bipolarons in polydiacetylenes *Synth. Met.* **1989**, *28*, D621.

(36) Ehrenfreund, E.; Moses, D.; Lee, K.; Heeger, A. J.; Cornil, J.; Bredas, J. L. Solitons in doped b-carotene films: optical absorption and ESR studies *Synth. Met.* **1993**, *57*, 4707.

(37) Esaki, L. New Phenomenon in Narrow Germanium p-n Junctions *Phys. Rev.* **1958**, *109*, 603.

(38) Liang, W.; Shores, M. P.; Bockrath, M.; Long, J. R.; Park, H. Kondo resonance in a single-molecule transistor *Nature* **2002**, *417*, 725.

(39) Park, J.; Pasupathy, A. N.; Goldsmith, J. I.; Chang, C.; Yaish, Y.; Petta, J. R.; Rinkoski, M.; Sethna, J. P.; Abruña, H. D.; McEuen, P. L.; Ralph, D. C. Coulomb blockade and the Kondo effect in single-atom transistors *Nature* **2002**, *417*, 722.

(40) Bao, Z.; Lovinger, A. J.; Dodabalapur, A. Organic field-effect transistors with high mobility based on copper phthalocyanine *Appl. Phys. Lett.* **1996**, *69*, 3066.

(41) Gadzuk, J. W.; Plummer, E. W. Field emission energy distribution (FEED) *Rev. Mod. Phys.* **1973**, *45*, 487.

(42) Bell, A. E.; Swanson, L. W. Total energy distributions of field-emitted electrons at high current density *Phys. Rev. B* **1979**, *19*, 3353.

(43) Binnig, G.; Rohrer, H. Scanning tunneling microscopy *IBM Journal of Research and Development* **1986**, *30*, 355.

(44) Binnig, G.; Rohrer, H. Scanning tunneling microscopy *Surface Science* **1985**, *152-153*, 17.

(45) Reed, M. A.; Zhou, C.; Muller, C. J.; Burgin, T. P.; Tour, J. M. Conductance of a molecular junction *Science (Washington, D. C.)* **1997**, *278*, 252.

(46) Zhou, C.; Deshpande, M. R.; Reed, M. A.; Jones, K., II; Tour, J. M. Nanoscale metal/self-assembled monolayer/metal heterostructures *Appl. Phys. Lett.* **1997**, *71*, 611.

(47) Datta, S.; Tian, W.; Hong, S.; Reifenberger, R.; Henderson, J. I.; Kubiak, C. P. Current-voltage characteristics of self-assembled monolayers by scanning tunneling microscopy *Phys. Rev. Lett.* **1997**, *79*, 2530.

(48) Jaklevic, R. C.; Lambe, J. Inelastic tunneling due to vibrational modes of yttrium and chromium oxides *Phys. Rev. B* **1970**, *[3]2*, 808.

(49) Lambe, J.; Jaklevic, R. C. Molecular vibration spectra by inelastic electron tunneling *Phys. Rev.* **1968**, *165*, 821.

(50) McCarthy, S. L.; Lambe, J. Enhancement of light emission from metal-insulator-metal tunnel junctions *Appl. Phys. Lett.* **1977**, *30*, 427.

(51) Nazin, G. V.; Qiu, X. H.; Ho, W. Atomic Engineering of Photon Emission with a Scanning Tunneling Microscope *Phys. Rev. Lett.* **2003**, *90*, 216110/1.

(52) Nilius, N.; Wallis, T. M.; Ho, W. Localized Molecular Constraint on Electron Delocalization in a Metallic Chain *Phys. Rev. Lett.* **2003**, *90*, 186102/1.

(53) Huber, J. L.; Chen, J.; McCormack, J. A.; Zhou, C.; Reed, M. A. An RTD/Transistor Switching Block and Its Possible Application in Binary and Ternary Adders *IEEE Trans. Electron. Devices* **1997**, *44*, 2149.

(54) Imry, Y.; Landauer, R. Conductance viewed as transmission *Rev. Mod. Phys.* **1999**, *71*, S306.

(55) Buttiker, M.; Imry, Y.; Landauer, R.; Pinhas, S. Generalized many-channel conductance formula with application to small rings *Phys. Rev. B* **1985**, *31*, 6207.

(56) Datta, S.; Assad, F.; Lundstrom, M. S. The silicon MOSFET from a transmission viewpoint *Superlattices Microstruct.* **1998**, *23*, 771.

(57) Xue, Y.; Datta, S.; Ratner, M. A. First-principles based matrix Green's function approach to molecular electronic devices: general formalism *Chem. Phys.* **2002**, *281*, 151.

(58) Calzolari, A.; Marzari, N.; Souza, I.; Nardelli, M. B. Ab-initio transport properties of nanostructures from maximally-localize Wannier functions *Los Alamos National Laboratory, Preprint Archive, Condensed Matter* **2003**, 1.

(59) Kobayashi, K. Surface-state conduction through p-bonded chains *Phys. Rev. B* **2003**, *68*, 075308/1.

(60) Kobayashi, K.; Ishikawa, E. Surface state conduction through dangling-bond states *Surface Science* **2003**, *540*, 431.

(61) Pleutin, S.; Grabert, H.; Ingold, G.-L.; Nitzan, A. The electrostatic potential profile along a biased molecular wire: a model quantum-mechanical calculation *J. Chem. Phys.* **2003**, *118*, 3756.

(62) Akis, R.; Bird, J. P.; Ferry, D. K. Eigenstate selection in open quantum dot systems: using the landauer formalism as a spectroscopic probe *Microelectron. Eng.* **2002**, *63*, 241.

(63) Paulsson, M.; Zahid, F.; Datta, S. Resistance of a molecule *Los Alamos National Laboratory, Preprint Archive, Condensed Matter* **2002**, 1.

(64) Damle, P.; Ghosh, A. W.; Datta, S. First-principles analysis of molecular conduction using quantum chemistry software *Chem. Phys.* **2002**, *281*, 171.

(65) Swanson, L. W.; Crouser, L. C. Total-energy distribution of field-emitted electrons and single-plane work functions for tungsten *Phys. Rev.* **1967**, *163*, 622.

(66) Young, R. D. Theoretical total-energy distribution of field-emitted electrons *Phys. Rev.* **1959**, *113*, 110.

(67) Yuasa, K.; Shimoi, A.; Ohba, I.; Oshima, C. Modified Fowler-Nordheim field emission formulae from a nonplanar emitter model *Surface Science* **2002**, *520*, 18.

(68) Karabutov, A. V.; Gordeev, S. K.; Ralchenko, V. G.; Korchagina, S. B.; Lavrischev, S. V.; Vlasov, I. I. BN-carbon and SiO2-carbon nanocomposites as low-field electron emitters *Diamond & Rel. Mater.* **2003**, *12*, 1698.

(69) Wang, S. G.; Zhang, Q.; Yoon, S. F.; Ahn, J.; Yang, D. J.; Wang, Q.; Zhou, Q.; Li, J. Q. Electron field emission from carbon nanotubes and undoped nano-diamond *Diamond & Rel. Mater.* **2003**, *12*, 8.

(70) Cui, J. B.; Ristein, J.; Ley, L. Low-threshold electron emission from diamond *Phys. Rev. B* **1999**, *60*, 16135.

(71) Young, R. D.; Muller, E. W. Experimental measurement of the total-energy distribution of field-emitted electrons *Phys. Rev.* **1959**, *113*, 115.

(72) Collazo, R.; Schlesser, R.; Sitar, Z. Role of adsorbates in field emission from nanotubes *Diamond & Rel. Mater.* **2002**, *11*, 769.

(73) Lewis, B. F.; Fischer, T. E. Energy distributions of field-emitted electrons from silicon. Evidence for surface states *Surface Science* **1974**, *40*, 371.

(74) Bagchi, A.; Gomer, R.; Penn, D. R. Field emission total energy distribution in the presence of adsorbates *Surface Science* **1974**, *40*, 555.

(75) Penn, D.; Gomer, R.; Cohen, M. H. Energy distribution in field emission from adsorbate-covered surfaces *Phys. Rev. Lett.* **1971**, *27*, 26.

(76) Russell, A. M.; Litov, E. Band gap in the energy distribution of electrons obtained from Si through field emission *Appl. Phys. Lett.* **1963**, *2*, 64.

(77) Schlesser, R.; McClure, M. T.; McCarson, B. L.; Sitar, Z. Mechanisms of field emission from diamond coated Mo emitters *Diamond & Rel. Mater.* **1998**, *7*, 636.

(78) McCarson, B. L.; Schlesser, R.; Sitar, Z. Field emission energy distribution analysis of cubic-BN-coated Mo emitters: Nonlinear behavior *J. Appl. Phys.* **1998**, *84*, 3382.

(79) Bagchi, A.; Young, P. L. Model calculation for field emission from adsorbate-covered W(100) *Phys. Rev. B* **1974**, *9*, 1194.

(80) Swanson, L. W.; Crouser, L. C. Effect of polyatomic adsorbates on the total energy distribution of field emitted electrons *Surface Science* **1970**, *23*, 1.

(81) Krasnov, A. N. Electroluminescent displays: history and lessons learned *Displays* **2003**, *24*, 73.

(82) Helfrich, W.; Lipsett, F. R. Fluorescence and defect fluorescence of anthracene at 4.2 DegK *J. Chem. Phys.* **1965**, *43*, 4368.

(83) Helfrich, W.; Schneider, W. G. Recombination radiation in anthracene crystals *Phys. Rev. Lett.* **1965**, *14*, 229.

(84) RodriguezViejo, J.; Jensen, K. F.; Mattoussi, H.; Michel, J.; Dabbousi, B. O.; Bawendi, M. G. Cathodoluminescence and photoluminescence of highly luminescent CdSe/ZnS quantum dot composites *Appl. Phys. Lett.* **1997**, *70*, 2132.

(85) Jahn, U.; Fujiwara, K.; Menniger, J.; Grahn, H. T. Cathodoluminescence studies of exciton localization in GaAs-AlGaAs single quantum wells *J. Appl. Phys.* **1995**, *77*, 396.

(86) Robins, L. H.; Farabaugh, E. N.; Feldman, A. Cathodoluminescence spectroscopy of free and bound excitons in chemical-vapor-deposited diamond *Phys. Rev. B* **1993**, *48*, 14167.

(87) Reynolds, C. L., Jr.; Lengle, S. E.; Swaminathan, V. Cathodoluminescence observation of excitons confined to a two-dimensional electron gas in a selectively doped heterostructure *Appl. Phys. Lett.* **1991**, *59*, 2700.

(88) Balk, L. J.; Kubalek, E. Micron scaled cathodoluminescence of semiconductors *Scanning Electron Microscopy* **1977**, *10*, 739.

(89) Liu, Z.; Pinto, J.; Soares, J.; Pereira, E. Efficient multilayer organic light emitting diode *Synth. Met.* **2001**, *122*, 177.

(90) Savvate'ev, V.; Friedl, J. H.; Zou, L.; Shinar, J.; Christensen, K.; Oldham, W.; Rothberg, L. J.; Chen-Esterlit, Z.; Kopelman, R. Nanosecond transients in the electroluminescence from multilayer blue organic light-emitting devices based on 4,4(')- bis(2,2(')diphenyl vinyl)-1,1(')-biphenyl *Appl. Phys. Lett.* **2000**, *76*, 1501.

(91) Bell, C. M.; Yang, H. C.; Mallouk, T. E. Materials Chemistry of Organic Monolayer and Multilayer Thin-Films *Advances In Chemistry Series* **1995**, *245*, 211.

(92) Suh, M. C.; Chin, B. D.; Kim, M.-H.; Kang, T. M.; Lee, S. T. Enhanced luminance of blue light-emitting polymers by blending with hole-transporting materials *Adv. Mater.* **2003**, *15*, 1254.

(93) Ohshita, J.; Kai, H.; Sumida, T.; Kunai, A.; Adachi, A.; Sakamaki, K.; Okita, K. Synthesis of novel bithiophene derivatives with an organosilanylene bridge, and their applications to electron-transporting materials in EL devices *Journal of Organometallic Chemistry* **2002**, *642*, 137.

(94) Lu, P.; Hong, H.; Cai, G.; Djurovich, P.; Weber, W. P.; Thompson, M. E. Synthesis of Octasubstituted Cyclooctatetraenes and Their Use as Electron Transporters in Organic Light Emitting Diodes *J. Am. Chem. Soc.* **2000**, *122*, 7480.

(95) O'Brien, D. F.; Burrows, P. E.; Forrest, S. R.; Koene, B. E.; Loy, D. E.; Thompson, M. E. Hole transporting materials with high glass transition temperatures for use in organic light-emitting devices *Adv. Mater.* **1998**, *10*, 1108.

(96) Uchida, M.; Izumizawa, T.; Nakano, T.; Yamaguchi, S.; Tamao, K.; Furukawa, K. Structural Optimization of 2,5-Diarylsiloles as Excellent Electron-Transporting Materials for Organic Electroluminescent Devices *Chem. Mat.* **2001**, *13*, 2680.

(97) Tasch, S.; Holzer, L.; Wenzl, F. P.; Gao, J.; Winkler, B.; Dai, L.; Mau, A. W. H.; Sotgiu, R.; Sampietro, M.; Scherf, U.; Mullen, K.; Heeger, A. J.; Leising, G. Light-emitting electrochemical cells with microsecond response times based on PPPs and novel PPVs *Synth. Met.* **1999**, *102*, 1046.

(98) Li, Y. F.; Gao, J.; Yu, G.; Cao, Y.; Heeger, A. J. ac impedance of polymer light-emitting electrochemical cells and light-emitting diodes: a comparative study *Chem. Phys. Lett.* **1998**, *287*, 83.

(99) Nepijko, S. A.; Ievlev, D. N.; Viduta, L. V.; Schulze, W.; Ertl, G. The light emission observed from small palladium particles during passage of electronic current *ChemPhysChem* **2002**, *3*, 680.

(100) Nepijko, S. A.; Ievlev, D. N.; Schulze, W. Influence of vacuum conditions on the light emission caused by passing a current through a silver cluster film *Physica B: Condensed Matter (Amsterdam, Netherlands)* **2001**, *304*, 45.

(101) Nepijko, S. A.; Fedorovich, R. D.; Viduta, L. V.; Ievlev, D. N.; Schulze, W. Light emission from small copper particles excited by current passage or by low-energy electron bombardment *Physica B* **2001**, *301*, 261.

(102) Nepijko, S. A.; Fedorovich, R. D.; Viduta, L. V.; Ievlev, D. N.; Schulze, W. Light emission from Ag cluster films excited by conduction current *Ann. Phys.-Berlin* **2000**, *9*, 125.

(103) Lloyd, J. R. Electromigration in integrated-circuit conductors *J. Phys. D: Appl. Phys.* **1999**, *32*, R109.

(104) Schimschak, M.; Krug, J. Electromigration-Induced Breakup of Two-Dimensional Voids *Phys. Rev. Lett.* **1998**, *80*, 1674.

(105) Lloyd, J. R. Electromigration in thin film conductors *Semiconductor Science and Technology* **1997**, *12*, 1177.

(106) Clarke, P. J.; Ray, A. K.; Hogarth, C. A. Electromigration-a tutorial introduction *International Journal of Electronics* **1990**, *69*, 333.

(107) Ho, P. S.; Kwok, T. Electromigration in metals *Rep. Prog. Phys.* **1989**, *52*, 301.

(108) Lee, T.-H.; Hladik, C. R.; Dickson, R. M. Asymmetric Photoconductivity within Nanoscale Break Junctions *Nano Lett.* **2003**, *3*, 1561.

(109) Peyser, L. A.; Vinson, A. E.; Bartko, A. P.; Dickson, R. M. Photoactivated fluorescence from individual silver nanoclusters *Science* **2001**, *291*, 103.

(110) Rabin, I.; Schulze, W.; Ertl, G.; Felix, C.; Sieber, C.; Harbich, W.; Buttet, J. Absorption and fluorescence spectra of Ar-matrix-isolated Ag-3 clusters *Chem. Phys. Lett.* **2000**, *320*, 59.

(111) Rabin, I.; Schulze, W.; Ertl, G. Absorption spectra of small silver clusters Ag-n (n >= 3) *Chem. Phys. Lett.* **1999**, *312*, 394.

(112) Felix, C.; Sieber, C.; Harbich, W.; Buttet, J.; Rabin, I.; Schulze, W.; Ertl, G. Fluorescence and excitation spectra of Ag-4 in an argon matrix *Chem. Phys. Lett.* **1999**, *313*, 105.

(113) Rabin, I.; Schulze, W.; Ertl, G. Light emission in matrix assisted cluster-cluster reactions *Cryst. Res. Technol.* **1998**, *33*, 1075.

(114) Rabin, I.; Schulze, W.; Ertl, G. Light emission during the agglomeration of silver clusters in noble gas matrices *J. Chem. Phys.* **1998**, *108*, 5137.

(115) Konig, L.; Rabin, I.; Schulze, W.; Ertl, G. Chemiluminescence in the agglomeration of metal clusters *Science* **1996**, *274*, 1353.

(116) Zheng, J.; Dickson, R. M. Individual water-soluble dendrimer-encapsulated silver nanodot fluorescence *J. Am. Chem. Soc.* **2002**, *124*, 13982.

(117) Bonacic´-Koutecky, V.; Veyret, V.; Mitric´, R. Ab initio study of the absorption spectra of Ag_n (n=5–8) clusters *J. Chem. Phys.* **2001**, *115*, 10450.

(118) Bonacic´-Koutecky, V.; Pittner, J.; Boiron, M.; Fantucci, P. An accurate relativistic effective core potential for excited states of Ag atom: An application for

studying the absorption spectra of Agn and Ag+ clusters *J. Chem. Phys.* **1999**, *110*, 3876.

(119) Bonacic´-Koutecky, V.; Cespiva, L.; Fantucci, P.; Koutecky, J. Effective core potential-configuration interaction study of electronic structure and geometry of small neutral and cationic Agn clusters : predictions and interpretation of measured properties *J. Chem. Phys.* **1993**, *98*, 7981.

(120) Yoon, J.; Kim, K. S.; Baeck, K. K. Ab initio study of the low-lying electronic states of Ag_3^-, Ag_3, and Ag_3^+: a coupled-cluster approach *J. Chem. Phys.* **2000**, *112*, 9335.

(121) Fedrigo, S.; Harbich, W.; Buttet, J. Optical-Response of Ag2, Ag3, Au2, and Au3 in Argon Matrices *J. Chem. Phys.* **1993**, *99*, 5712.

(122) Nilius, N.; Wallis, T. M.; Ho, W. Development of One-Dimensional Band Structure in Artificial Gold Chains *Science (Washington, DC, United States)* **2002**, *297*, 1853.

(123) Beveratos, A.; Brouri, R.; Gacoin, T.; Villing, A.; Poizat, J.-P.; Grangier, P. Single Photon Quantum Cryptography *Phys. Rev. Lett.* **2002**, *89*, 187901/1.

(124) Muller, A.; Zbinden, H.; Gisin, N. Quantum cryptography over 23 km in installed under-lake telecom fiber *Europhysics Letters* **1996**, *33*, 335.

(125) Paul, H. Photon antibunching *Rev. Mod. Phys.* **1982**, *54*, 1061.

(126) Yuan, Z.; Kardynal, B. E.; Stevenson, R. M.; Shields, A. J.; Lobo, C. J.; Cooper, K.; Beattie, N. S.; Ritchie, D. A.; Pepper, M. Electrically Driven Single-Photon Source *Science* **2002**, *295*, 102.

(127) Brunel, C.; Lounis, B.; Tamarat, P.; Orrit, M. Triggered source of single photons based on controlled single molecule fluorescence *Phys. Rev. Lett.* **1999**, *83*, 2722.

(128) Lounis, B.; Moerner, W. E. Single photons on demand from a single molecule at room temperature *Nature* **2000**, *407*, 491.

(129) Hollars, C. W.; Lane, S. M.; Huser, T. Controlled non-classical photon emission from single conjugated polymer molecules *Chem. Phys. Lett.* **2003**, *370*, 393.

(130) Kurtsiefer, C.; Mayer, S.; Zarda, P.; Weinfurter, H. Stable Solid-State Source of Single Photons *Phys. Rev. Lett.* **2000**, *85*, 290.

(131) Buchel, D.; Mihalcea, C.; Fukaya, T.; Atoda, N.; Tominaga, J.; Kikukawa, T.; Fuji, H. Sputtered silver oxide layers for surface-enhanced Raman spectroscopy *Appl. Phys. Lett.* **2001**, *79*, 620.

(132) Mihalcea, C.; Buechel, D.; Atoda, N.; Tominaga, J. Intrinsic Fluorescence and Quenching Effects in Photoactivated Reactively Sputtered Silver Oxide Layers *J. Am. Chem. Soc.* **2001**, *123*, 7172.

(133) Varkey, A. J.; Fort, A. F. Some Optical-Properties of Silver Peroxide (AgO) and Silver- Oxide (Ag2)) Films Produced By Chemical-Bath Deposition *Sol. Energy Mater. Sol. Cells* **1993**, *29*, 253.

(134) Lee, T.-H.; Gonzalez, J. I.; Dickson, R. M. Strongly enhanced field-dependent single-molecule electroluminescence *Proc. Natl. Acad. Sci. USA* **2002**, *99*, 10272.

(135) Peyser, L. A.; Lee, T.-H.; Dickson, R. M. Mechanism of Agn nanocluster photoproduction from silver oxide films *J. Phys. Chem. B* **2002**, *106*, 7725.

(136) Lee, T.-H.; Dickson, R. M. Single-Molecule LEDs from Nanoscale Electroluminescent Junctions *J. Phys. Chem. B* **2003**, *107*, 7387.

(137) Kramer, N.; van den Berg, M. R.; Schoenenberger, C. Scanning tunnelling microscope-induced oxidation of hydrogen passivated silicon surfaces *Thin Sol. Films* **1996**, *281-282*, 637.

(138) Barniol, N.; Perez-Murano, F.; Abadal, G.; Ye, J. H.; Aymerich, X. Field induced nanomodification on silicon (100) with scanning tunneling microscopy *Microelectron. Eng.* **1995**, *27*, 27.

(139) Tjeng, L. H.; Meinders, M. B. J.; Elp, J. v.; Ghijsen, J.; Sawatzky, G. A.; Johnson, R. L. Electronic Structure of Ag2O *Phys. Rev. B* **1990**, *41*, 3190.

(140) Alameddin, G.; Hunter, J.; Cameron, D.; Kappes, M. M. Electronic and geometric structure in silver clusters *Chem. Phys. Lett.* **1992**, *192*, 122.

(141) Lee, T.-H.; Hladik, C. R.; Dickson, R. M. Facile, on-demand electronic nanodevice fabrication from photo- and electro-active silver oxide *Appl. Phys. Lett.* **2004**, *84*, 118.

(142) Kumar, P.; Mehta, A.; Dadmun, M. D.; Zheng, J.; Peyser, L.; Bartko, A. P.; Dickson, R. M.; Thundat, T.; Sumpter, B. G.; Noid, D. W.; Barnes, M. D. Narrow-

bandwidth spontaneous luminescence from oriented semiconducting polymer nanostructures *J. Phys. Chem. B* **2003**, *107*, 6252.

(143) Mehta, A.; Kumar, P.; Dadmun, M. D.; Zheng, J.; Dickson, R. M.; Thundat, T.; Sumpter, B. G.; Barnes, M. D. Oriented Nanostructures from Single Molecules of a Semiconducting Polymer: Polarization Evidence for Highly Aligned Intramolecular Geometries *Nano Lett.* **2003**, *3*, 603.

VITA

Tae-Hee Lee was born in 1971 in Seoul, South Korea. He graduated from Sogang University in 1993 with honors. He got a master's degree in science in 1995 from Sogang University. During his undergraduate and graduate tenure, he was exposed to electrochemistry of solid state materials. As a researcher in industry, Tae-Hee Lee studied polymer dynamics as well as R&D project evaluation methodology. Since the year 2000, Tae-Hee Lee has been conducting his Ph.D. thesis research in single molecule spectroscopy/microscopy and optoelectronics of silver nanoclusters.